THESE DE DOCTORAT EN COTUTELLE INTERNATIONALE

L'UNIVERSITE DE RENNES 1

ECOLE DOCTORALE N° 601 :
MAthématiques, Télécommunications, Informatique, Signal, Systèmes, Électronique (MATISSE)
Spécialité : Composants et dispositifs pour l'électronique et la photonique

MCMASTER UNIVERSITY

DEPARTMENT OF ENGINEERING PHYSICS

Control of the mechanical and optical properties of SiN_x-based films for optical and strain engineering applications

Par

Brahim AHAMMOU

Thèse présentée et soutenue à Hamilton, Ontario, Canada, le 24 Janvier 2023
Unité de recherche : Institut FOTON (UMR 6082)

Rapporteurs avant soutenance :

Christophe Labbé Maître de conférences HDR à l'Université de Caen (France)
Karim Sallaudin Karim Professeur à Waterloo University (Canada)

Composition du Jury :
Attention, en cas d'absence d'un des membres du Jury le jour de la soutenance, la composition du jury doit être revue pour s'assurer qu'elle est conforme et devra être répercutée sur la couverture de thèse

Président :	Hatem Zurob	Professeur à McMaster University (Canada)
Examinateurs :	Stéphanie Escoubas	Professeure à l'Université d'Aix-Marseille (France)
	Ray LaPierre	Professeur à McMaster University (Canada)
Dir. de thèse :	Jean-Pierre Landesman	Professeur à l'Université Rennes 1 (France)
	Peter Mascher	Professeur à McMaster University (Canada)
Co-encadrant :	Christophe Levallois	Maître de conférences à l'INSA de Rennes (France)

"In life, everything is possible. You might have less talent, you might have fewer qualities, you might have less money, but if you want, if you work, if you fight, if you believe, well, you can do it. However, be careful. It is not a miracle. It is hard work!"
— Walid Regragui.

"Growth is in a series of mistakes. That's the only way you learn."
— Steve Harvey.

"Slowly is the fastest way to get to where you want to be; the top of one mountain is the bottom of the next, so keep climbing."
— André De Shields.

Control of the mechanical and optical properties of SiN_x-based films for optical and strain engineering applications

A Thesis Submitted to the School of Graduate Studies in the Partial Fulfillment of the Requirements for the Degree: Doctor of Philosophy

By Brahim Ahammou*, M. Eng.

December 2022

* e-mails : ahammoub@mcmaster.ca & brahim.ahammou@univ-rennes1.fr

Acknowledgements

I am deeply grateful to everyone who have supported me and contributed to the completion of my Ph.D. project. My sincere thanks go to my supervisors, Jean-Pierre Landesman, Peter Mascher, and Christophe Levallois, for their guidance, encouragement, and invaluable insights throughout my research journey. I am also thankful to my thesis committee: Christophe Labbé, Karim Sallaudin Karim, Stéphanie Escoubas and Ray LaPierre for their time and efforts in evaluating my research work and participating in my Ph.D. defense. Special thanks to Hatem Zurob for chairing my thesis defense.

I am grateful for the opportunity to be part of various laboratories and to experience different cultures in France and Canada. I would like to express my appreciation to all the members of these labs for their support and collaboration. I would like to extend my sincere thanks to Aysegul Abdelal, Paramita Bhattacharyya, Emmanuel Schaub and Fahmida Azmi for their valuable contributions to my research.

My research journey would not have been the same without the support and friendship of my fellow researchers and friends, Alain Moreac, Anouar Rkhami, Anwar Kerchaoui, Daniel Hilal, Fahmida Azmi, Julie Le Pouliquen, Maryam Sadeghiyan, Paramita Bhattacharyya, Rachid Khneisser, Soraya Ababou-Girard, and others.

As I will not be able to name everyone, I would like to thank everyone with whom I shared a meal or even a coffee for their enjoyable company and for helping to make my time in the lab and abroad more memorable.

Last but not least, I must express my gratitude
To my family, who always bore my inconstant attitude,
They stood by me through all difficult moments,
Helping me weather the storm, no matter my torments.

You know, my PhD journey was emotionally draining,
Financially depleting, and physically exhausting,
But you were there for me, every step of the way,
Encouraging me to never lose my pep and stray.

Your encouragement and support carried me through,
No matter how far I was from you…

You taught me good values, how to work hard and be patient,
How to have self-awareness and self-knowledge, no matter the situation.

Remember that without your love and constant care,
This PhD achievement would not have been there.
I dedicate all my hard work and achievements,
To my beloved parents, whom I will forever cherish!

So please, for all those chasing their dreams,
Do not forget to care for those who gave you your wings.
Despite my new fancy title, I will stay modest and true,
Thanks to my loved ones, who always knew!

Brahim Ahammou

Abstract

Due to their attractive properties, silicon nitride (SiN_x) based films have been recognized as essential dielectric films in the microelectronic and optoelectronic industries. In this PhD thesis, we describe how we can control the refractive index and the mechanical properties of SiN_x and silicon oxynitride (SiO_yN_x) films by tuning the deposition process parameters. We use two different plasma-enhanced chemical vapor deposition reactors: a standard capacitively coupled reactor with radiofrequency excitation and an electron cyclotron resonance reactor with microwave excitation. We discuss the fabrication and characterization of multilayer structures as an optical application of our thin films. We focus on characterizing and understanding these thin films' optical properties through spectroscopic ellipsometry. We also study their mechanical properties experimentally using the wafer curvature measurement technique, microstructure fabrication, and nanoindentation measurements.

Finally, we show accurate measurements of the strain distribution induced within GaAs wafers when such thin films are structured in the shape of elongated stripes of variable width, using standard optical lithography and plasma etching. For this, we map the anisotropic deformation, measuring the degree of polarization of the spectrally integrated photoluminescence (PL) generated within GaAs by excitation with a red laser. PL from bulk cubic semiconductors such as GaAs is unpolarized, whereas anisotropic strain produces some degree of polarization. These maps were measured either from the semiconductor surface or from cleaved cross-sections. They provide a detailed and complete image of the crystal deformation in the vicinity of the structured stressor film. Then, we performed some finite element simulations trying to reproduce the experimental maps. We believe our simulation scheme is helpful for designing the photonic components, e.g., to predict the local changes in the refractive index due to the photoelastic effect.

Résumé

Les couches minces à base de nitrure de silicium (SiN_x) ont été reconnus comme des diélectriques essentiels dans l'industrie microélectronique et optoélectronique en raison de leurs propriétés intéressantes. Dans cette thèse, nous décrivons comment contrôler l'indice optique et les propriétés mécaniques des couches de SiN_x et d'oxynitrure de silicium (SiO_yN_x) en ajustant les paramètres du processus de dépôt. Nous utilisons deux types de réacteurs de dépôt chimique en phase vapeur assisté par plasma : un réacteur standard à couplage capacitif avec excitation radiofréquence et un réacteur à résonance cyclotron électronique avec excitation micro-onde. Nous discutons de la fabrication et de la caractérisation des structures multicouches comme application optique de nos couches minces. Nous focalisons sur la caractérisation et la compréhension des propriétés optiques de ces couches minces grâce à l'ellipsométrie spectroscopique. Nous étudions également expérimentalement leurs propriétés mécaniques en utilisant la technique de mesure de la courbure des substrats, la fabrication de microstructures et les mesures de nanoindentation.

Enfin, nous montrons des mesures précises de la distribution des contraintes induites dans le GaAs lorsque de tels couches minces sont structurés sous forme de rubans allongées de largeur variable, en utilisant la lithographie optique et la gravure au plasma. Pour cela, nous cartographions la déformation anisotrope, en mesurant le degré de polarisation de la photoluminescence (PL) à intégration spectrale générée au sein du GaAs par excitation avec un laser rouge. La PL des semi-conducteurs cubiques massifs tels que le GaAs n'est pas polarisé, tandis que sous une contrainte anisotrope un certain degré de polarisation est produit. Ces cartographies ont été mesurées soit à partir de la surface du semi-conducteur, soit à partir de sections transversales clivées. Ils fournissent une image détaillée et complète de la déformation cristalline au voisinage de la couche contrainte structurée. Ensuite, nous avons effectué des simulations par éléments finis en essayant de reproduire les cartographies expérimentales. Nous pensons que notre schéma de simulation est utile pour la conception des composants photoniques, par exemple pour prédire les changements locaux de l'indice de réfraction dus à l'effet photoélastique.

Contents

List of Figures

List of Tables

Acronyms

Ar	Argon
CC	Capacitively Coupled
CCP	Capacitively Coupled Plasma
CMC	Continuous Multi-Cycle
CMOS	Complementary Metal-Oxide-Semiconductor
CMP	Chemical-Mechanical Polishing
CTE	Coefficient of Thermal Expansion
DOLP	Degree Of Linear Polarization
DOP	Degree Of Polarization
ECR	Electron Cyclotron Resonance
GaAs	Gallium Arsenide
Ge	Germanium
HH	Heavy Hole
InP	Indium Phosphide
LH	Light Hole
LPCVD	Low-Pressure Chemical Vapor Deposition
MOSFET	Metal-Oxide-Semiconductor Field-Effect Transistors
MW	Microwaves
N_2	Molecular Nitrogen
NH_3	Ammonia
O_2	Oxygen
OPTS	Optimized Thickness Structure
PECVD	Plasma-Enhanced Chemical Vapor Deposition
PL	Photoluminescence
QW	Quantum Well
QWS	Quarter-Wave Thickness Structure
RF	Radio Frequency
sccm	Standard Cubic Centimeters per Minute
SEM	Scanning Electron Microscopy
SF_6	Sulfur Hexafluoride
Si	Silicon
Si_3N_4	Stochiometric Silicon Nitride
SiH_4	Silane
SiO_2	Stochiometric Silicon Dioxide
TE	Transverse Electric
TM	Transverse Magnetic
TMAH	Tetramethylammonium Hydroxide
VASE	Variable Angle Spectroscopic Ellipsometry

Portions of this work have been published in:

Journal of Vacuum Science & Technology B

DOI: 10.1116/6.0001352

1. Introduction

Dielectric thin films such as silicon dioxide SiO_2 and silicon nitride Si_3N_4 are integral to many microelectronic, photonic, and optical devices. They are used for their interesting electrical, optical, mechanical, and thermal properties[1–4]. We can find them in transistors, memories, optical waveguides, semiconductor lasers, and solar cell applications as insulating, anti-reflection, or passivating coatings. There are various deposition techniques to fabricate such dielectric films, among which plasma-enhanced chemical vapor deposition (PECVD) is widely used to deposit hydrogenated amorphous dielectric films at low temperatures (<300 °C) compatible with several materials sensitive to high temperatures such as III-V semiconductors or flexible substrates [5]. PECVD reactors offer a high tunability of films' properties according to the deposition parameters. Therefore, it is possible to combine several physical characteristics and give several functions to the same dielectric films by controlling their deposition conditions.

We can also modify the films' optical properties to fabricate optical devices such as optical filters or waveguides by modifying their density or stoichiometry. We can change their mechanical and tribological properties to enhance the performance and reliability of some semiconductor materials. For instance, it is possible to introduce intentional residual stresses in dielectric thin films grown on semiconductors to

increase carrier mobility in complementary metal-oxide-semiconductor (CMOS) devices [6], so-called strain engineering.

Strain engineering was proven to help improve advanced CMOS technologies [7]. Thus, understanding the impact of strain on the optical properties of materials is essential to developing integrated photonic circuits and facilitating their industrialization on a large scale. On the one hand, unintentional mechanical stress in semiconductor devices causes undesirable deformations and complicates certain components' designs. These mechanical stresses are thus considered a limiting factor that reduces the performance and the lifetime of photonic devices. On the other hand, the controlled mechanical strain generated by a thin dielectric film can modify the properties of semiconductor devices on-demand, opening the way to developing new concepts in materials engineering.

Examples of the positive impact of strain engineering on optoelectronic devices are discussed in the next part.

1.1. Strain engineering in optoelectronics

Integrating dissimilar materials such as Si, Ge, III-V semiconductors, and Si-based dielectric thin films is important to the fabrication of optoelectronic devices. Combining all these heterogeneous materials on an industrial level presents new challenges in fabrication, characterization, and modeling. In this work, we are mainly interested in the role strain engineering can play in enhancing the performance of optoelectronic devices.

For example, strain in semiconductor waveguides can change the geometrical properties of the optical mode, change a single-mode waveguide into a multimode one, change the waveguide's polarization properties, and affect its propagation losses [8]. Strain engineering also allows the easy fabrication of photoelastic waveguides used in a wide range of semiconductor devices, such as electro-optical modulators [9], directional couplers [10], semiconductor laser diodes [11], and integrated optical devices in general.

It is known that etching and ion-implantation significantly affect the material's structure by changing the surface topology [12] or implantation-induced damage [13], respectively. Thus, waveguides technologies using these processes set restrictions on the design because it is necessary to maintain the material's surface intact to allow the integration of other devices in the vicinity of waveguides.

For that reason, photoelastic waveguides seem particularly interesting as an alternative technology for generating planar waveguides that do not require doping or

damaging the substrate and leave the material surface intact. Photoelastic waveguides use the photoelastic effect to change the refractive index of the guiding layer using a controlled mechanical deformation induced by a stressor layer. We also use photoelasticity in some applications to experimentally determine stress distribution in stressed materials [14].

Westbrook et al. [15] reported photoelastic waveguides in GaAs-based structures, as shown in Figure 1.

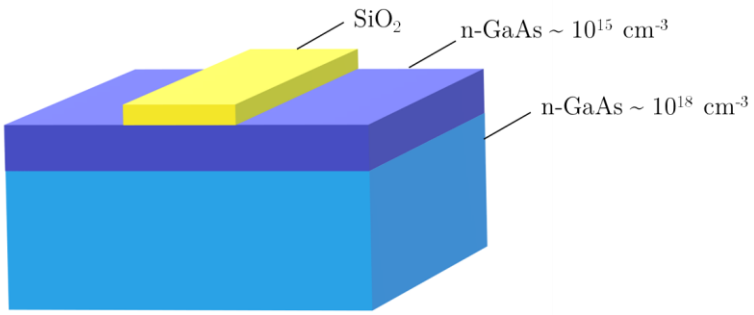

Figure 1: Photoelastic waveguides using a compressive SiO_2 stressor stripe deposited onto a surface planar waveguide in a GaAs-based structure [15].

The photoelastic waveguide is produced by introducing strain locally into a semiconductor material by depositing a SiO_2 stressor layer in compression onto a planar GaAs waveguide structure. The deformation of the semiconductor induces variations in the refractive index beneath the stressor stripe. We note that the guiding layer's photoelastic properties and the stressor stripe's nature define the shape of the guiding regions and the properties of the waveguide. For example, the same work [15] demonstrated

that the number of guided modes in these waveguides depends mainly on the stripe width.

We also find strain engineering in physics related to the quantum confinement of charge carriers. It has become a powerful tool to tune optoelectronic characteristics, such as gain and polarization of stimulated emission of quantum well (QW) lasers. An epitaxial strain is generally introduced in QWs during the growth of active layers to optimize the performance of diode lasers and increase their gain [16]. As a result, strained lasers need less current modulation to obtain a given modulation in the output power and can operate at higher modulation frequencies.

The strain changes not only the gain but also the polarization of the emitted light from the QWs. It has been reported in [17] that compressively strained QWs amplify light polarized in the plane of the well, i.e., in the transverse electric (TE) mode. In contrast, QWs in tensile strain provide more gain to light polarized in the direction perpendicular to the plane of the well, in the transverse magnetic (TM) mode. Therefore, if we can locally control the stress in a multilayer structure of QWs by alternating layers in compression and tension, as shown in Fig. 2a, we can produce a mechanically stable QW structure that amplifies both polarizations equally [17], [18]. For instance, Fig. 2b shows that we can build a polarization-insensitive semiconductor optical amplifier over a wide spectral range from 1475 nm to 1575 nm.

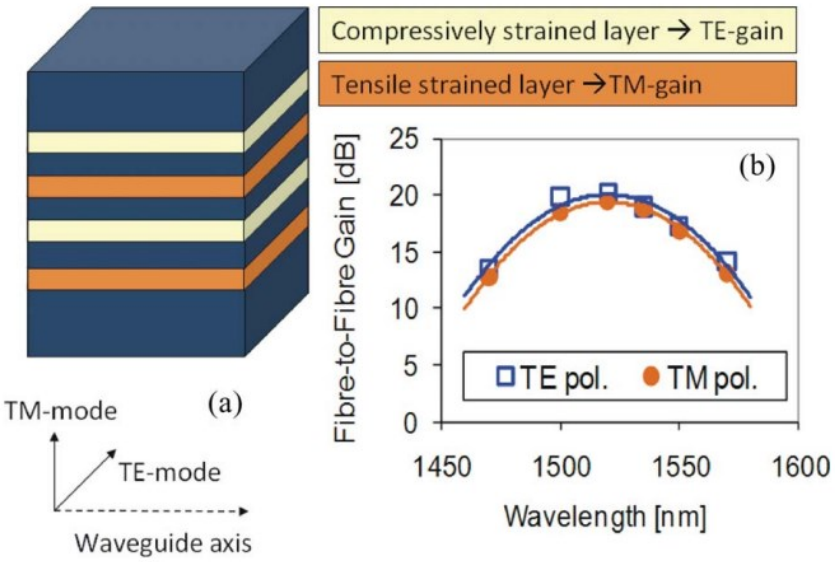

Figure 2: A series of compressive and tensile films can be designed to be mechanically stable (a) and equally amplify both TE and TM modes to produce polarization-insensitive semiconductor optical amplifiers as shown in (b) [16–18]

Here we only underline the importance of strain engineering in designing optimized optoelectronic devices. Many other examples of strain engineering applications in optoelectronics can be found in the literature [19,20].

1.2. Thesis objectives and methods

Among the many interesting properties of dielectric films, the optical and mechanical properties of amorphous silicon nitride SiN_x and silicon oxynitride SiO_xN_y films mainly attracted our attention in this Ph.D. project.

The objective of this thesis is to understand the main factors contributing to tuning the properties of PECVD SiN_x-based films to fabricate optically functionalized multi-layer structures and increase the knowledge of strain distribution generated by dielectric thin film structures on semiconductor substrates. Hence, we help develop efficient strain engineering techniques for optoelectronic devices such as optical filters and photoelastic waveguides.

This research project is being developed in a Canadian – French collaboration framework, including studies with different deposition techniques based on SiN_x and SiO_xN_y dielectric thin films. We have used two PECVD reactors: a commercial capacitively coupled (CC)-PECVD reactor (Corial D250) located at the Nano-Rennes facility, within INSA Rennes in France and a "custom-designed" electron cyclotron resonance (ECR)-PECVD reactor located at McMaster University in Canada.

In this work, we describe how we control the refractive index, residual stresses, elastic modulus, and hardness of SiN_x-based films by tuning certain PECVD process parameters. Then, we investigated the optical properties of thin films using variable angle spectroscopic ellipsometry (VASE). The thin films' mechanical properties, such as

residual stress, hardness, and Young's modulus, were mainly estimated from wafer curvature and nanoindentation measurements. These characterizations allowed us to have ideal conditions to adjust the optical properties of our films and fabricate optically functionalized multilayer structures. We were also able to deposit thin films with well-controlled mechanical stress used as stressor layers on different substrates.

We studied the impact of strain generated by a structured stressor SiN_x film at the surface of III-V bulk semiconductors using spatially resolved photoluminescence (PL) measurements. We also compared the experimental measurements with the simulation results obtained by COMSOL Multiphysics®.

This research emphasizes the importance of controlling all the steps (simulation, fabrication, and characterization) of the overall strategy to predict better the final characteristics of optical and photonic devices using strain engineering.

1.3. Academic achievements

1.3.1. Journal publications

Journal articles that contribute to the work presented in this thesis are as follows:

Brahim Ahammou, Aysegul Abdelal, Jean-Pierre Landesman, Christophe Levallois, Peter Mascher. *"Strain engineering in III-V photonic components through structuration of SiN_x films"*. Journal of Vacuum Science & Technology B, Nanotechnology and Microelectronics: Materials, Processing, Measurement, and Phenomena, 2022, vol. 40, no 1, p. 012202.

Emmanuel Schaub, **Brahim Ahammou**, and Jean-Pierre Landesman, *"Polarimetric photoluminescence microscope for strain imaging on semiconductor devices"*. Applied Optics 61.6 (2022): 1307-1315.

Solène Gérard, Merwan Mokhtari, Jean-Pierre Landesman, Christophe Levallois, Marc Fouchier, Erwine Pargon, Philippe Pagnod-Rossiaux, François Laruelle, Alain Moréac, **Brahim Ahammou**, Daniel T. Cassidy. *"Photoluminescence mapping of the strain induced in InP and GaAs substrates by SiN_x stripes etched from thin films grown under controlled mechanical stress"*. Thin Solid Films, 2020, vol. 706, p. 138079.

Brahim Ahammou, Christophe Levallois, Jean-Pierre Landesman, Peter Mascher. *"Mechanical and Optical Properties of Amorphous Silicon Nitride Based Films Prepared by ECR PECVD"*. Thin Solid Films [Under Review]

Paramita Bhattacharyya, **Brahim Ahammou**, Fahmida Azmi, Rafael Kleiman, Peter Mascher. *"Design and Fabrication of Color-generating Nitride based Thin-Film Optical Filters for Photovoltaic Applications"* Journal of Vacuum Science & Technology A [Under Review]

1.3.2. Conference oral presentations

Oral presentations that contribute to the work presented in this thesis are as follows:

Brahim Ahammou, Aysegul Abdelal, Christophe Levallois, Jean-Pierre Landesman, Peter Mascher. *"Mechanical and Optical Properties of Amorphous SiN-Based Films Prepared by ECR PECVD and CCP PECVD"*. In: 239th ECS Digital Meeting, May 30, 2021.

Brahim Ahammou, Aysegul Abdelal, Solène Gérard, Christophe Levallois, Peter Mascher, Jean-Pierre Landesman. *"Stress Engineering of Dielectric Films on Semiconductor Substrates*". In: 239th ECS Digital Meeting, May 30, 2021.

Brahim Ahammou, Paramita Bhattacharyya, Fahmida Azmi, Christophe Levallois, Jean-Pierre Landesman, Peter Mascher. *"PECVD Silicon Nitride-Based Multilayers with Optimized Mechanical Properties"*. In: 241st ECS Meeting (May 29-June 2, 2022), Vancouver, British Columbia, Canada.

Brahim Ahammou, Aysegul Abdelal, Denis Laillé, Christophe Levallois, Jean-Pierre Landesman, Peter Mascher. *"Characterization of Silicon Nitride Thin Films Deposited by PECVD using Microstructures*". In: FCSE Symposium, June 2021, Montreal, Quebec, Canada.

Paramita Bhattacharyya, **Brahim Ahammou**, Fahmida Azmi, Rafael Kleiman, Peter Mascher. *"Design and Fabrication of Multiple-Color-Generating Thin-Film Optical Filters for Photovoltaic Applications"*. In: 241st ECS Meeting (May 29-June 2, 2022), Vancouver, British Columbia, Canada.

Fahmida Azmi, **Brahim Ahammou**, Paramita Bhattacharyya, Peter Mascher. *"Optical and Mechanical Properties of Europium-Doped Silicon Oxynitride Thin Films"*. In: 241st ECS Meeting (May 29-June 2, 2022), Vancouver, British Columbia, Canada.

2. Strain Engineering of Thin Films

2.1. Introduction

Strain engineering is a mechanical approach to modifying the physical properties of semiconductors on demand. This Chapter provides a brief overview of the most common strain engineering applications in semiconductor devices. For this reason, we discuss how strain impacts the properties of semiconductor crystals. Then, we discuss the stress-transfer techniques used in the semiconductor industry to introduce a controlled strain in crystalline and amorphous thin films. As our work mainly focuses on stress generation in amorphous SiN_x-based stressor layers fabricated by PECVD, we also present in this Chapter the CC-PECVD and ECR-PECVD reactors used during this Ph.D. project.

2.2. Strained semiconductors

The effect of strain on semiconductors has been studied since the 1950s. Shockley and Bardeen introduced in their paper the gradual shifts in energy bands resulting from the crystal lattice deformations under stress [21]. Nevertheless, the mechanical strain was mainly related to undesirable defects, dislocations, impurities, and delamination. A few decades later, some studies [22,23] showed a mobility enhancement in strained $Si/Si_{1-x}Ge_x$ metal-oxide-semiconductor field-effect transistors (MOSFET) caused by the lattice mismatch in the epitaxial heterostructures. Thus, strain engineering became

very useful to improve carrier transport efficiency in transistors and advanced CMOS devices. As shown in Fig. 3, the hole mobility increases as a function of the longitudinal channel uniaxial tensile strain in p-MOSFETs.

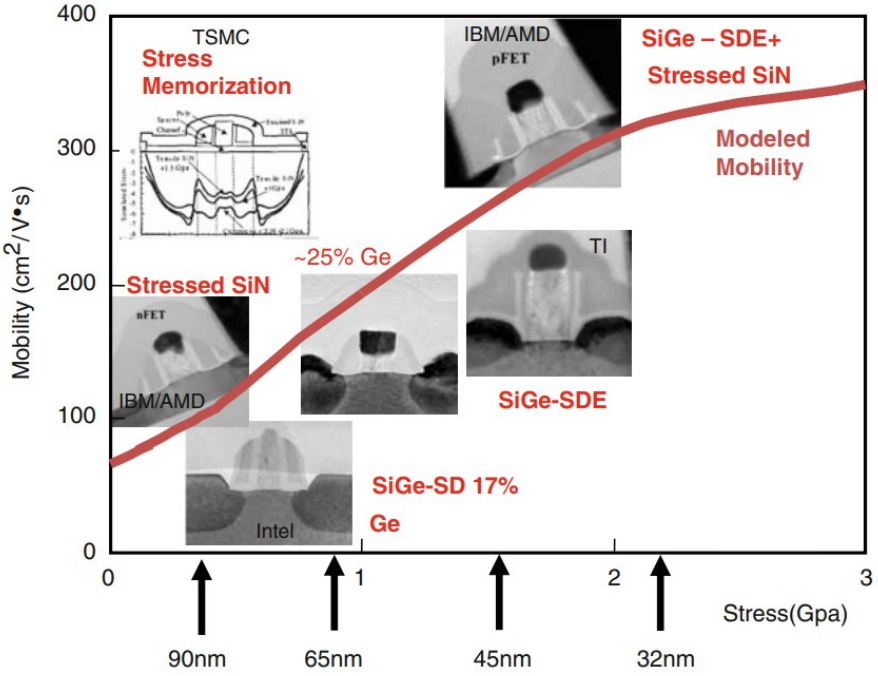

Figure 3: Strain technology for p-MOSFETs in different Si technology nodes. The line in the Figure represents the modeled hole mobility as a function of longitudinal channel uniaxial tensile strain [7].

Intel adopted the first major strained-Si technologies to enhance microprocessor performances using strained transistors. The first strained Intel 90nm node MOSFET was presented by Ghani et al. in 2003 [6]. Several stress-transfer techniques have been used to apply increasingly high stresses on MOS structures. We note that wafer-based biaxial strain produced by epitaxial heterostructure has been combined with stressed

SiN_x films to obtain significant advances in the hole mobility in the IBM and AMD p-MOSFETs [24], see Fig. 3.

Since the emission of photons is caused by electron-hole recombination and involves two electronic states, we need to investigate the electronic state properties of materials to determine their photonic properties. In direct gap materials such as GaAs and InP, electrons move from the valence band to the conduction band by exchanging only photons. However, in indirect gap materials such as Si and Ge, carriers must interact with a phonon and a photon to modify their wave vector, making the transition much less likely at room temperature. Thereby, direct bandgap materials are more often used in active optoelectronic devices. To understand the impact of stress on light emission and absorption, we need to investigate the effect of strain on the band structure of semiconductors.

Despite their indirect bandgap, group IV semiconductors have attracted much interest in fabricating light sources for silicon photonics applications. It has been shown in some studies that strain can transform an indirect bandgap semiconductor such as Ge into a direct bandgap semiconductor using a SiN_x stressor layer in compression [25,26]. The SiN_x stressor layers are mainly used for their CMOS compatibility, low-temperature deposition method (below 300 °C) and can be suitable for some metastable alloys such as $Ge_{1-x}Sn_x$. Fenrich et al. [27] demonstrated tensile-strained pseudomorphic $Ge_{0.934}Sn_{0.066}$/Ge quantum wells in a microdisk resonator using a compressive SiN_x cladding. A cross-section of the resulting hydrostatic strain, induced by the stressor SiN_x

layer, is shown in Figure 4a, excluding initial epitaxial strains. We notice that the stressor layer in compression induces a tensile (positive) strain on the structure after relaxation.

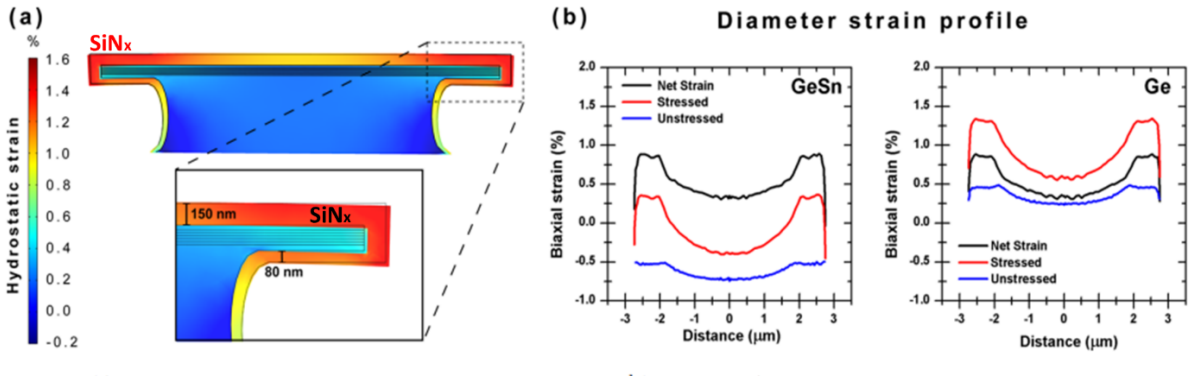

Figure 4: (a) Cross-section of the 3D finite element model showing the hydrostatic strain of a microdisk induced by the SiN_x stressor layer; the initial epitaxial strains are not included. (b) Simulated biaxial strain profiles along the microdisk diameter for the top GeSn QW and the top Ge cap layer, accounting for initial epitaxial strains. [27]

The hydrostatic and biaxial strain distributions are studied through finite element simulation (Fig. 4a) and show local biaxial strain transfers as high as 1.3 % at free-standing microdisk edges in Fig. 4b. According to deformation potential theory, these strains are sufficient to overcome the original compressive strain in $Ge_{0.934}Sn_{0.066}$ epitaxy and reach a direct band gap configuration [27]. Ge is an indirect bandgap semiconductor, with a valence band maximum at the Γ-point (k=0) of the reciprocal space and a conduction band with several minima, two of which are very close in energy at the Γ-point and *L*-point [28]. The offset between the indirect and the direct gap in Ge

is about 140 meV compared to silicon's 2.28 eV [28]. Some simulation-based studies have shown the possibility of turning Ge into a direct bandgap semiconductor by applying a tensile strain of 2 % [29,30]. Usually, SiN_x stressor layers are added to obtain enough hydrostatic strain to reduce the bandgap and enough shear strain to lift the degeneracy at $k = 0$ of the heavy hole (HH) and light hole (LH) valence bands. We can describe the band degeneracies depending on the nature of the stress. Nevertheless, we cannot predict which bands will gain or lose energy. Hence the importance of using techniques such as the tight-binding or k.p perturbation theory to predict, for example, how HH and LH bands warp [31]. It has been demonstrated that biaxial compressive strain applied to a bulk direct bandgap semiconductor will split the degeneracy so that the LH gain energy and HH lose energy. The opposite was observed for tensile strain, see Fig. 5.

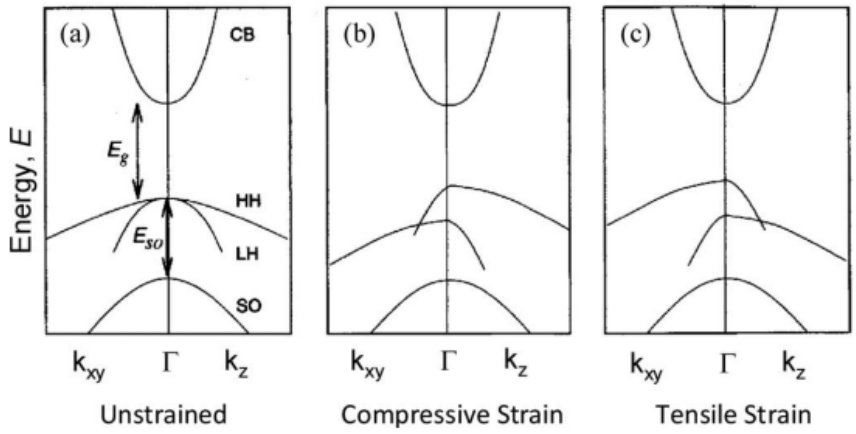

Figure 5: In direct bandgap bulk unstrained semiconductors (a), the HH and LH bands degenerate at the valence band maximum at the Brillouin zone center Γ. *Compressive strain splits the degeneracy so that the highest band is light in the x-y plane of the layer but*

heavy in the z-direction, as shown in (b). The opposite situation is observed for tensile strain, as shown in (c). [16]

These modifications in the energy band structure of materials lead to radical changes in their optical properties, affecting optoelectronic devices' performance, such as emission wavelength, gain, and quantum efficiency [16]. Strain engineering is used in QW lasers to improve their performance and make them capable of emitting light with desirable polarization by introducing epitaxial strain in active layers.

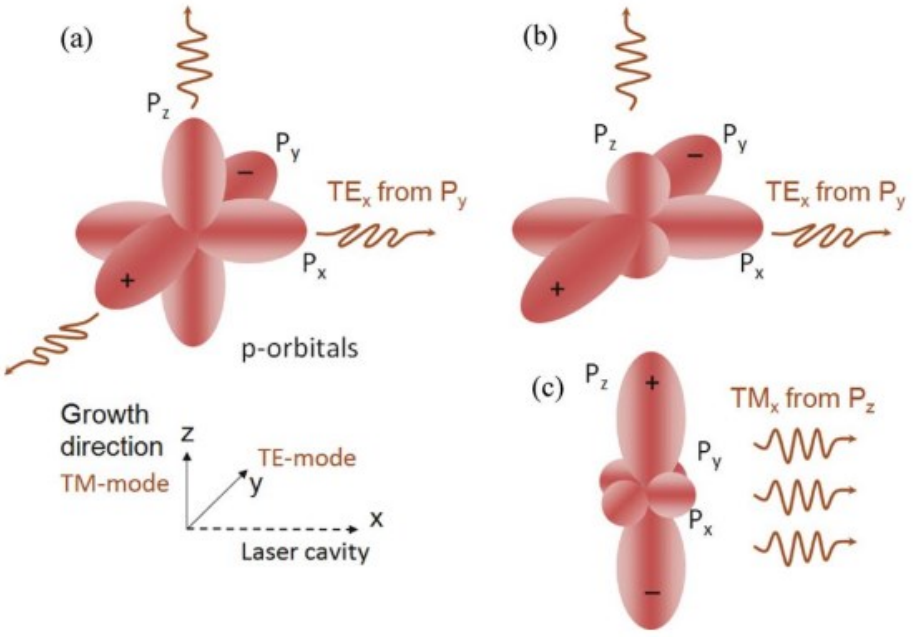

Figure 6: A qualitative illustration showing three p-orbitals P_x, P_y, and P_z of equal size for an unstrained bulk semiconductor (a). The variation of the p-orbitals size under biaxial compression is shown in (b), and under biaxial tension in (c). [16]

Figure 6 illustrates qualitatively the impact of strain on the size of the three p-orbitals, P_x, P_y, and P_z, of a bulk direct bandgap semiconductor. First, Fig. 6a shows an unstrained semiconductor, where holes at the valence band maximum are equally distributed among the three p-orbitals. Thus, P_x, P_y, and P_z contribute the same to photoluminescence (PL). However, when biaxial compressive stress is introduced, the number of holes in the P_y orbital increases (see Fig. 6b), and the PL light is linearly TE polarized in the x-direction. Under a biaxial tensile strain, almost all holes are in the P_z orbital (see Fig. 6c), and the semiconductor emits TM polarized PL light in the x-direction.

We note that the polarization of PL depends on the nature, amplitude, and anisotropy of the applied stress. Therefore, several characterization techniques of strain are based exclusively on the study of PL in semiconductors. In micro-PL spectroscopy, the applied stress will shift the PL spectrum [32], providing information on the hydrostatic component of strain. At the same time, a measurement of the degree of polarization (DOP) of PL gives us information about the anisotropic component of the strain [32–34].

Si, GaAs, and InP have a single isotropic refractive index since they have cubic crystal symmetry in the undeformed state. However, strain modifies the crystal electronic structure on a microscopic scale by changing the bond lengths between the atoms, altering the polarizability of strained semiconductors. For example, a non-hydrostatic strain transforms the refractive index into a matrix with some degree of anisotropy.

According to photoelastic theory [35], a linear approximation of the change in the inverse dielectric function with strain can be described by the photoelastic tensor of the material. The variation in the refractive index ellipsoid n_{ij} can be related to the strain ε_{ij} in terms of the photoelastic tensor p_{ij} as:

$$\Delta\left(\frac{1}{n^2}\right)_i = p_{ij}\varepsilon_j \tag{1}$$

where p_{ij} are the photoelastic constants of the material. In our case, the symmetry of the cubic crystals such as GaAs, InP, Si, and Ge reduces the number of independent photoelastic constants to only three p_{11}, p_{12} and p_{44}.

Photoelasticity also deals with the birefringence developed in a solid under anisotropic mechanical strain. In fact, it is a powerful tool for designing polarization-insensitive optical waveguide devices considering the stress-induced effects [36].

Strain engineering uses a combination of different techniques to apply strain on semiconductor materials and modify their properties. Therefore, we need to discuss the various methods used to apply controlled stress in semiconductor devices to take advantage of all the benefits of strain engineering.

2.3. Stress transfer methods

Residual mechanical stresses can be associated with many parameters during the fabrication of semiconductor devices. Strain can be induced throughout the process steps by Chemical-Mechanical Polishing (CMP) [37], ion implantations [38], thermal annealing [39], and intrinsic stresses in thin films. However, we only study intentional residual stresses in this part. We describe two approaches for introducing strain in semiconductor devices: a global one, where stress is generated across the entire substrate's surface by epitaxial growth in lattice-mismatch systems, and a local approach, where stress is engineered into the devices by structured dielectric stressor layers.

Global residual stress generally arises due to a lattice mismatch between an epitaxial film and a substrate. For example, we can deposit a crystalline Si layer on a relaxed $Si_{1-x}Ge_x$ substrate with a larger lattice constant to apply a tensile strain on the Si layer. Thus, the amount of strain in the crystalline Si layer can be controlled by the Ge concentration in the $Si_{1-x}Ge_x$ substrate. Experimentally, it has been found that tensile biaxial stress improves electron mobility and compressive biaxial stress improves hole mobility in strained Si [6]. Global stress-transfer techniques have, however, some limitations in applying both tensile and compressive stress on the same substrate for different devices such as n-MOSFETs and p-MOSFETs.

In optoelectronics, several global tensile stress-transfer methods into Ge crystalline layers have been investigated in the literature [40] to create active photonic

components such as lasers into Si-compatible platforms. However, they are not all easy to integrate on CMOS-integrated devices.

However, local stress-transfer techniques use stressor layers that apply controlled stress on specific substrate regions, allowing strain control in every device on the same substrate. It is possible to create stressor layers either by a thermal mismatch or by producing layers with built-in stress. We can select the type, amplitude, and region for the applied strain using lithographic patterning of different layers with different properties. After etching patterns on the stressor films, the structures will relax and induce local deformations in the substrate. Later in this work, we will discuss the influence of this deformation field on direct bandgap semiconductors.

The local stress-transfer techniques using amorphous SiN_x-based films are flexible for strain engineering, and we discuss why in the following part.

2.4. SiN_x-based thin stressor films

SiN_x-based films are widely used in the microelectronics and optoelectronics industries. Here we will discuss how we can tune their properties and explain the mechanisms for stress generation during the deposition of these films.

2.4.1. Silicon nitride properties

Silicon nitride films are used as insulators in thin-film transistors, as passivation layers to protect integrated circuit devices from moisture and ion contamination [41], and give interesting properties to integrated optical devices [42].

We can fabricate stoichiometric and thermally stable polycrystalline Si_3N_4 films using low-pressure chemical vapor deposition (LPCVD) at temperatures between 600 and 900 °C where hydrogen is evaporated from the films because of the high temperature. However, it is challenging to integrate these films in many applications where high temperatures can damage devices, so instead, we focus in this work on hydrogenated amorphous SiN_x films deposited at low temperatures (less than 300 °C) using PECVD. Numerous parameters must be controlled to ensure high quality and reproducibility in PECVD processes, such as the excitation power and frequency, nature of precursors, concentration and gas flows, plasma pressure, and substrate temperature.

It is interesting to note that thin films give access to many unusual properties that are impossible with macroscopic materials. Therefore, it is not easy to define unique physical properties for these films as they can vary significantly as a function of the

deposition condition. Usually, we use a set of multilayers in the same optical or electronic device to obtain more complex functionalities. Later in this thesis, we will discuss how optical filters can be fabricated from a stack of SiN_x-based films with different refractive indices. The tunability of the refractive index of SiN_x-based films depends mainly on the fabrication parameters of the films [33]. We can obtain various properties on demand by changing the silicon/nitrogen ratio or the hydrogen incorporation in the SiN_x films. For example, it is possible to lower the nitrogen incorporation in SiN_x films to increase the refractive index approaching that of amorphous silicon. We can also introduce oxygen in SiN_x films to reduce their refractive index approaching that of silicon oxide. This flexibility allows the fabrication of a wide range of photonic devices such as solar cells' antireflective coatings, waveguides, and others [43].

One of the important differences between SiN_x deposited using a plasma deposition and Si_3N_4 films obtained from a high temperature chemical vapor deposition is the percentage of hydrogen incorporation. Introducing hydrogen into SiN_x films modifies their structure and density, passivates dangling bonds [44], and reduces the films' hardness [45].

Table 1 shows the possible bonds in hydrogenated amorphous SiN_x PECVD films and their associated bond energies.

Table 1: Bond energies in PECVD silicon nitride [46].

Bonds	Energies (eV)
Si-Si	2.34
Si-N	3.45
N-N	1.70
Si-H	3.10
N-H	4.05

The SiN_x films are generally deposited using hydrogenated precursors such as SiH_4 and NH_3 which leads to the presence of Si-N, Si-H, Si-Si, and N-H bonds, as shown in Table 1. Their configuration depends strongly on the stoichiometry of the films [47,48]. N-H bonds are especially problematic because they act as absorption centers that lead to undesirable losses at λ ~1550 nm as discussed in Ref.[49].

The hydrogen impurities incorporated in PECVD SiN_x films come mainly from the hydrogen present in the deposition precursor gases such as SiH_4 and NH_3. Generally, NH_3 is used as a precursor in standard PECVD recipes for SiN_x. However, we can use N_2 instead to reduce the available hydrogen in the plasma during thin films' growth. This modified recipe, often called NH_3-free PECVD, has been demonstrated to be an

excellent alternative to obtaining layers with low hydrogen content and propagation losses close to 2 dB/cm without needing high-temperature annealing [49]. Although we cannot eliminate the presence of hydrogen due to the decomposition of SiH_4, we can assume that the hydrogen level in NH_3-free films is low.

Furthermore, it is possible to achieve even lower propagation losses if we optimize the process parameters for that purpose. In addition to their interesting optical properties, we can control the mechanical properties of SiN_x-based films by modifying the process parameters. Thus, amorphous SiN_x-based films can be used as stressor layers in many optoelectronic applications in the framework of strain engineering, as discussed earlier. Therefore, we need to understand the mechanism of stress generation and how to control mechanical stress in these films.

2.4.2. Origin of residual stress in amorphous films

Many studies have been dedicated to understanding the internal stress generation in amorphous films [50][51]. Most publications have reported the participation of two components for the residual stress in thin films: thermal stress and intrinsic stress.

The thermal mismatch between the film and the substrate generates stressed films due to the temperature variation between deposition and room temperature and the difference between the thermal expansion coefficients of the two materials [52]. Hence, the deposition of a thin film at a given temperature on a thick substrate causes mechanical stresses to appear when the system gets to room temperature.

However, intrinsic stresses appear at the deposition temperature, and according to Johlin et al. [50], they are mainly the consequence of two components. A compressive component is related to ion bombardment during deposition, and a tensile component is associated with the film porosity. Therefore, the deposited films are either tensile or compressive, depending on the nature of the material deposited and the operating conditions [53–55], such as deposition temperature, deposition power, and partial pressures of the reactive gases. Many models make it possible to explain the presence of these residual stresses [56].

First, we will discuss the suggested models to explain the presence of tensile stresses in polycrystalline and amorphous films. One of the most cited models to explain the causes of this effect in polycrystalline films is Hoffman's "grain boundary relaxation"

mechanism, where a reduction in interfacial energy occurs when individual crystallites join to form a grain boundary [57]. Nix and Clemens [56] relied on Hoffman's theory to develop more advanced models that consider the coalescence of grains at the beginning of growth. They considered an array of two-dimensional crystallites with an elliptical shape that merges to form a surface with a cycloid shape, as shown in Fig. 7.

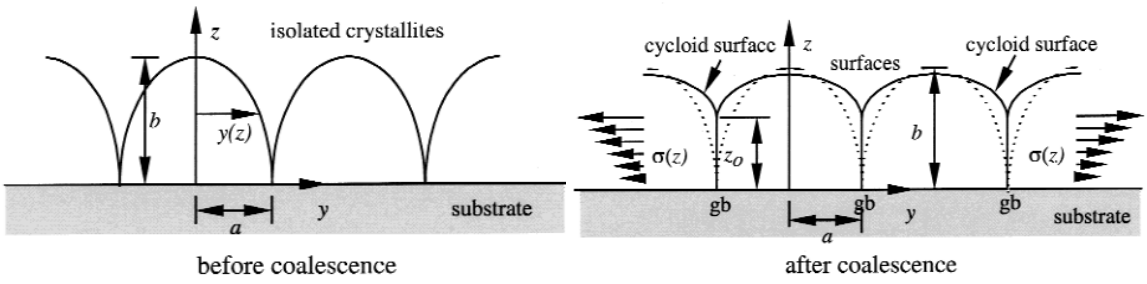

Figure 7: Crystallite coalescence process, showing the elastic displacements and stresses associated with forming a continuous film [56].

This approach is based on crystallite morphology and physical phenomena close to reality. The surfaces of the crystallites spontaneously snap together in a "zipping process" as the grain boundary energy is less than the energies of the free surfaces. Even though Nix and Clemens placed this model in the context of polycrystalline materials, and it is difficult to speak of "grain boundaries" in amorphous films, recent studies have shown that this model can also be applied to tensile stresses in amorphous films. Floro et al. [51] attribute tensile stress in amorphous semiconductor films of Si and

Ge to the "zipping" phenomenon of nanovoids in the film formed between regions of high local bond strain and slightly different densities.

On the other hand, the compressive intrinsic stresses are usually related to the "atomic peening" phenomenon, leading to two main models: Windischmann's [58] and Davis's [59] model. These two models are based on the displacement and implantation of atoms in the volume of amorphous films during the knock-on linear cascade caused by the particles incident on the surface, generating volumetric distortions. Due to the dimensional limitation of the film and its adhesion to the substrate, compressive stresses appear in the film. Davis's model adds to this theory the presence of thermal spikes, i.e., intense local heating in the form of violent atomic movements caused by the ion bombardment, which explains the relaxation of stresses sometimes observed when the ion bombardment during growth is very energetic. For this reason, Davis's model is generally considered to be the most valid among the theories that explain the intrinsic compressive stresses in amorphous thin films.

2.5. Thin-film deposition systems used in the thesis

Plasma can be artificially generated by heating or subjecting a neutral gas to a strong electromagnetic field to the point where the gas becomes ionized and increasingly conductive to electricity. Usually, we do not generate plasmas by heating because the reactors cannot withstand the temperature necessary to ionize the gas and stabilize the plasma. In laboratories, we usually create plasmas by subjecting a gas

mixture to an electrical discharge. Our PECVD reactors use an electromagnetic field to accelerate free electrons within a gas mixture. During the inelastic shocks, between the accelerated electrons and the neutral molecules or atoms present within the gas, an avalanche of charged particles is created, and the gas molecules are ionized. The gas goes from an electrically insulating state to a conductive state by producing charged species. In our work, we are interested in process plasmas, which offer an excited atomic state to favor chemical reactions, and modify the surface chemical and physical properties at low temperatures, for example, the etching and deposition plasmas used in the semiconductor industry.

We distinguish different types of plasmas according to the excitation frequency: low frequencies (10 to 100 kHz), radio frequency RF (1 MHz to 500 MHz), and very high frequencies "microwaves MW" (0.5 GHz to a few GHz). Depending on the frequency used, it is possible to favor ion bombardment on the substrate and control the deposition rate, film composition, and properties. We focus in this work on a CC-PECVD reactor with an RF excitation frequency and an ECR-PECVD reactor with an MW excitation frequency.

2.5.1. Capacitively Coupled (CC) PECVD

In this work, we have used a commercial Corial-D250 CC-PECVD reactor composed of two electrodes in parallel with a spacing between them, where a mixture of SiH_4, NH_3, and Ar was injected. The plasma was ignited with a voltage excitation frequency of 13.56 MHz. When an isolated substrate is inserted into the plasma, it initially receives a high quantity of ions and electrons. However, the flux of each species is not the same due to the much higher mobility of electrons. First, the substrate begins to charge negatively compared to the plasma until it reaches a stationary state. The flow of positive ions towards the substrate, also called ion bombardment, balances the electron flow repelled towards the plasma. A potential barrier surrounds any surface in contact with the plasma; only the most energetic electrons can cross it. Hence, the difference between the electrical potential of the plasma region and the floating potential leads to positive ion bombardment onto the surface of the substrate. This excited atomic state favors chemical reactions and deposits the SiN_x-based films. Later in this work, we present the detailed recipes for each deposited layer and its properties.

2.5.2. Electron Cyclotron Resonance PECVD

In our studies, we have also used an ECR-PECVD reactor composed of a magnetron, waveguide, electromagnet, and an ECR plasma chamber (see Figure 8), where the plasma is generated remotely from the sample. To deposit SiN_x-based films, we used an NH_3-free recipe with a gas mixture of SiH_4, N_2, O_2, and Ar. Then, the plasma is ignited when the electron cyclotron frequency matches the microwave frequency in the plasma chamber. A detailed explanation of the conditions required to satisfy an ECR resonance can be found in [60]. In our case, we coupled the 2.45 GHz MW from the magnetron with an 875 G magnetic field produced through solenoid coils and manually tuned the waveguide's impedance to transfer the maximum MW power to the plasma. The magnetic field inside the ECR chamber confines the plasma radially and brings the charged species to the sample's surface to react and produce the SiN_x-based films. Later in this work, we present the detailed recipes for each deposited layer and its properties.

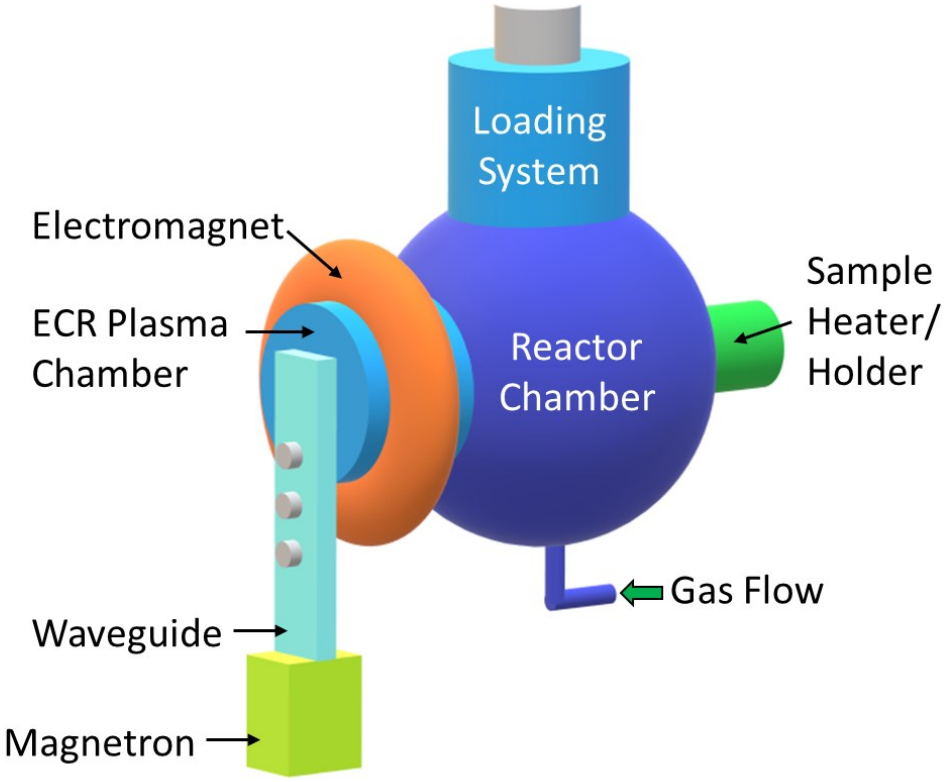

Figure 8: Schematic drawing of the interconnection of the main sub-systems of the ECR-PECVD reactor.

2.6. Conclusions

In this Chapter, we discussed some of the applications of strain engineering in micro-electronic and photonic devices. Then, we discussed how strain affects semiconductors' electrical, optical, and mechanical properties. We have shown a global and a local stress transfer technique to control strain in semiconductor thin films. We also explain the role of amorphous SiN_x-based stressor layers fabricated by PECVD in strain engineering. Finally, we presented the two reactors used for this Ph.D. project.

3. Study of Optical Properties of Silicon Nitride based Thin Films

3.1. Introduction

SiN_x-based thin films received considerable attention in optoelectronics and photovoltaics technologies mainly for their optical properties. Therefore, before adding a stressor layer function to these layers, it is important to ensure that their optical properties remain good. This Chapter outlines the fabrication recipes used to produce SiN_x-based thin films with controlled optical properties and how to modulate the refractive index in a multilayer structure to create optical filters.

First, we give an overview of the principle of ellipsometry since it was the primary characterization tool used in this thesis to determine the optical properties of thin films. Ellipsometry measures quantities that are not directly interpretable as thin films' properties. So, it generally requires certain knowledge of the material to choose a suitable model to fit the ellipsometry data and extract the film's properties. The following part explains the choice of models adapted to our amorphous dielectric thin films.

We will also discuss the impact of process parameters, particularly the gas flows, on the refractive index and optical band gap of our SiN_x-based films. This is followed by a section that presents the fabrication and characterization of a multilayer structure as an optical application of our thin films.

3.2. Presentation of the spectroscopic ellipsometry technique

3.2.1. Principle of ellipsometry

Spectroscopic ellipsometry is a non-destructive optical technique mainly used to determine the optical constants and thickness from a thin film sample by using a model-based approach. As shown in Fig. 9, a linearly polarized light is reflected off the surface of a sample. This reflection induces a phase shift Δ between the p- and s-components of the electric field vector, resulting in an elliptical polarization state. Through the well-known ellipsometry formula, the polarization change can be described by an amplitude ratio ($\tan \Psi$) and the phase shift (Δ):

$$\frac{r_p}{r_s} = \tan \Psi \,.\, e^{i\Delta} \tag{2}$$

where, the r_p and r_s are respectively the complex Fresnel reflection coefficient for p and s polarization.

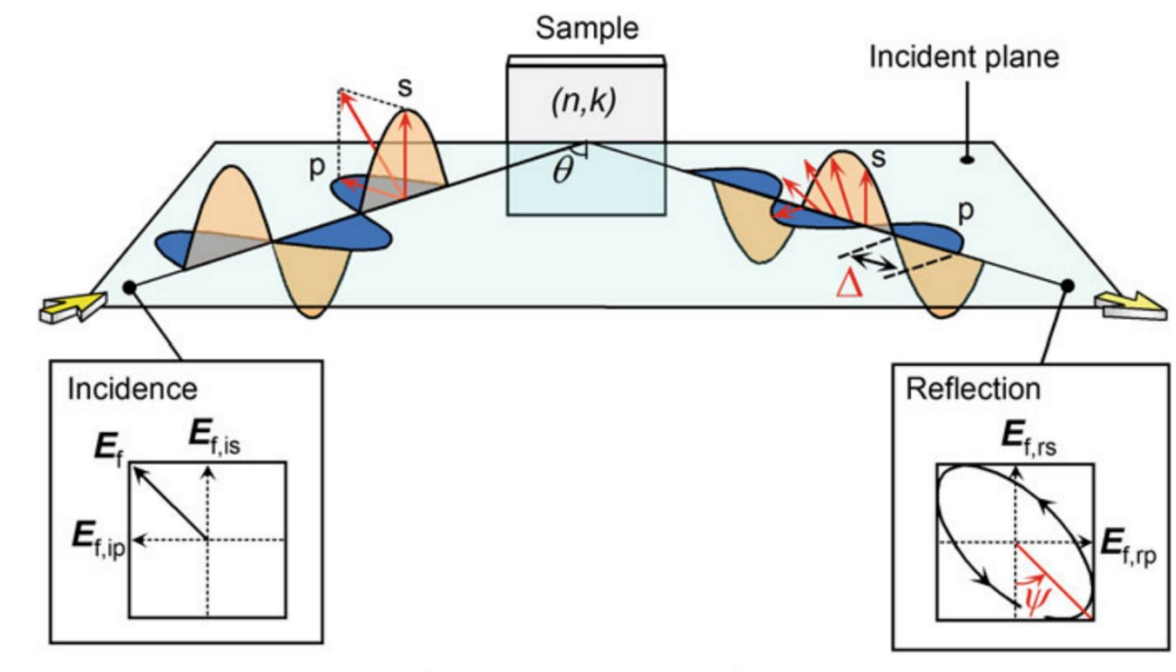

Figure 9: Basic principle of ellipsometry from Fujiwara [61]. *The light polarization is categorized into p- and s-polarizations depending on the oscillatory direction of the electric field (E_f). The p-polarization is parallel to the incident plane, while the s-polarization is perpendicular. The E_f shows the electric field vector, and the subscripts "i", "r", "s", and "p" for E_f denote the incidence, reflection, s-polarization, and p-polarization, respectively.*

The incident angle ϴ is usually selected around Brewster's angle as this provides the most significant ratio between r_p and r_s, increasing the sensitivity of the ellipsometry measurements to thin films. However, we usually measure our samples at multiple angles using variable angle spectroscopic ellipsometry (VASE) to increase the collected information and better estimate our films' properties. For example, the interaction of the light with absorbing films or multilayer structures at different angles provides

more data to be fitted through the models, increasing the accuracy of the properties' estimation.

In this thesis, we have used a Horiba UVISEL 2 and a J.A. Woollam M-2000U ultraviolet-visible ellipsometers to measure the absorption and refractive index of the deposited thin films as well as their thicknesses. We have chosen spectroscopic ellipsometry for its simplicity of measurement and speed of acquisition of an experimental spectrum. It is also a cheap and non-destructive technique to measure our thin films' thickness and the refractive index after deposition. Ellipsometry simultaneously measures Ψ ($\tan\Psi$ proportional to the amplitude ratio) and Δ (phase shift) and precisely determines their values to within $\pm 0.01°$ [61]. Due to the determination of these two parameters, it is not necessary to have a reference measurement in spectroscopic ellipsometry compared to other optical techniques such as reflectance. When thin films are deposited on a substrate, it is necessary to use experimental data modeling to extract meaningful parameters such as refractive index and thickness. Such modeling may sometimes be challenging in samples with a complex structure. For instance, the characterization of multilayer structures requires the knowledge of the optical constants of the individual layers and their distribution in the structure to build a reliable model. We usually need to develop a model of the structure of the studied sample before starting the analysis of ellipsometry data. Further information about the ellipsometry technique can be easily found in many sources [61–63].

As soon as the modeling step is carried out in an appropriate manner, it is then possible to evaluate the sample properties. Among these, we can identify the dimensional properties of a thin film, such as the thickness and roughness of layers or the thickness profile of the different layers forming a multilayer structure. The density, porosity, or even the crystallinity of the films can be deduced from the modeling as well. The next part shows the main models used to characterize our amorphous SiN_x-based films.

3.2.2. Dielectric function of homogeneous semiconductors

Several dielectric function models or dispersion formulas have been developed to allow researchers and technologists to predict the evolution of thin films' optical properties. Since we are using spectroscopic ellipsometry, we are collecting data at multiple energies, and we can use dispersion formulas to fit our data. A dispersion formula is mainly a set of two parametric equations describing the shape of the optical functions (n(E), k(E)) and dielectric functions (ϵ_1(E), ϵ_2(E)) versus energy, which significantly reduces the number of fitting parameters. Knowing which dielectric function models are appropriate for a given set of materials is essential. We mention in the following the main dispersion formulas applied to characterize the optical properties of amorphous dielectric films.

When the thin films are transparent in the wavelengths used for the ellipsometry measurement, $\epsilon_2 \approx 0$, we use the Cauchy model to fit the data.

The Cauchy equation is given by:

$$n = A_2 + \frac{B_2}{\lambda^2} + \frac{C_2}{\lambda^4} + \cdots \ , \qquad k = 0 \tag{3}$$

where A_2, B_2, and C_2 are Cauchy coefficients. The refractive index, n, and the extinction coefficient, k, are related to the dielectric function, $(n + ik)^2 = \epsilon_1 + i\epsilon_2$. All these parameters are fitted using the experimental data. We note that the Cauchy model does not fulfill the Kramers-Kronig relations since the real component of the dielectric function is obtained by assuming that the imaginary component is equal to zero. Therefore, we cannot use the Cauchy model to fit the data at energies below the band gap to evaluate the films' residual absorption. In that case, a harmonic oscillator approximation and dielectric function models can be used. In our study, we have used a semi-empirical model called the Tauc-Lorentz model to better describe the absorption edge of our materials, avoiding an overestimation of ϵ_2 for energies lower than the band gap. The Tauc-Lorentz model is generally used to fit amorphous materials since it can better fit the imaginary dielectric component of such materials. Figure 10 shows an example of a Tauc-Lorentz model that can be used as a starting point to fit the dielectric function of hydrogenated amorphous Si [64].

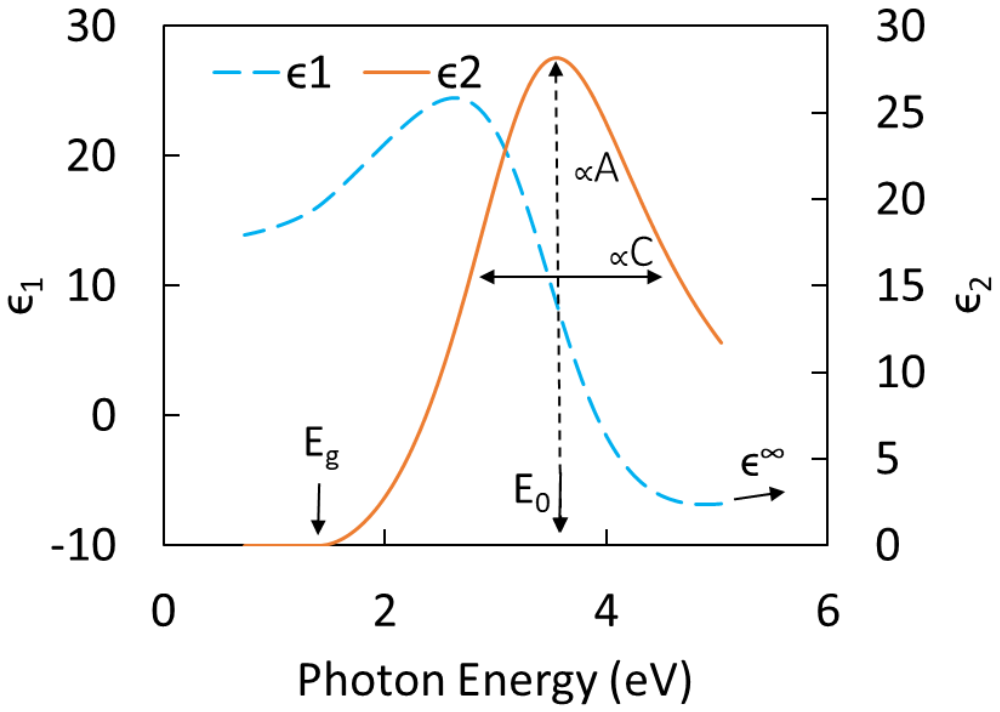

Figure 10: Tauc-Lorentz model. The real (blue dashed line) and imaginary (orange solid line) components are plotted for a model material with $A = 170$ eV, $C = 2.2$ eV, $E_g = 1.39$ eV, $E_0 = 3.5$ eV, and $\epsilon^{\infty} = 0.6$. Produced using CompleteEASE software of the VASE.

In the case of materials with several absorption peaks, such as crystals, it is possible to include their respective contributions using several Tauc-Lorentz oscillators. However, our work mainly characterizes amorphous thin films by adjusting the fit parameters of only one Tauc-Lorentz oscillator. The imaginary part of the Tauc-Lorentz dielectric function ϵ_2 gives the response of the material caused by inter-band mechanisms only, as shown here:

$$\begin{cases} \epsilon_2 = \frac{1}{\mathrm{E}} \frac{AE_0C\left(E-E_g\right)^2}{(E^2-E_0^2)^2+C^2E^2} \;\; for \;\; E > E_g \\ \epsilon_2 = 0 \;\; for \;\; E < E_g \end{cases} \quad (4)$$

The real part ϵ_1 of the dielectric function is derived from the expression of ϵ_2 using the Kramers-Kronig integration. We usually start by fitting the imaginary part of the dielectric function, described by the following parameters:

A (in eV) is related to the strength of the absorption peak,

C (in eV) is the broadening term of the absorption peak,

E_g (in eV) is the optical band gap energy,

E_0 (in eV) is the energy of the maximum transition probability and is always higher than the band gap energy E_g.

Then, we fit one parameter related to the real part of the dielectric function at high frequency ϵ^∞, representing the contribution of inter-band transitions occurring at high energies. This parameter also prevents the dielectric constant ϵ_1 from converging to zero for energies below the band gap. One of the limitations of the Tauc-Lorentz model is that it requires ϵ_2 to be zero for energies less than the band gap, not considering the intra-band absorption caused by defects.

We usually start with a Cauchy fit in the transparent energy range of SiN_x films to determine their thickness. Then, we fit the Tauc-Lorentz model to minimize the number of unknown parameters at each fit.

3.3. Characterization of the optical properties of silicon nitride monolayers

3.3.1. Set of monolayer samples

During this study, we deposited SiN_x-based films on 2-inch Si <100> substrates.

For the thin films deposited with the capacitively coupled plasma (CCP) reactor, we used a mixture of SiH_4, Ar, NH_3, and N_2 as gas precursors, and we kept the flow rates constant at 20, 400, 50, and 250 sccm, respectively, at a deposition pressure of 1500 mTorr. The substrate temperature was set to 280 °C for all samples, and the RF power was varied from 20 to 170 W. The deposition rates ranged from around 50 to 90 $nm.min^{-1}$.

In the ECR reactor, SiH_4, Ar, and N_2 were used as gas precursors and the flow rates were kept constant at 1.2, 13.6, and 1.2 sccm, respectively. The deposition pressure was 1.7 mTorr. The substrate heater temperature was set to 350 °C, which corresponds to 120 °C at the sample surface due to the temperature gradient in the thick metal substrate holder. The microwave power (MW) power coupled to the plasma was adjusted from 400 to 600 W. The deposition rates varied from around 1 to about 1.8 $nm.min^{-1}$, as shown in Table 2.

Table 2: Films deposition parameters. The variable parameter investigated is the MW deposition power highlighted in gray.

ECR Films	SiH_4 (sccm)	N_2 (sccm)	Ar (sccm)	Deposition Pressure (mTorr)	Deposition Rate ($nm.min^{-1}$)	Microwave Power (W)
Set 1	1.2	1.2	13.6	1.7	1.1	400
	1.2	1.2	13.6	1.7	1.5	500
	1.2	1.2	13.6	1.7	1.8	600

Then, optimization was carried out to increase the deposition rates in the ECR reactor before studying SiO_yN_x films. Three sets of samples were fabricated. The experimental details are summarized in Table 3.

Firstly, we deposited SiN_x films using SiH_4, Ar, and N_2 only. The flow rates of SiH_4 and N_2 were kept constant at 2.4 sccm, and the Ar flow was adjusted from 27.2 to 57.2 sccm. The deposition rates were between 2.7 and 3.2 $nm.min^{-1}$, and the total pressure during the deposition changed from 3.3 to 5.9 mTorr.

Secondly, we deposited SiO_yN_x films using SiH_4, O_2, N_2, and Ar. The flow rates of SiH_4 and N_2 were kept constant at 2.4 sccm, while the Ar and O_2 flows were adjusted from 57.2 to 54.2 sccm and from 0 up to 3 sccm, respectively. The deposition pressure was stabilized at 6.2 mTorr. The introduction of O_2 increased the deposition rates from 2.7 to 5.9 $nm.min^{-1}$.

Finally, we deposited SiN_x films using SiH_4, Ar, and N_2 with a constant flow rate of 2.4 sccm for SiH_4, while the Ar and N_2 flows were adjusted from 29.0 to 27.2 sccm and from 0.6 to 2.4 sccm, respectively, to maintain a constant deposition pressure of 3.3 mTorr. The deposition rates were around 3.1 $nm.min^{-1}$.

Table 3: Films terminology and deposition parameters. The parameters investigated are the N_2 and O_2 flows, and the deposition pressure highlighted in gray in the table.

ECR Films		SiH_4 (sccm)	N_2 (sccm)	O_2 (sccm)	Ar (sccm)	Dep. Pressure (mTorr)	Dep. Rate ($nm.min^{-1}$)	Film Thickness (+/-5 nm)
Set 2	SiN1	2.4	2.4	0.0	27.2	3.3	3.2	579
	SiN2	2.4	2.4	0.0	42.2	4.6	3.0	543
	SiN3	2.4	2.4	0.0	57.2	5.9	2.7	493
Set 3	SiON1	2.4	2.4	1.5	55.7	6.2	4.8	384
	SiON2	2.4	2.4	3.0	54.2	6.2	5.9	470
Set 4	SiN4	2.4	0.6	0.0	29.0	3.3	3.4	617
	SiN5	2.4	0.8	0.0	28.8	3.3	3.1	552
	SiN6	2.4	1.6	0.0	28.0	3.2	2.9	523

For all depositions, the MW power coupled to the plasma was fixed at 600 W to maintain a deposition rate higher than 3 $nm.min^{-1}$, and the sample was heated to 120 °C. The final properties of the thin films are a function of several parameters, so

sometimes, it is necessary to modify several deposition parameters to modify a single final property of the thin film.

3.3.2. Results and discussion

The absorption coefficient and refractive index of the deposited thin films presented in this Chapter were measured using a J.A. Woollam M-2000U ultraviolet-visible VASE. All the measurements were performed at incident angles of 55°, 60°, 65°, 70°, and 75° to improve the accuracy of layer modeling. We evaluated the refractive index and the absorption coefficient of the amorphous thin films as a function of the photon energy using the Tauc–Lorentz model [65]. We also used the Tauc plot method for determining the optical band gap of amorphous semiconductors [65] using optical absorbance data plotted as $(\alpha h\nu)^{1/2}$ with respect to photon energy to obtain a reasonable quantification of the optical band gaps of our films.

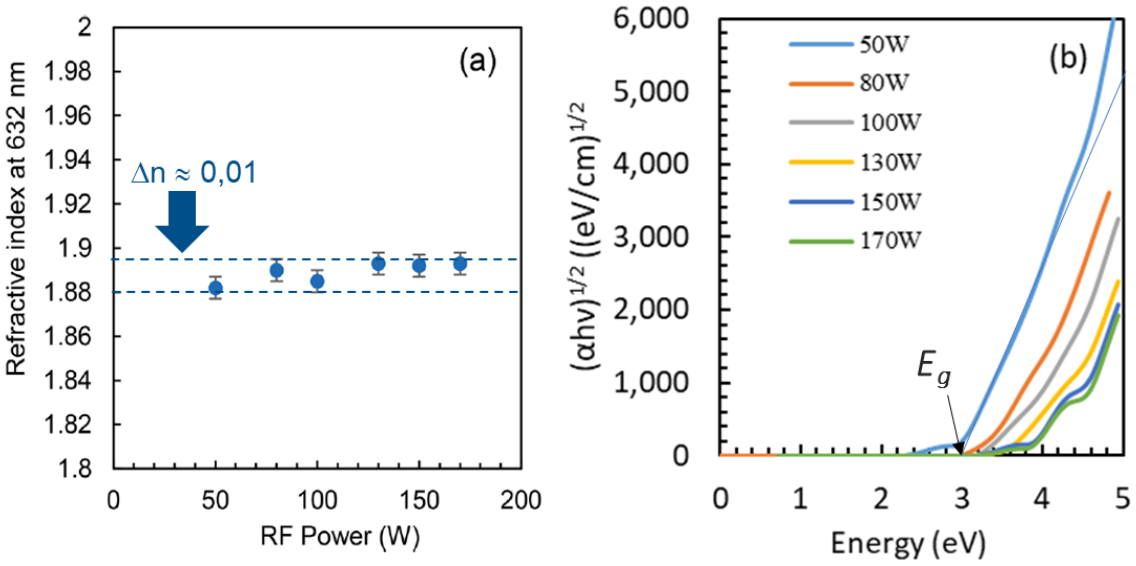

Figure 11: Refractive index at 632 nm (a) and Tauc plots derived from the optical absorption measurements (b) of the 500 nm SiN_x films deposited within the CCP reactor. [33]

In the CCP reactor, we mainly studied the impact of the deposition power on the optical properties of hydrogenated a-SiN_x films. Figure 11a shows only a slight increase in the refractive index at 632 nm ($1.88<n<1.89$) as a function of the deposition power. The optical bandgaps of the films were extracted from the Tauc plots shown in Figure 11b, and we notice that the optical band gap increases significantly from 3 eV to 4 eV with increasing deposition power.

We assume the porosity of the amorphous films to remain constant since the refractive index does not change significantly - $\Delta n \sim 0.01$; however, the deposition power influences the defects concentration in the SiN_x films. As discussed in [46], the main defects in amorphous SiN_x films are the Si and N dangling bonds. Since we measured an increase in the optical band gap at high deposition power, we attribute this variation

to a decrease of deep states associated with dangling bonds and a decrease of hydrogen in the SiN_x structure.

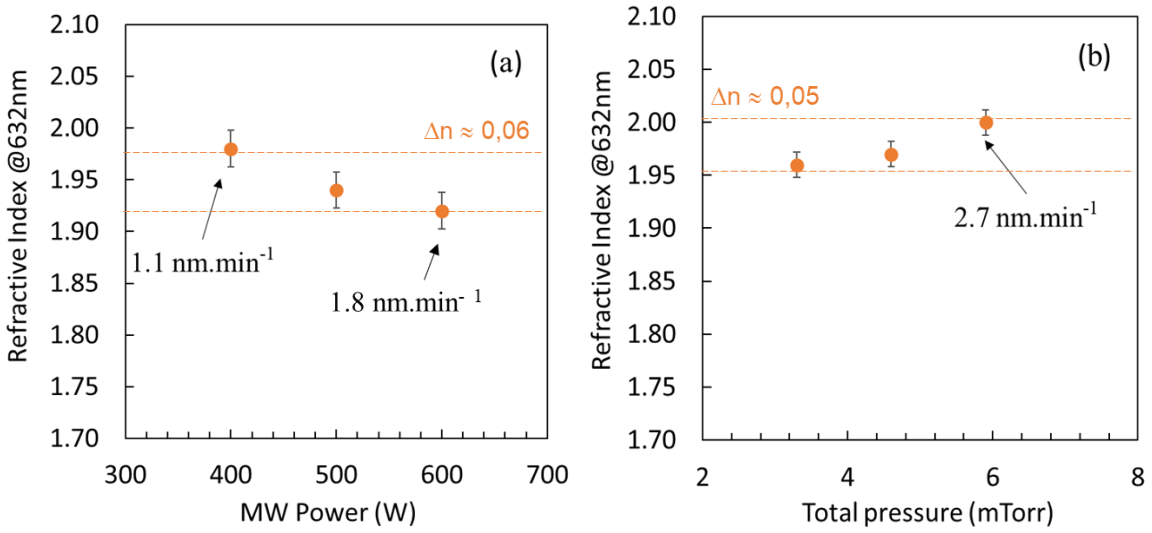

Figure 12: Refractive index at 632 nm of 500 nm SiN_x films deposited within the ECR reactor at three different deposition powers (a) and pressures (b). The samples (a) correspond to Set 1 from Table 2 and samples (b) correspond to Set 2 from Table 3.

In the ECR reactor, Figure 12a shows a significant decrease in the refractive index at 632 nm as a function of the deposition power. In contrast, Fig. 12b shows an increase in the refractive index as a function of the deposition pressure. The deposition rate of the SiN_x film with n=2 in Fig.12a is very low, around 1.1 nm.min^{-1}, requiring more than 7 hours to deposit a layer of 500 nm. Knowing that the layers deposited during this study are all around 500 nm, we had to modify the deposition parameters to achieve higher deposition rates and more reasonable deposition times of around 3 hours. We also note that the deposition rates and the film's properties are multi-parameter functions and might require the variation of two parameters to modify only

one property. Thus, we can double the deposition rate of a SiN_x film while keeping the same refractive index n=2.

After increasing the deposition rate of the ECR films, we studied the impact of the gas flows on the optical properties before and after an annealing at 400 °C. The refractive index and Tauc plots derived from the data obtained by VASE are shown for various deposition conditions.

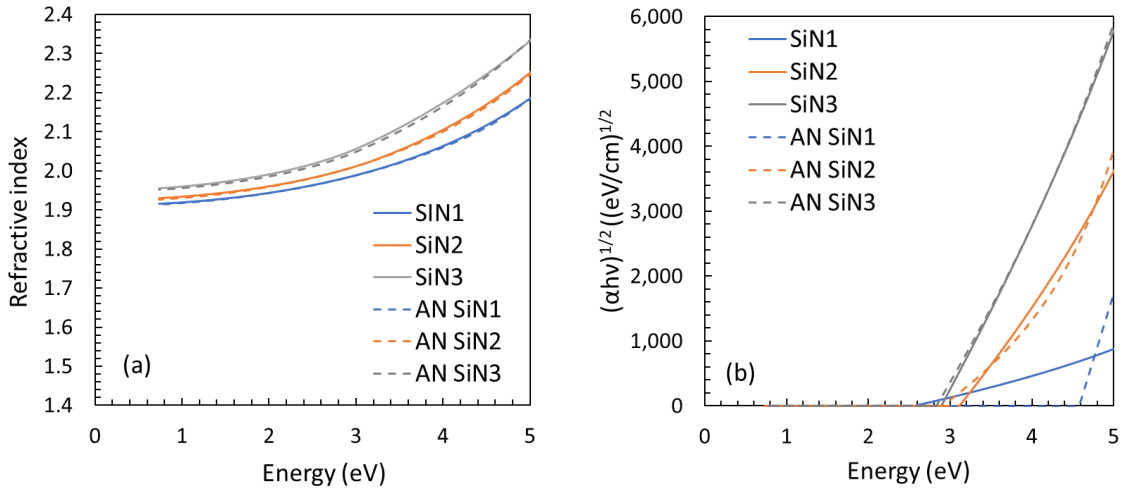

Figure 13: Refractive index (a) and Tauc plots (b) derived from the VASE measurements of SiN_x films deposited at three different pressures before and after annealing. "AN" indicates samples after annealing at 400 °C.

Figure 13a shows an increase of $\Delta n \sim 0.06$ in the refractive index with increasing deposition pressure for all photon energies, while Fig. 13b shows no absorption at low energies and an optical bandgap around 3 eV. The optical band gap extracted from the Tauc plots was not significantly affected by the deposition pressure. However,

above the optical band gap the absorption efficiency is increased with the deposition pressure. Even after annealing at 400 °C, the refractive index remained the same and the absorption curve of one sample SiN1 was modified, inducing a shift of the optical bandgap towards higher values (4.6 eV).

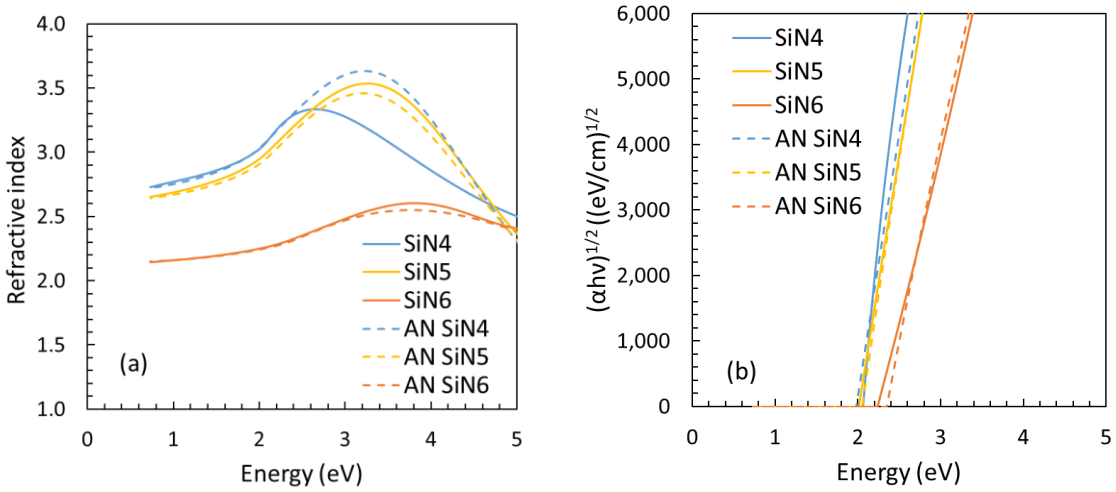

Figure 14: Refractive index (a) and Tauc plots (b) derived from the VASE measurements of SiN_x films deposited with different N_2 flows before and after a 400 °C annealing. "AN" indicates samples after annealing at 400 °C.

Figure 14a shows a decrease of $\Delta n \sim 0.6$ in the refractive index for low photon energies as a function of the N_2 flow during the deposition, while Fig. 14b shows that the optical bandgap increased with increasing N_2 flow. We assume that the optical bandgap of these films will increase progressively toward the SiN1 optical bandgap at 3 eV, shown in Fig. 13b, when the flow ratio N_2/SiH_4 reaches unity.

In Fig. 14a, we see a broad maximum in the refractive index for energies around and above the optical bandgap. The same peak could have been observed in the other SiN_x samples if we had performed VASE measurements at higher energies. In Ref [66], Forouhi and Bloomer measured the optical properties of amorphous SiN_x films produced by pyrolytic decomposition of a mixture of silane and ammonia up to 11 eV and observed a peak in the refractive index at around 7 eV. Despite the different fabrication processes, we believe our samples have a similar dispersion shape in terms of refractive index because of their amorphous nature.

We can consider that the range of photon energies for visible light from red to violet is 1.6 to 3.3 eV. So, these films are highly absorbing for applications in the visible range though they can be suitable materials for infrared applications only. After annealing at 400 °C, we noticed that the refractive index for low photon energies did not change much compared to before annealing.

It is common in optoelectronics to use both high refractive index and low refractive index layers to control light. For this reason, we studied the effect of oxygen on reducing the refractive index of SiN_x films.

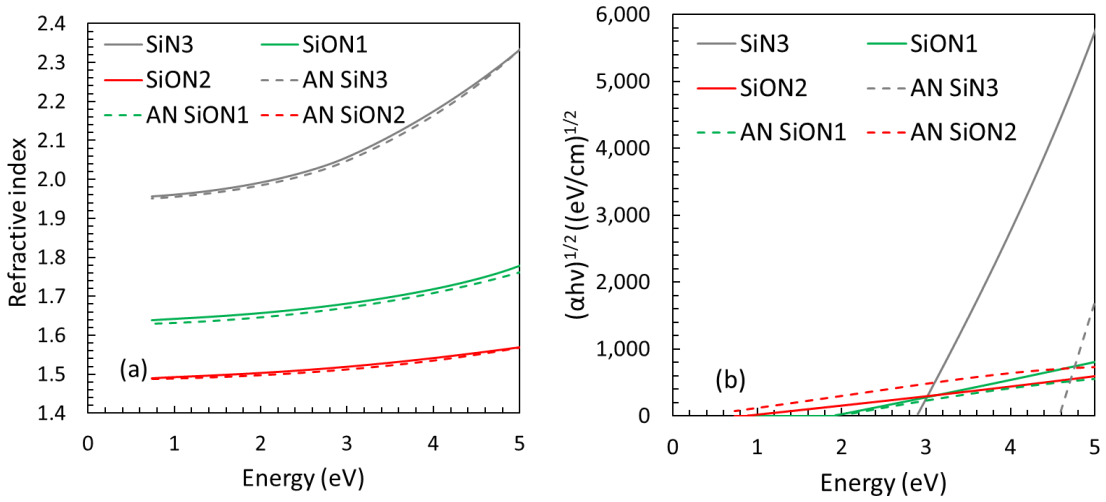

Figure 15: Refractive index (a) and Tauc plots (b) derived from the VASE measurements of SiO_yN_x films deposited with different O_2 flows before and after a 400 °C annealing. "AN" indicates samples after annealing at 400 °C.

Figure 15a shows a decrease of $\Delta n \sim 0.46$ in the refractive index for all photon energies as a function of O_2 flow in the gas mixture during the deposition, while Fig. 15b shows that the absorption levels of the films become significantly lower after the introduction of O_2 in the deposition mixture. After annealing at 400 °C, the refractive index did not change significantly.

Thus, modifications of the film's stoichiometry introduce a more significant variation of the film's refractive index in the order of 10^{-1}, while the deposition power and pressure induce Δn in the order of 10^{-2}. In the next part, we will see how to use these thin films to design an optical device based on a multilayer structure.

3.4. Characterization of the optical properties of silicon nitride based multilayer structures

3.4.1. Presentation and interests of multilayer systems

Multilayer optical coatings are important in several applications. We find them in optical devices such as notch filters, antireflection (AR) coatings, high-reflection (HR) coatings, and beam splitters. They are used to modify the optical properties of the near-surface region of photonic structures. The optical function of the structure depends on the refractive index and the thickness of each layer. It is common to find multilayer filters with hundreds of individual layers since the number of layers significantly influences the performance of such optical devices. This study mainly focuses on the fabrication and characterization of SiN_x-based multilayer structures. We discussed earlier how to control the optical properties of individual layers by modifying the deposition parameters. Here we show how to alternate during deposition between several layers of different thicknesses and refractive indices. The quality of fabrication of these individual layers impacts the overall system performance. In addition, we also approach the characterization of these multilayers with VASE. We explain the characterization strategy used to measure ex-situ the thickness profile of the different layers of the structure. To reduce the complexity, we only alternate between two types of layers with two different refractive indices, which is the case in many optical applications. The VASE measurements were efficient to determine both film thickness and

refractive index from monolayers. However, multilayer structures have significantly more unknown parameters, which is one of the reasons for measuring ellipsometry data over a wide spectral range and at multiple angles of incidence, 55°, 60°, 65°, 70°, and 75° is to improve the accuracy of the multilayer modeling.

3.4.2. Set of multilayer samples

SiN_x-based multilayer structures are a potential candidate for fabricating wavelength-selective reflective coatings in building-integrated photovoltaics (BIPV) technologies [67]. Since the lifecycle of BIPV cells is very long, and the coating surfaces are substantial, it is essential to produce films with well-controlled optical and mechanical properties. In this Chapter, we only focus on the control and characterization of the optical properties and later in this thesis, the mechanical properties of these layers will be discussed. Since we can control the optical properties of individual layers by modifying the deposition parameters of our PECVD system, we have chosen to fabricate functionalized multilayer structures to reflect light at 400 nm while transmitting most wavelengths with low loss of intensity. We used the ECR reactor because it allows better control of the thickness of thin layers below 10 nm, thanks to its relatively low deposition rates compared to the CCP reactor. For that reason, we developed specific recipes for the ECR reactor to obtain a high refractive index layer (n=2) and a low refractive index layer (n=1.5) while maintaining the stability of the plasma throughout the deposition. The ability to switch rapidly between the different layers

during deposition is essential to avoid the creation of intermediate layers at the interface and alter the overall performance of multilayer devices. Therefore, we tried to reduce the number of variable parameters that must be changed during multilayer deposition while maintaining the plasma stability during the whole process.

Here we show the recipes we used to alternate during deposition between SiN_x and SiO_yN_x films with similar deposition conditions except for the oxygen flow, as shown in Table 4.

Table 4: Films terminology and deposition parameters of SiN_x and SiO_yN_x films used in the fabrication of multilayer structures.

Films	SiH_4 (sccm)	N_2 (sccm)	O_2 (sccm)	Ar (sccm)	Deposition Pressure (mTorr)	Deposition Rate ($nm.min^{-1}$)
SiN	2.4	2.4	0.0	57.2	5.9	2.7
SiON	2.4	2.4	3.0	54.2	6.2	5.9

Table 4 also shows that the addition of oxygen almost doubles the deposition rates of SiO_yN_x films compared to SiN_x films.

First, we configured our system to stabilize the ECR plasma and deposit the multilayers automatically. We started by depositing multilayer structures with 2, 4, and 6 layers of 100 nm each. We then used these samples to implement an ellipsometry model for estimating thickness profiles in multilayer structures. Then, we fabricated two notch filters with a minimum number of layers designed to reflect light within a

specific wavelength λ_0 while transmitting most wavelengths with low intensity loss. We selected two designs with 11-layers: the first one with a quarter-wave physical thickness, $\lambda_0/4n$, to the reference wavelength $\lambda_0 = 400$ nm. The other design with an optimized physical thickness was developed by Paramita Bhattacharyya [68] as an optimized notch filter with a minimum number of layers on a silicon substrate to be integrated as aesthetic reflectors into flexible solar cells to reflect colors over the entire visible spectrum on demand. The thickness profile optimization was performed using a gradual evolution optimization technique on OptiLayer software [69] using a starting design to obtain an optimized notch filter with reduced ripples maximizing transmission while maintaining a narrow reflection peak in the desired wavelength (400 nm). Since these optical notch filters must maintain their optical and mechanical integrity during long-term repeated use on a flexible substrate. We decided to use our knowledge of SiN_x-based monolayers developed during this PhD in a collaboration framework to fabricate and characterize these specific optical devices. Their mechanical properties will be shown in Chapter 4.

3.4.3. Multilayer analysis and extraction of thickness profiles

We started our analysis by assuming that our layers have the same optical properties at all levels of the multilayer structure and that the deposition rate is constant for each given material. We have used the optical constants (n,k) of each material from reference monolayers and kept them constant during the fit, where we fitted only the film thicknesses.

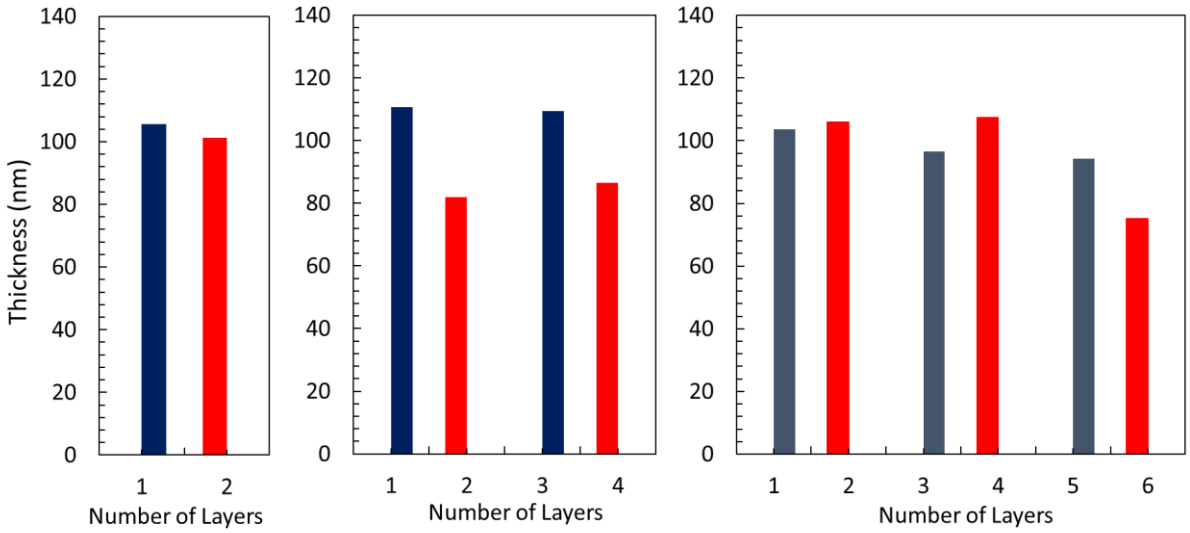

Figure 16: Three multilayer structures with 2, 4, and 6 layers of 100 nm each deposited on a Si substrate. The odd layers in blue are SiN_x layers, and the even layers in red are SiO_yN_x layers. The thickness values are estimations made by fitting ellipsometry data.

We defined the number of initial layers and their targeted thickness beforehand. Figure 16 shows the fitted thickness estimated from ellipsometry data for the 2-, 4-, and 6-layer structures. We noticed the SiO_yN_x thicknesses were 20 % below the target thickness in the 4-layer sample and near or slightly above the target thickness in the 6-layer sample. However, the fitted thicknesses of SiN_x were above the target thickness in the 4-layer sample and gradually decreased below the target thickness for the last layers deposited in the 6-layer sample. We assume that this variation between the targeted and measured results may be due to a slight change in the deposition rate or the films' optical properties during the multilayer deposition since these parameters were obtained from reference layers of approximately 500 nm. Our model does not consider other phenomena, such as the interaction at the interface between the films, which can induce biases in our results. However, we do not wish to increase the complexity of our model and accept uncertainties up to 20 % for layers with a thickness of 100 nm. If our uncertainty comes from the interface between the layers, we expect the thickness error to increase significantly for thinner layers.

This approach becomes more challenging with structures containing significantly more layers. In this study, we fabricated an 11-layer notch filter structure with quarter-wave thickness using automatic ECR deposition, where we switch between SiN_x layers and SiO_yN_x layers by controlling the oxygen flow only, as shown in Table 4. The same strategy was followed to fit the VASE data, where we define an initial thickness profile structure before starting the fit which makes it possible to converge rapidly.

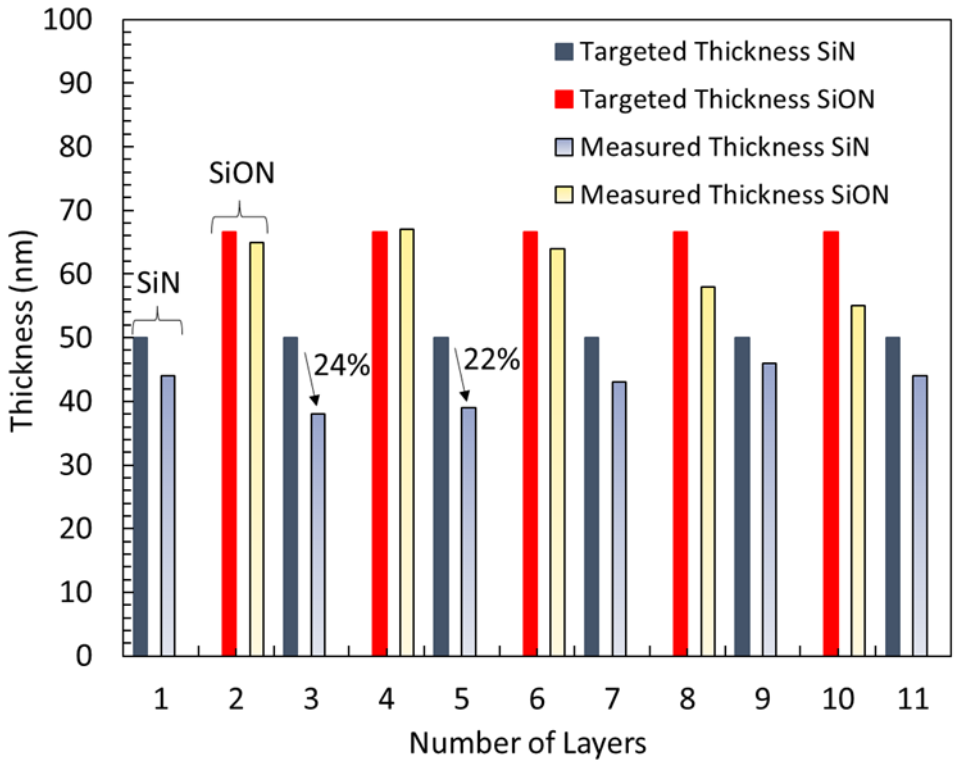

Figure 17: 11-layer notch filter structure with a quarter-wave thickness. The odd layers are SiN_x layers, and the even layers are SiO_yN_x layers. The targeted thickness values are in solid colors and the fitted thicknesses from the ellipsometry data are in grading colors.

Figure 17 shows the targeted thickness values from the design and the fitted thickness from the ellipsometry data of each layer of the 11-layer notch filter structure. The reproduction of the design is generally satisfactory; however, we detected significant deviations of more than 20 % below the target thickness in some layers (such as layer 3 and 5 in Fig. 17).

A simulated reflectance spectrum was obtained from a Python script using a transfer matrix method on the 11-layer structure. The experimental reflectance spectra were measured at -12°, -6°,6°, and 12°.

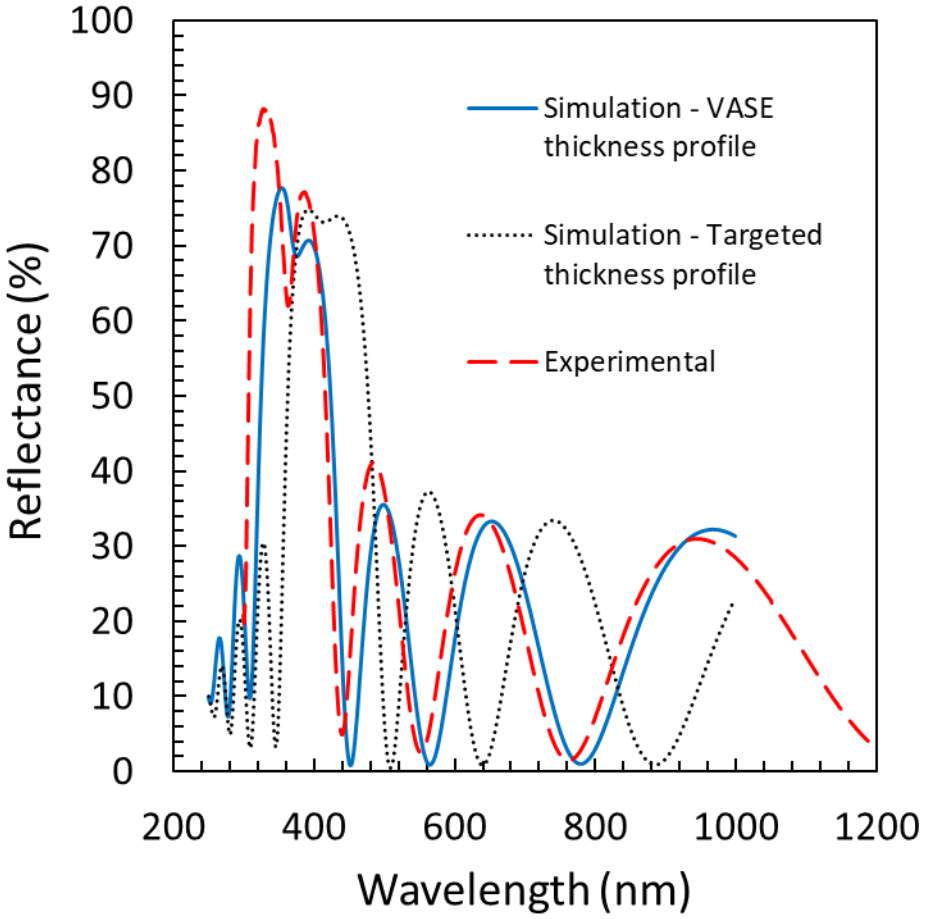

Figure 18: Reflectance spectrum of the 11-layer notch filter structure with a quarter-wave thickness. The simulated reflectance from a measured thickness profile is shown in a blue solid line, and the experimental reflectance spectrum is in a red dashed line, while the targeted simulation is in dotted line. Angle of detection at 6°.

Figure 18 shows experimental and simulated reflectance curves measured and calculated at 6°, respectively, since it was the closest angle to the incident angle measurable experimentally with our reflectance spectrophotometer. We obtained a notch filter with 70 % reflection around 400 nm using the targeted thickness. Because of the limited number of layers, we have ripples at other wavelengths with around 30 % reflection. The experimental reflectance curve was quite close to the targeted simulation but had a blue shift of 55 nm. The simulated reflectance spectrum calculated using the measured thickness profile from the VASE model was closer to the experimental reflectance results.

We usually use notch filters with hundreds of layers to reduce the ripples in a quarter-wave thickness structure. However, in our work, we have used the optimized notch filter design, suggested by Bhattacharyya et al. [68] with reduced ripples since it uses a minimum number of layers on a silicon substrate. We used the ECR reactor to reproduce the optimized structure's thickness profile automatically and the VASE to estimate the thickness profile of the fabricated structure.

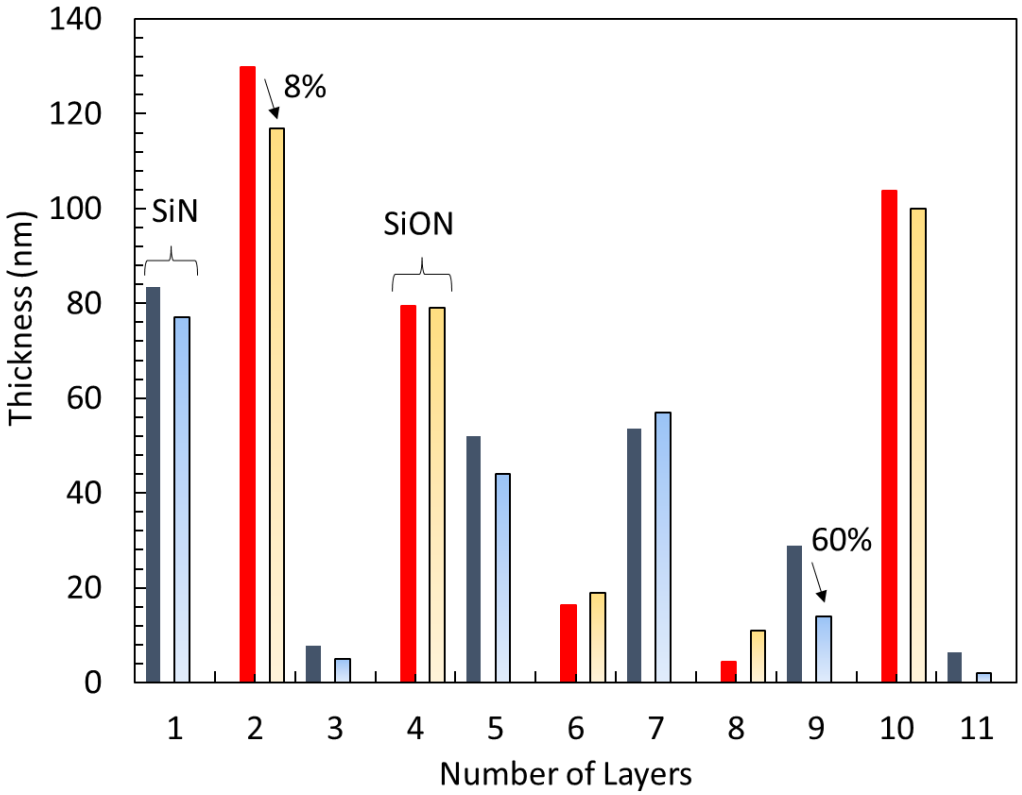

Figure 19: 11-layer notch filter structure with an optimized thickness profile. The odd layers are SiN_x layers, and the even layers are SiO_yN_x layers. The targeted thickness values are in solid colors, and the fitted thicknesses from the ellipsometry data are in grading colors.

Figure 19 shows the thickness profile of an optimized 11-layer notch filter, and we noticed that the fit is satisfactory except for layers with less than 30 nm thickness, where the errors were very high. For example, the estimated thickness of layer 9 was 60 % below the target thickness. We measured and calculated the experimental and simulated reflectance curves at 6°, respectively.

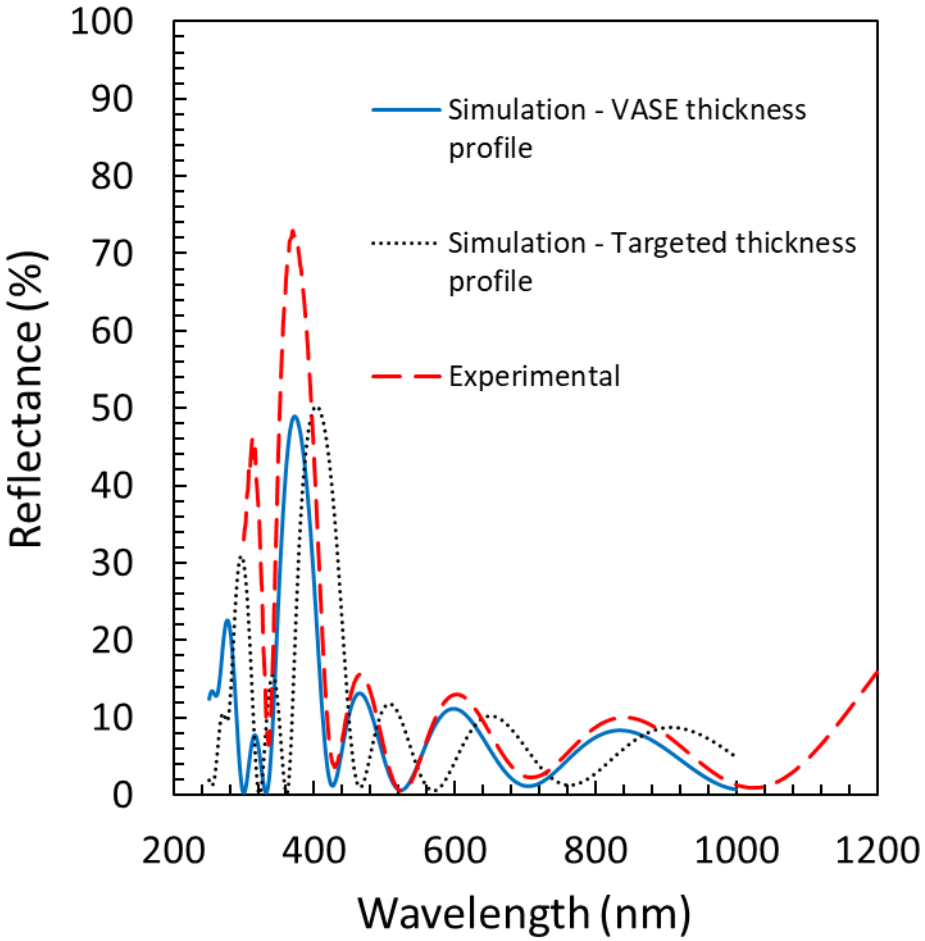

Figure 20: Reflectance spectrum of the 11-layer notch filter structure with an optimized thickness profile. The simulated reflectance from a measured thickness profile is shown in a blue solid line, and the experimental reflectance spectrum is in a red dashed line, while the targeted simulation is in dotted line. Angle of detection at 6°.

Figure 20 shows a significant reduction in the reflection peak width and ripples compared to the non-optimized structure in Figure 18. We noticed a maximum reflectance of 70 % in the experimental spectrum, higher than the expected values from simulation of around 50 %, and less than 15 % reflection in the transmission region. The simulated

reflectance spectrum using the measured thickness profile and the experimental reflectance both have a blue shift of about 28 nm from the targeted spectrum. In order to check if this blue shift is due to the error of the measurement angle of +/- 1°, we also studied, using simulation, the influence of the detection angle on the notch reflection wavelength.

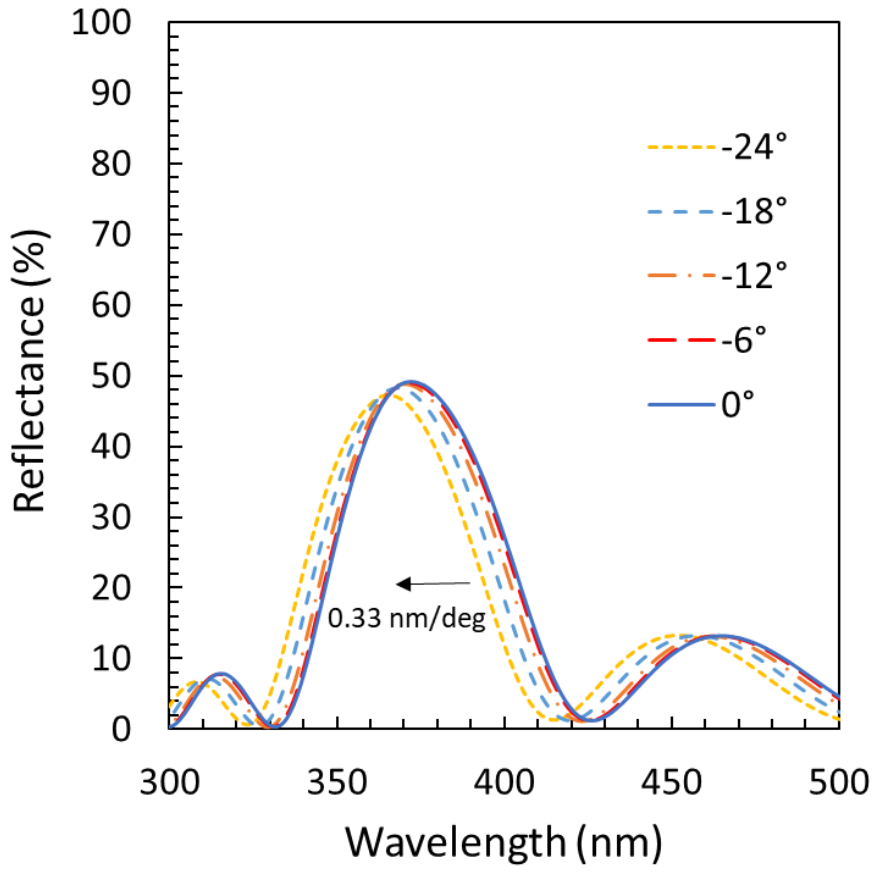

Figure 21: Reflectance spectrum shift vs. the angle of detection. The simulated reflectance spectrum of the 11-layer notch filter structure from a measured thickness profile using VASE.

Figure 21 shows a blue shift for different angles from the incident angle. However, the shift is small at around 0.33 nm per degree. We also note that the simulation is symmetrical and the negative detection angles have the same optical spectrum as their absolute values. Hence, the difference between the experimental peak and those resulting from the simulation in Figures 20 and 18 is not due to measurement angle errors but to modification in the structure itself compared to it is simulated design.

3.5. Conclusions

In this Chapter, we described how we control the refractive index of SiN_x-based films by tuning select PECVD process parameters. We optimized the deposition rate and stoichiometry of our ECR films to fabricate functional multilayer structures. We also presented satisfactory results of an ex-situ characterization method using VASE to estimate the thickness profile of the structures. Then, we have performed an experimental reflectance spectral detection and compared the results with multilayer simulation using a transfer matrix method. All these results do not consider the possible geometric deformations of the films under stress or any phenomenon that can occur at the interface between the layers in complex structures. Thus, we explore in the next part the mechanical properties of the films.

4. Study of Mechanical Properties of Silicon Nitride Based Thin Films

4.1. Introduction

This Chapter outlines the mechanical properties of SiN_x-based thin films and the different methods used to characterize these properties.

First, we describe the wafer curvature method used to measure the residual stress of the films. We give an overview of the principle of nanoindentation since it was the primary characterization tool used to determine the hardness and the elastic modulus of our films. We also used some micro-structures made from films with different compressive residual stresses to estimate the elastic properties of these films from their deformation shapes. Then, we studied experimentally the impact of process parameters on the mechanical properties of our SiN_x-based films and suggested some mechanisms of stress generation. This is followed by a section presenting the mechanical properties of the multilayer structures described in Chapter 3.

4.2. Experimental details

4.2.1. Set of samples

Several amorphous SiN_x-based thin films were deposited using two different deposition methods, as discussed in Chapter 3. We used the samples described in Tables 2 and 3 to study the mechanical properties of the stressor layers. In addition, we deposited some samples using the same recipes with greater thickness of around 2 microns in order to measure their elastic properties using nanoindentation.

4.2.2. Curvature method

We used a well-established residual stress characterization technique based on wafer curvature measurements and the Stoney model [70]. This method of characterization is most often used to quantify the mechanical stresses in thin films and identify their tensile or compressive nature. We used in this work two types of instruments to measure the curvature profile of our samples. First, we used a Bruker DektakXT Stylus profilometer to measure the wafer curvature prior and after deposition of a layer. Then, we used a Python script developed during this PhD project to adjust the data using a best fit procedure assuming a circular shape to estimate the radius of curvature R necessary to calculate the stress using Stoney formula (Equation 5). However, since it is not possible to use contact profilometry to measure the curvature of heated samples, we started a collaboration with the Ecole Polytechnique Montreal, during which

I was trained to perform measurements with the Tencor FLX-2900 commonly named FLEXUS. In this case, the curvature measurements were performed optically using a 670 nm laser, and the residual stresses of the films were calculated automatically at different temperatures.

For both measurements techniques, the residual stress of the layer was deduced from measuring the curvature radius of a full wafer before (R_0) and after (R) thin film deposition on its surface, it is possible to evaluate the strain information and then deduce the thin film built-in stress using Stoney's formula [70]:

$$\sigma_f = \frac{E_s}{6(1-\vartheta_s)}\frac{t_s^2}{t_f}\left(\frac{1}{R}-\frac{1}{R_0}\right) \tag{5}$$

With E_s, ϑ_s, t_s: elastic modulus, Poisson ratio, and thickness of the substrate, respectively, and t_f the thickness of the film. R_0 and R are the measured curvature radii. Consequently, it is not necessary to know the elastic properties of the deposited thin films to determine their residual stress σ_f. However, this model has some practical constraints and limitations. The films must be homogeneous on the substrate and have a small thickness compared to that of the substrate, and the longitudinal dimensions of the system {thin film + substrate} must be significantly greater than their thickness. Thus, circular substrates are used to have a spherical deformation and a negligible variation in the radius of curvature along the different wafer diameters.

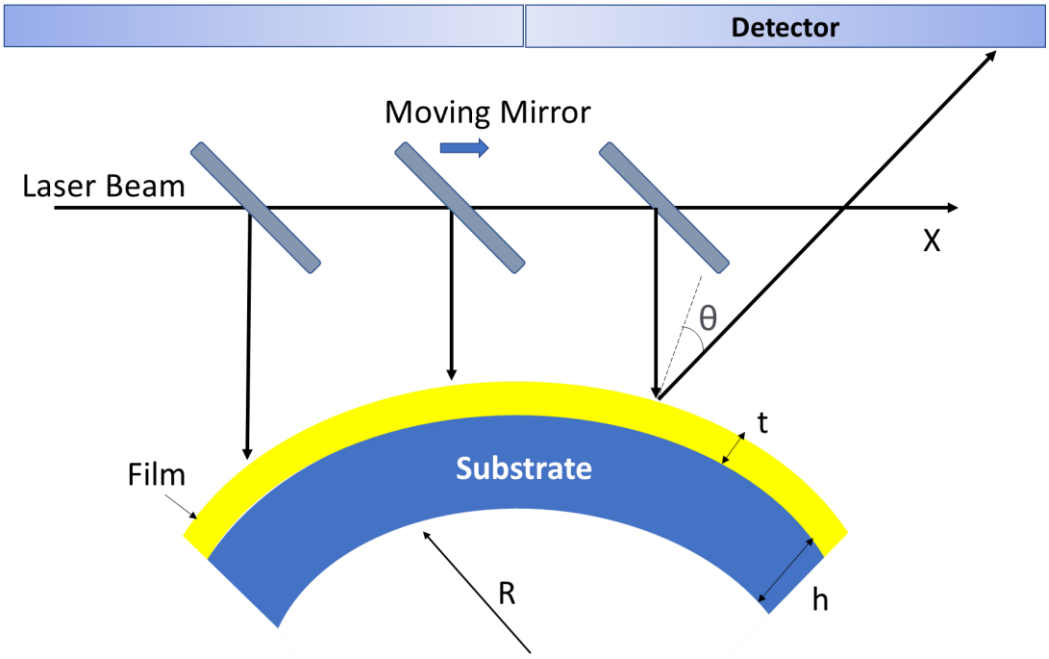

Figure 22: Principle of measuring the radius of curvature by reflectometry.

Figure 22 shows the principle of measuring the radius of curvature by reflectometry used in the FLEXUS. A translating mirror reflects a laser with a wavelength of 670 nm on the substrate. According to the angle of reflection estimated by the displacement of the reflection peak intensity on the photodiode, we can calculate the curvature radius of the substrate R.

The curvature $\frac{1}{R}$ is obtained by calculating the change of the reflected angle $\Delta\theta$ with a displacement ΔX of the mirror along the sample surface by the following equation:

$$\frac{1}{R} \cong \frac{\Delta\theta}{\Delta X} \tag{6}$$

We measured the radius of curvature of the wafers at room temperature but also at temperatures up to 400 °C at a rate of 10 °C.min^{-1} under an N_2 atmosphere to reduce the O_2 contamination of the films. Further in this Chapter, we will discuss the impact of thermal cycling on the residual stress of the films.

4.2.3. Principle of nanoindentation

Unlike conventional indentation, which focuses on a residual mark left by the indenter on the sample, instrumented nanoindentation studies the displacement curve as a function of the normal force P applied to the sample. It is possible to measure locally the elastic properties and the hardness of a material thanks to a method developed by Oliver and Pharr [71]. The visualization of the indent was no longer necessary, so nanoindentation was used in many applications to measure the mechanical properties of small volumes of material, such as thin films. Thus, we can observe both its plastic and elastic response from an indentation load-discharge curve.

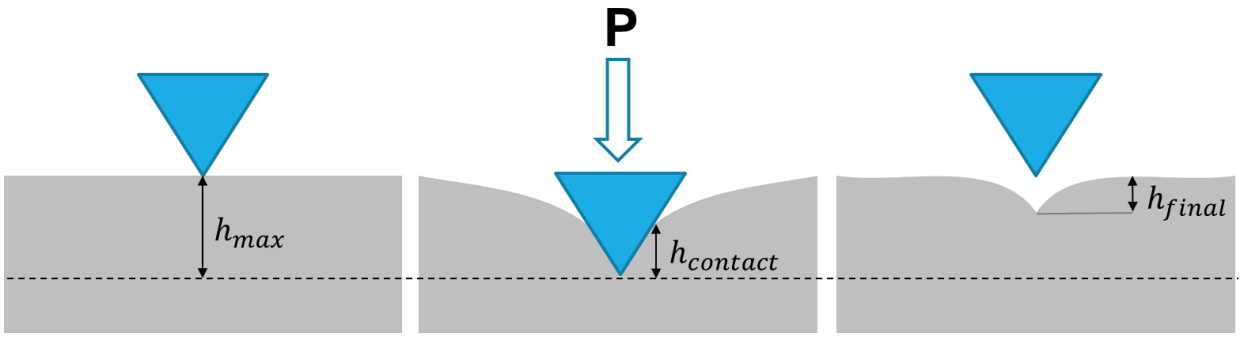

Figure 23: Indentation of a surface.

Figure 23 shows the principle of indentation where a tip enters with a force P (on the order of millinewtons) into a material, and the resulting indentation depth h is measured during the loading and unloading of the tip. When the force applied on the tip reaches a maximum, we note an indentation depth h_{max}. In thin films, the recommended penetration depth h_{max} is 10 % of the film's thickness to avoid substrate effects and obtain more accurate results. The final depth h_{final} at which the tip stops under zero force is the result of the residual plastic deformation of the material after indentation.

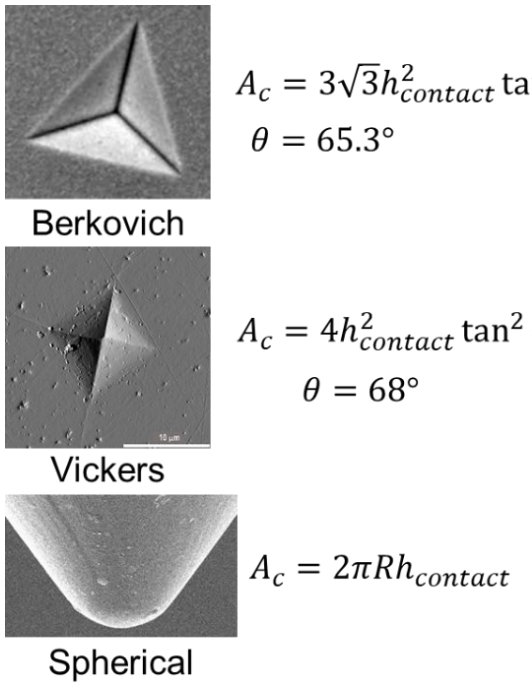

Figure 24: Examples from different geometries of indenter tips.[72]

The area of contact A_c between the indenter tip and the material depends on the geometry of the indenter tip and can be expressed with $h_{contact}$ as illustrated in Figure 24. Indenter tips are usually made of diamond and have different shapes depending on the application. It can be a three-sided pyramid (Berkovich), a four-sided pyramid (Vickers), or spherical, as shown in Figure 24. It is important to calibrate the nanoindenter often because a worn tip can become more rounded and behave like a sphere at shallow depths. Thus, the load-displacement curves are converted into an indentation stress-strain curve which induces an overestimation of the elastic modulus and inaccurate results.

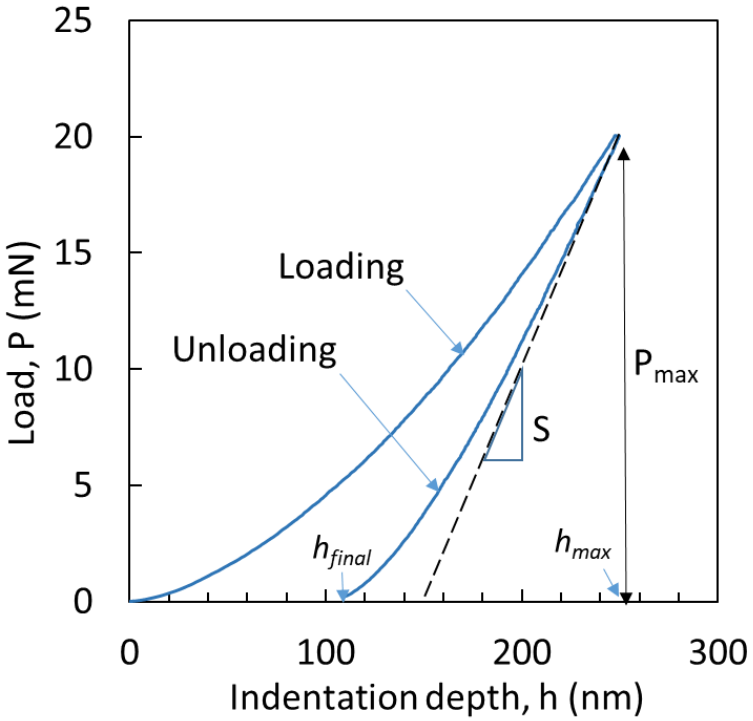

Figure 25: Single nanoindentation measurements.

The sharp, well-defined indenter tips have load-displacement curves with a loading part that combines both plastic and elastic deformation of the sample and an unloading part that reflects purely the elastic behaviour of the material. Therefore, the contact stiffness S of the sample is obtained from the slope of the unloading segment of the force-displacement curve P=f(h), illustrated in Figure 25. More details on the method of estimating S from the load-displacement curve are very well explained in the work of Oliver and Pharr [71].

The contact area remains very difficult to obtain because it does not concern the entire penetration depth but only the part of the indenter in contact with the sample (Figure

23). It is, therefore, necessary to determine the depth of penetration of the indenter in the sample noted $h_{contact}$. It is possible to relate S to $h_{contact}$ using the following formula:

$$h_{contact} = h_{max} - \varepsilon \frac{P_{max}}{S} \tag{7}$$

with $\varepsilon = 0.75$ for a Berkovich indentation tip.

Since the area of contact A_c is a function of $h_{contact}$, as shown in Fig. 24, it is possible to evaluate the indentation area A_c directly from the force-displacement curve and calculate the elastic modulus E_s and to the hardness H of the material under test, as follow:

$$H = \frac{P}{A_c(h_{contact})} \tag{8}$$

For the elastic modulus E_s, we first calculate the reduced elastic modulus E_r as follow:

$$E_r = \frac{\sqrt{\pi}}{2} \frac{S}{\sqrt{A_c(h_{contact})}} \tag{9}$$

Then, we note that E_r considers both the elastic deformations appearing in the sample and in the indenter. It is defined by the following formula:

$$\frac{1}{E_r} = \frac{1-\nu_s^2}{E_s} + \frac{1-\nu_i^2}{E_i} \tag{10}$$

For a diamond indenter, which is generally the case, $E_i = 1141$ GPa and $\nu_i = 0.07$. Generally, for soft materials E_s is very close to E_r.

In this study, we determined the elastic modulus and hardness of the films by nanoindentation measurements using a NanoTest Vantage instrument and an Anton Paar Ultra Nanoindentation Tester (UNHT³), both with a Berkovich indenter.

We also applied a progressive loading on the indenter from 2 mN to 20 mN to have a continuous load-depth curve (in the UNHT³).

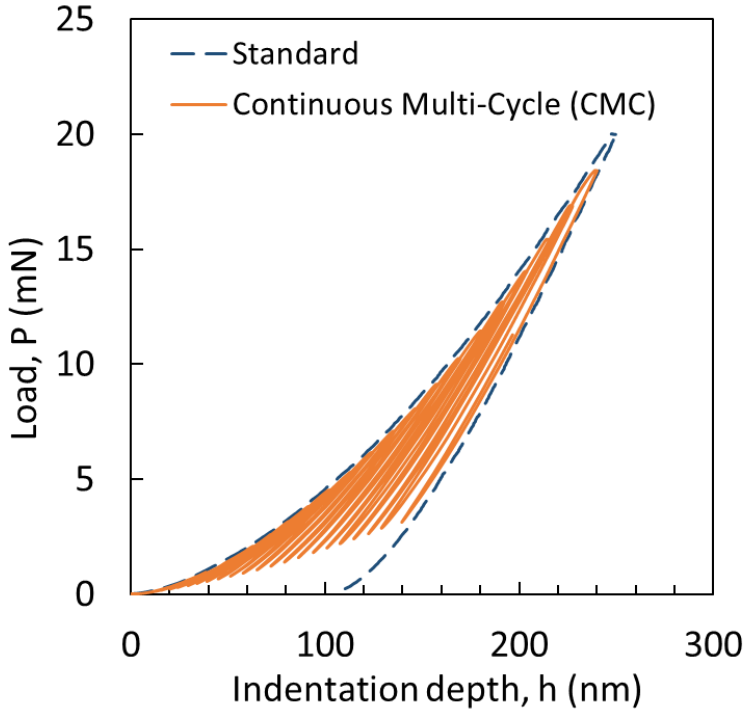

Figure 26: Single nanoindentation measurements with two different modes: standard and continuous multi-cycle mode.

Figure 26 shows the load-displacement curve for standard and continuous multi-cycle (CMC) modes. In the CMC mode, we start applying a minimum load value, then unloading 60 % of the force and immediately re-loading to a higher load until we reach the maximum penetration. At the same time, the standard method goes directly to the maximum indentation depth. Thus, the CMC test allows the evaluation of the hardness and elastic modulus of the films over the indentation depth.

4.2.4. Fabrication and characterization of microbeams

We deposited compressive thin films and measured their mechanical residual stress using curvature measurements. Then, we have fabricated doubly clamped microbeams to evaluate some of the elastic properties of these thin films. First, we defined narrow stripes before releasing them into cantilevers and microbeams. The procedure to define narrow stripes is based on optical lithography using a positive polymer resist as a mask, followed by mask opening and etching of the dielectric thin film using reactive ion etching with SF_6 plasma. After etching the dielectric thin film, the remaining polymer was removed using O_2 plasma. We released these narrow stripes from their substrate to fabricate the microstructures by wet etching using tetramethylammonium hydroxide (TMAH) (5 % solution at 85 °C) in the case of Si substrate. However, such microstructures could be also achieved on III-V substrates with other kind of chemical solutions. On Si substrates, TMAH is known to produce anisotropic etching sensitive

to crystallographic orientations of Si. Thus, the stripes were inclined by 45° in respect of the crystallographic orientations [110] and [1-10] of our (100) Si substrates.

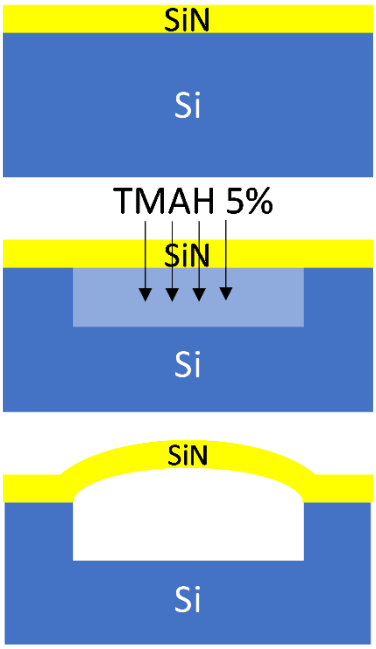

Figure 27: Cross-sectional schematic view of the process steps for fabricating a SiN_x microbeam on top of a Si substrate using SiN_x compressively strained films. [33]

Figure 27 shows a schematic of the process for fabricating a SiN_x microbeam. After etching the SiN_x thin film into a matrix of 10, 15, and 20 µm wide stripes, we release the SiN_x microbeams using the same process described in Figure 27.

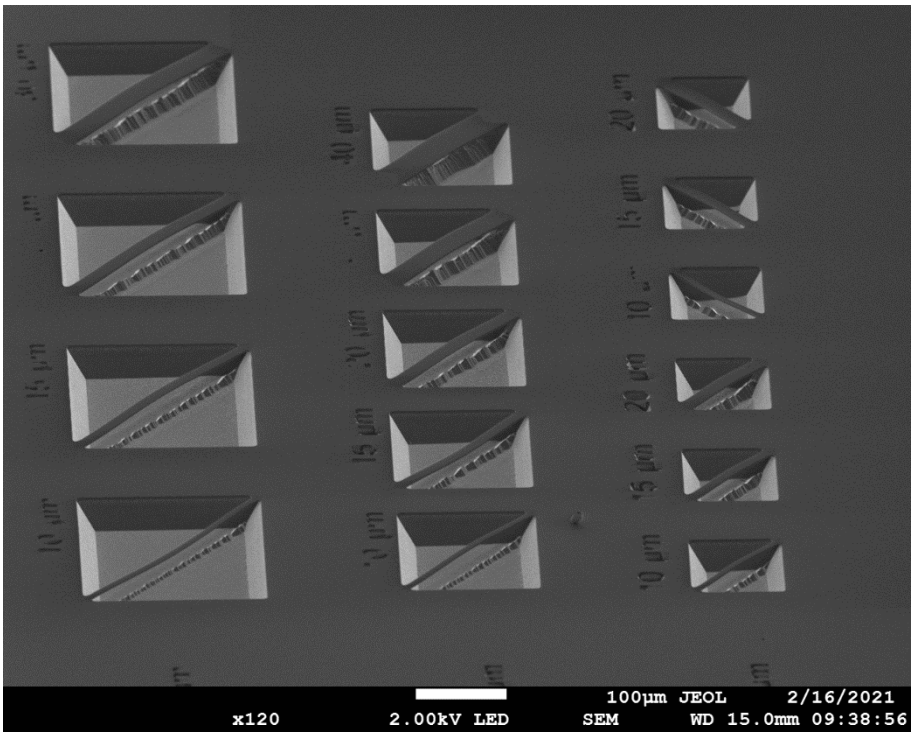

Figure 28: SEM image of a matrix of 10, 15, and 20 µm wide microbeams fabricated from a SiN_x film deposited on a Si substrate using a CCP reactor with 130 W RF power (compressive built-in stress: -300 MPa).

Figure 28 shows a scanning electron microscope (SEM) image of a matrix of microbeams obtained after etching and releasing a SiN_x film deposited on Si by CC-PECVD with initial compressive built-in stress of – 300 MPa.

We also measured the deformation of microbeams with a commercial Olympus confocal microscope with a blue laser diode to get as high accuracy as possible on the measurement of the vertical profiles of the released microbeams (± 50 nm). Then, a curve fitting of the data was performed to extract the elongation of the microbeams $\Delta L/L_0$, where L_0 is the initial length of the microbeam before the release. We assume

that the microbeam has a uniform compressive residual stress σ along its entire length and thickness before it is released from the substrate.

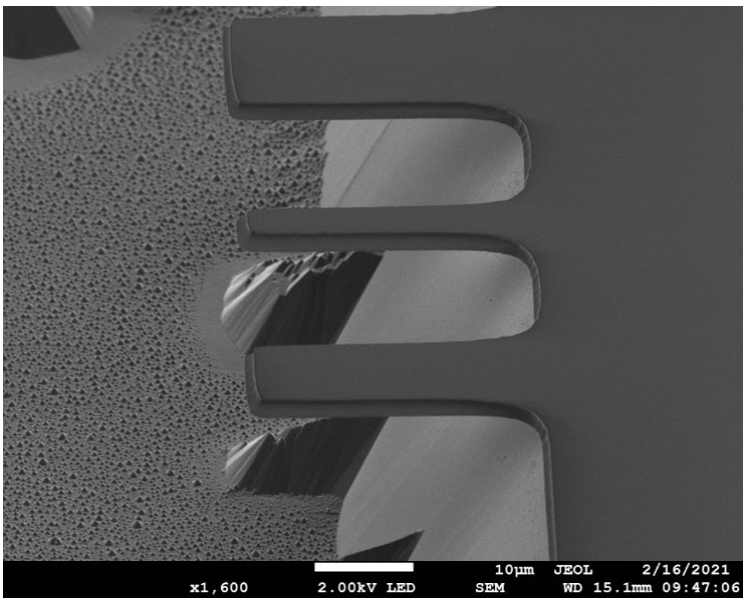

Figure 29: SEM image of cantilevers fabricated from a SiN_x film deposited on a Si substrate using a CCP reactor with 130 W RF power (compressive built-in stress: -300 MPa).

Figure 29 shows cantilevers fabricated from the same SiN_x films that remain flat after releasing them from the substrate, which confirms our assumption that σ is uniform along the thickness of the films. However, the variation in elongation in the cantilevers is too small to be measured accurately. The doubly clamped microbeams are much longer (hundreds of micrometers) and more suitable for elongation measurement.

Once released from the substrate, the microbeams tend to bend and deform in the perpendicular direction to the compression plane. We observe this buckling phenomenon when the residual stress is compressive and higher than the minimum stress value required to bend the microbeam, so called Euler's critical load σ_{Euler}.

The σ_{Euler} mainly depends on the structure geometry and the properties of the material, such as elastic modulus and Poisson's ratios. In our case, the σ_{Euler} necessary for the buckling of 500 nm thick and more than 100 µm long microbeams is less than 3 MPa (compressive), which is negligible compared to the residual stresses σ_{stoney} of the layers measured using curvature measurements.

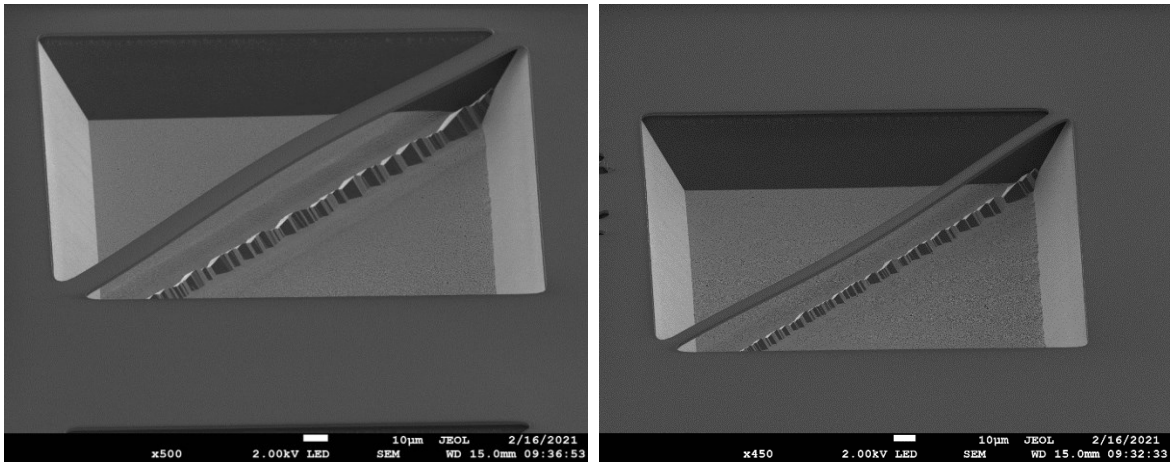

Figure 30: SEM image of microbeams buckling upward (left) and downward (right) fabricated from a SiN_x film deposited on Si by PECVD with 130 W RF power (compressive built-in stress: -300 MPa).

Figure 30 shows that microbeams fabricated in similar conditions can buckle either upward or downward. However, it is not easy in our case to control the direction of the buckling. Thus, we etched the substrate deep enough to allow the total elongation of the beams buckled downwards and to include them as well in our study.

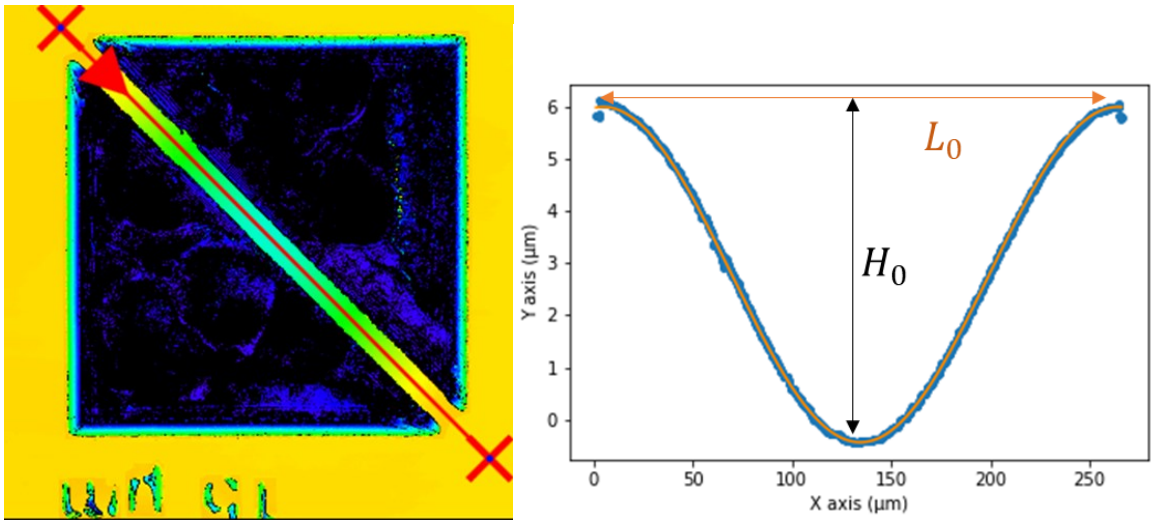

Figure 31: Confocal measurement of a 15 µm wide microbeam buckling downward (left) and the best fits of the experimental deformation profile using Equation 11 (right).

Figure 31 shows an example of a confocal measurement performed on a released microbeam and its deformation profile. To obtain the best fit of our results, it is necessary to neglect the influence of the shear stress and solve the differential equation of Euler-Bernoulli's beam. Thus, we obtain the following solution:

$$y(x) = -\frac{H_0}{2}\cos\left(\frac{2\pi}{L_0}x\right) + \frac{H_0}{2} \tag{11}$$

to fit the shape of the microbeams by varying the parameters H_0 and L_0 using a Python script developed during this PhD project. The Python script used these fitted data to precisely determine the elongation ΔL as:

$$\Delta L = L_1 - L_0 = \int_0^{L_0} \sqrt{1 + y'(x)^2}\,dx - L_0 \tag{12}$$

L_0 is the distance between the two embedments. As a result, the microbeam elongation is related to the elastic modulus and stress through Hooke's law. The same measurement can be automatically reproduced on several microbeams.

Then, it is possible to evaluate the elastic modulus E of SiN_x thin films using the elongation of the microbeams and the built-in residual (compressive) stress σ_{stoney} that was previously deduced from wafer curvature measurements by the following formula:

$$E \approx \sigma_{stoney}\left(\frac{1}{1-\nu}\frac{\Delta L}{L_0}\right)^{-1} \quad (13)$$

We took the value of Poisson's ratio from the literature (ν=0.23)[73].

4.3. Characterization of the mechanical properties of silicon nitride-based monolayers

4.3.1. Analysis of residual stresses

We evaluated the residual stress in the deposited thin films using the standard method of wafer curvature measurements discussed earlier in this Chapter. For this first set of samples, the curvature was measured before and after the deposition using a Bruker DektakXT Stylus profilometer available at INSA Rennes.

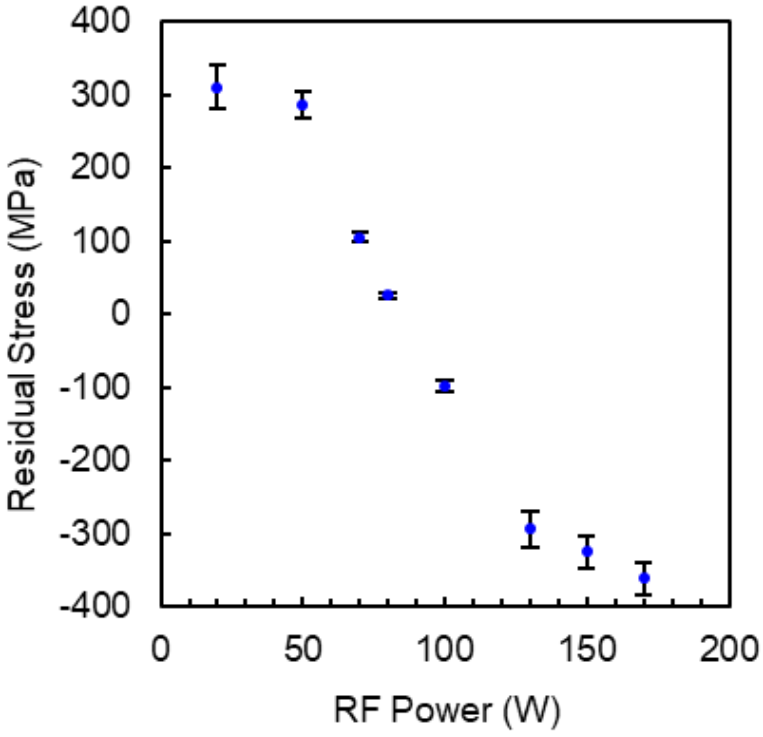

Figure 32: Residual stress vs. excitation power for 500 nm SiN_x films deposited within the CCP reactor. [33]

Figure 32 shows the influence of the RF power injected into the CCP reactor on the deposited films' residual stress. We notice a variation from tensile (+ 300 MPa) to compressive (– 400 MPa). The higher the deposition power, the more compressively strained the films are.

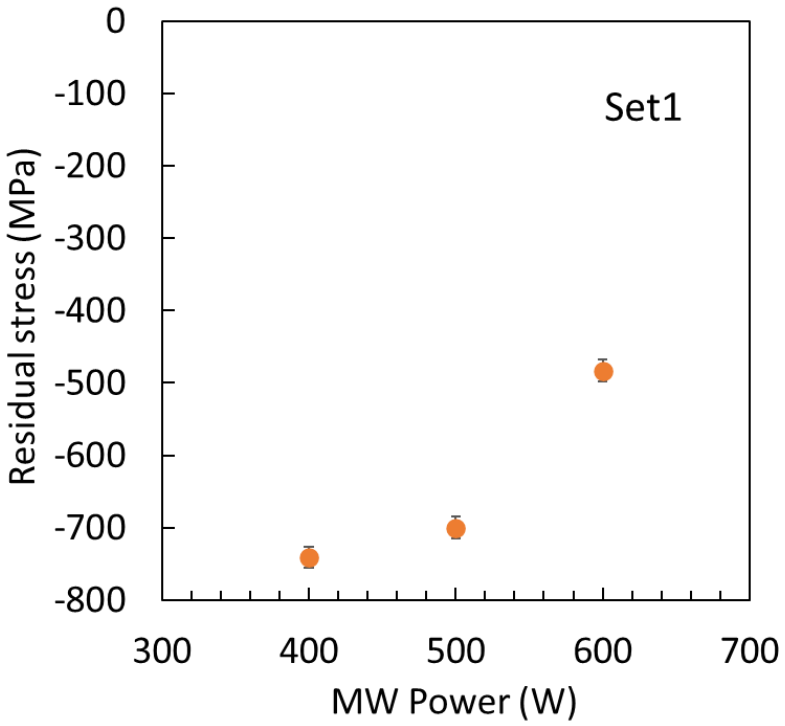

Figure 33: Residual stress vs. excitation power for 500 nm SiN_x films deposited within the ECR reactor. The samples were fabricated according to Set 1 from Table 2. [33]

Figure 33 shows that the ECR PECVD SiN_x films were all compressively strained, and higher injected microwave power produces less compressively strained films.

We observed that the deposition power affects the residual stress of the films differently in the two reactors. Therefore, a better understanding of residual stress during

the growth of thin films on semiconductor substrates is required. We assume that the changes in residual stress are mainly due to microstructural and/or chemical bonding modification within the deposited films resulting from the ion bombardment during the deposition. When we increase the deposition power in the CCP reactor, we provide more energy to the surface to release the hydrogen and increase the ion bombardment of the thin films, which increases the compressive component of the mechanical stress. Therefore, we turn the thin films from tensile to compressive. However, in the ECR reactor, we suppose that higher injected deposition power induces stress relaxation in the films and reduces the compressive stress in the films.

Further depositions were performed on the ECR PECVD reactor to study the impact of the processing parameters on the residual stresses that were evaluated using a FLEXUS available at the Ecole Polytechnique Montreal. We studied the impact of gas flows on the mechanical properties. The following results demonstrate experimentally how to tune the mechanical properties of SiN_x-based films by adjusting the N_2, and O_2 gas flows in an ECR-PECVD reactor.

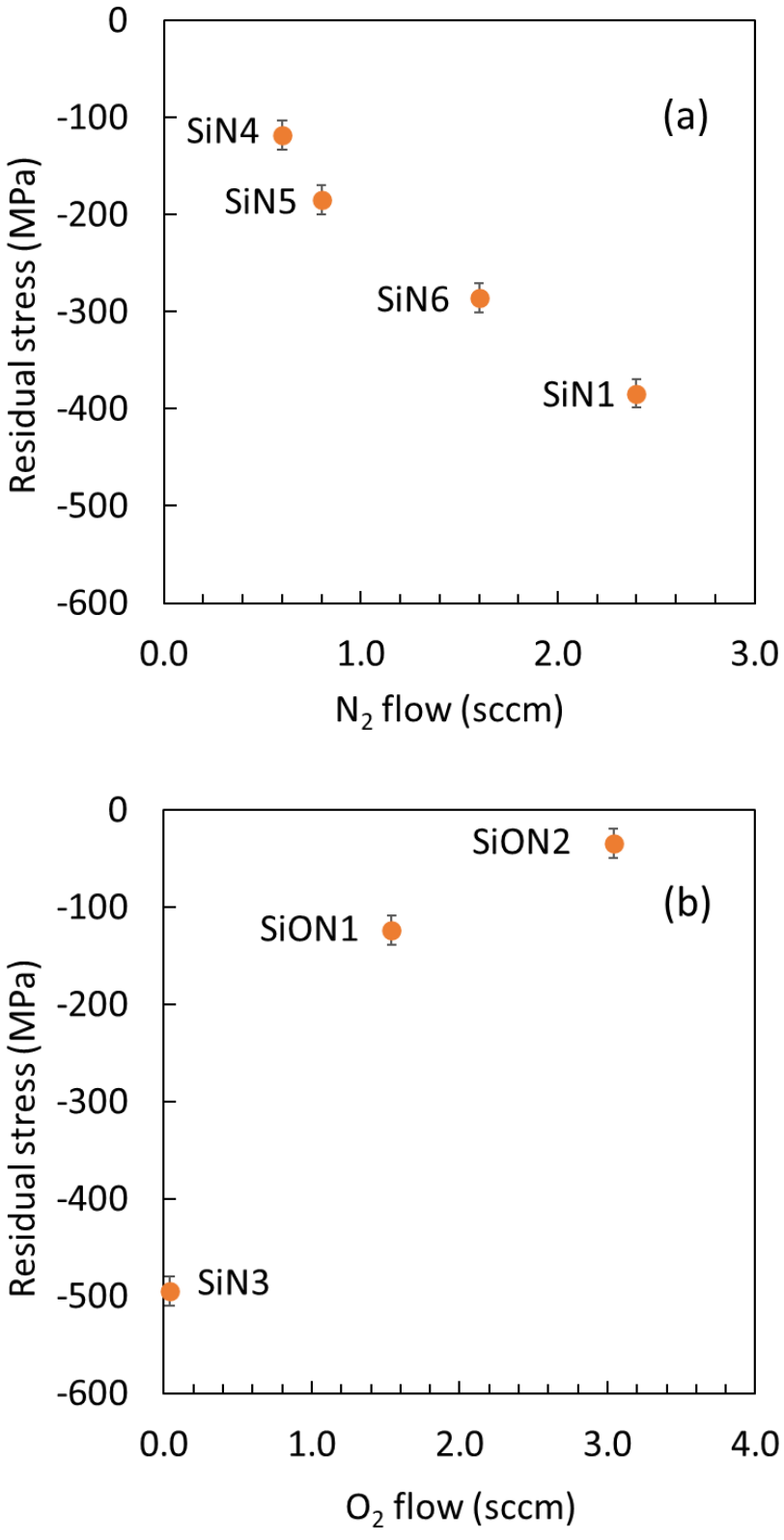

Figure 34: Residual mechanical stress vs. N_2 or O_2 flows for SiN_x films deposited within the ECR reactor. The samples correspond to Sets 3 and 4 from Table 3.

Figure 34 shows that N_2 and O_2 gas flows affected the residual mechanical stress of the films differently. The N_2 flow increases the compressive stress as shown in Fig. 34a, and the O_2 flow relaxes the mechanical stress as shown in Fig. 34b, while all the films are compressively strained.

To investigate our films' thermal properties and stability, we thermally cycled three SiN_x films deposited with the same N_2/SiH_4 flow ratio equal to unity and at different deposition pressures (3.3 mTorr, 4.6 mTorr, and 5.9 mTorr). They were exposed to a 400 °C annealing with continuous measurement of stress.

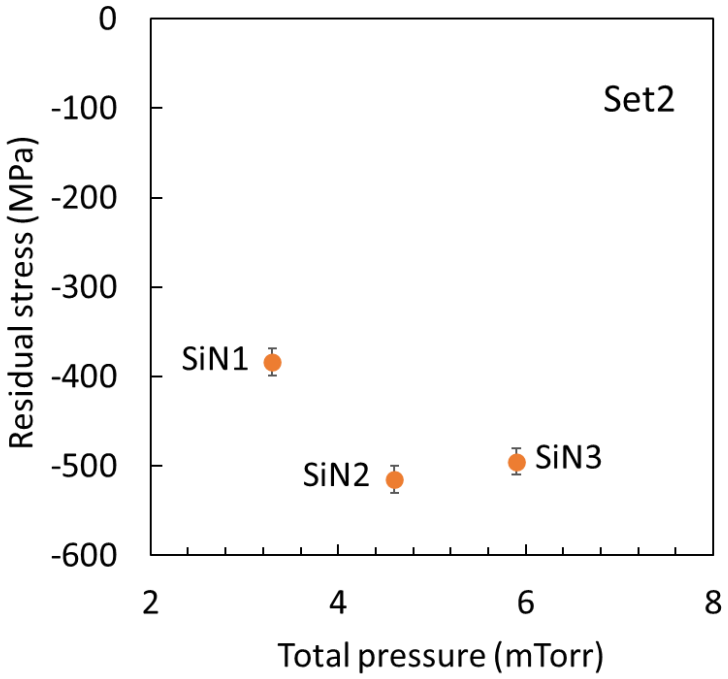

Figure 35: Residual mechanical stress vs. total deposition pressure for SiN_x films deposited within the ECR reactor. The samples correspond to Set 2 from Table 3.

We observe in Fig. 35 no clear dependence of the residual stress in the films on the total pressure. However, SiN1 has 100 MPa less compressive stress than SiN2 and SiN3.

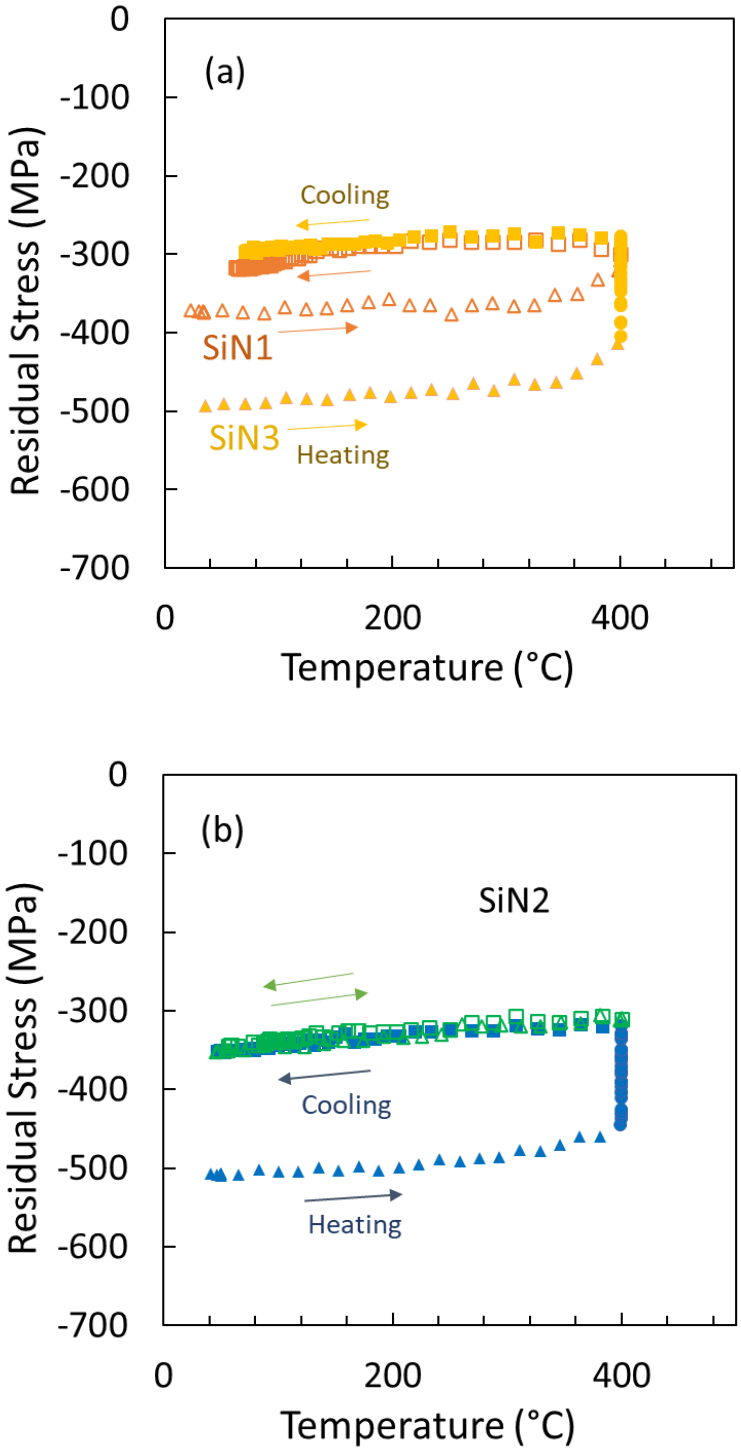

Figure 36: (a) Stress-temperature curves of the sample SiN1 plotted in open orange symbols and SiN3 plotted in solid yellow symbols. (b) Stress-temperature curve of the sample SiN2 doubly-thermally-cycled. Data points collected during the first thermal cycle are in solid

blue symbols; those collected during the second thermal cycle are in open green symbols (b). Data points collected during heating are triangles while holding the temperature at 400 °C are circles, and during cooling are squares.

Figure 36a shows the influence of the temperature variation on the residual stress of two films, SiN1 and SiN3, with different initial stresses. SiN1 film was not held at 400 °C, while SiN3 film was maintained at 400 °C for 1 hour and 10 minutes before being cooled down to RT. We observed a slight linear decrease in the overall compressive stress of the films while increasing the temperature. The stress variation was also linear during cooling, following an identical slope to the one during heating. We observed a faster and irreversible variation of the residual stress in the tensile direction around 400 °C, resulting in 67 MPa of stress hysteresis in SiN1 and 194 MPa of stress hysteresis in SiN3 after the thermal cycling. The stress hysteresis was substantial even for the sample SiN1, which experienced a rapid thermal cycle without maintaining the temperature at 400 °C.

In Figure 36b, we show the effect of double thermal cycling on the SiN2 film, with the first annealing longer than the second annealing. The two thermal cycles were consecutive, with no further hysteresis after the second one.

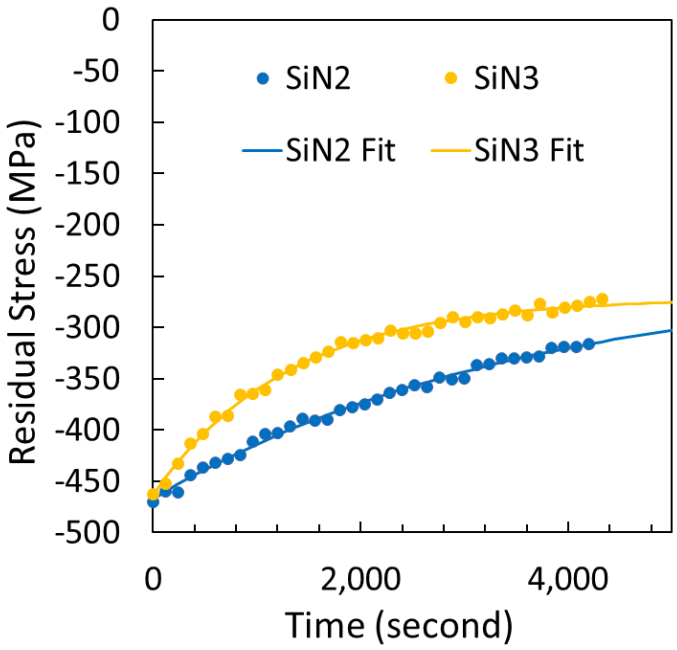

Figure 37: Stress-time curve of the samples SiN2 and SiN3 annealed at 400 °C for 1 hour and 10 minutes. The solid lines are the best fits of the experimental data using an exponential (Equation 15).

In Figure 37, we show the time-dependent behaviour of the SiN2 and SiN3 samples with the same initial stresses. However, we notice that irreversible stress generation occurs at different rates for the two samples. The films' mechanical stress seems to decrease toward some equilibrium compressive value. During the annealing time at 400 °C, irreversible stress variation follows an exponential decay with time as shown by the solid lines in Fig. 37.

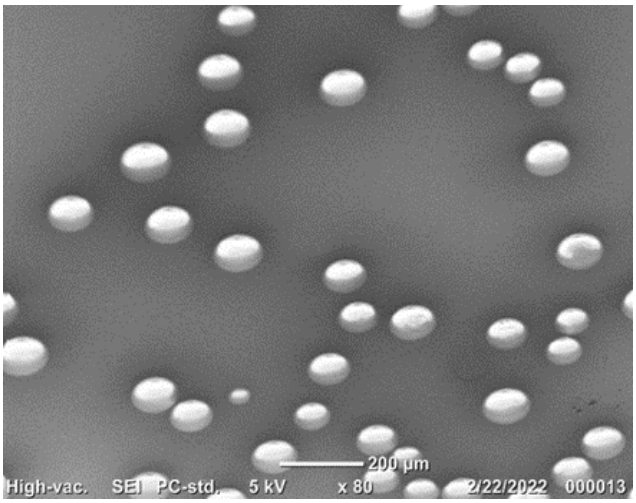

Figure 38: Scanning electron microscopy image of post-thermal-cycling delamination on sample SiN1 tilted at a 45-degree angle.

A simple observation of the samples under a scanning electron microscope (SEM) shows the appearance of circular delamination of the compressive SiN_x films after thermal cycling. Although the SiN1 film was not held at 400 °C, there was still a significant degree delamination at its surface post-thermal-cycling, as illustrated in Fig. 38.

The thermal cycling of these films shows irreversible variations in the residual mechanical stress. We evaluated the effect of low temperature annealing on three films that were deposited using the same N_2/SiH_4 flow ratio.

In Figure 36, we showed that the overall mechanical stress only increased by about 10 MPa between RT and the deposition temperature of 120 °C, which indicates that the global residual stress of the film is mainly induced by the intrinsic stresses produced

during deposition and not by the thermal mismatch between the film and the substrate. The linear stress variation was similar both during heating and cooling.

We used a linear model as a function of the annealing temperatures below 300 °C, where the thermal expansion phenomenon was observable. We evaluated the mechanical responses by fitting the linear function below (Equation 14) to the experimental data:

$$\sigma = AT + B \tag{14}$$

Where T is temperature, A is equal to the difference between the film coefficient of thermal expansion (CTE) and the substrate CTE times the elastic modulus of the film, B is equal to the initial residual stress during the heating, and equal to the final residual stress during the cooling of the films. The difference in thermal expansion coefficients between the film and the silicon substrate can be estimated using the elastic moduli measured by nanoindentation. One would believe that the delamination significantly impacts the film's perceived CTE after annealing; however, it was not the case in our films.

Table 5: The CTE values of the films were calculated using the CTE value of 2.6 ×10^{-6} °C^{-1} for the Si substrate [74]*, the values of the measured slope A of the stress-temperature curves, and the Elastic modulus of the films.*

ECR Films	A $_{Heating}$ (MPa/°C)	A $_{Cooling}$ (MPa/°C)	E (GPa)	CTE $_{Film}$ Heating (+/- 0.2 ×10^{-6} °C^{-1})	CTE $_{Film}$ Cooling (+/- 0.2 ×10^{-6} °C^{-1})
SiN1	0.07	0.12	175	2.2	1.9
SiN2	0.09	0.10	168	2.1	2.0
SiN3	0.09	0.09	154	2.0	2.0

Table 5 shows identical CTEs before and after annealing equal to 2.0 +/- 0.2 ×10^{-6} °C^{-1}. We found in the literature an estimated CTE value of 3.27 × 10^{-6} °C^{-1} for SiN_x films deposited by PECVD [75]. Our estimated and literature values are of the same order of magnitude, and we assume the difference is only due to the deposition conditions of the different films. Our results clearly show that the film CTE during cooling and heating were identical over the RT to 400 °C temperature interval, which confirms the VASE results in Chapter 3 that the microstructure of the films did not change significantly after annealing.

In our films, the values of A were at around 0.1, which means the residual stress induced by thermal expansion from the deposition temperature to the ambient was of the same order of magnitude as the stress measurement error of our system around +/- 10 MPa. Thus, the main contribution to the residual stresses at room temperature is the intrinsic component of the stress.

A better understanding of the mechanical responses of the SiN_x films during thermal cycling was required, especially while holding the sample at 400 °C, to evaluate the irreversible stress generation. In Fig. 37, we suggested the following analytical model (Equation 15) to fit our experimental data and describe the evolution of the residual stress at 400 °C:

$$\sigma = Ce^{-\lambda t} + D \tag{15}$$

Where t is time, C is a constant, λ is the rate at which irreversible stress generation occurs, and D is the final residual stress reached after a long time at a temperature of 400 °C.

It is worth noting that these fits are remarkably consistent for both samples, SiN2 and SiN3. If one would like to describe the behaviour of these films at higher temperatures, it is necessary to define a $\lambda(T)$ function because the rate λ is related to the temperature. After the annealing, the residual stress reached an equilibrium different from zero. The two samples had different rates of irreversible stress generation ($\lambda_{SiN2} = 2.8\,10^4\ s^{-1}$, $\lambda_{SiN3} = 7.7\,10^4\ s^{-1}$) even though they had similar initial stresses.

In the literature, irreversible stress generation has often been associated with stress relaxation, shrinkage of micro-voids existing in the films [69], or hydrogen evaporation, which changes the film's CTE [76]. In our study, irreversible stresses do not appear to be driven by structural modifications of the films since the optical properties of the

films remained unchanged after the annealing. We recognize that other stress relaxation mechanisms can also be attributed to stress hysteresis, such as the rearrangement of atoms at high temperatures to relax the film's compressive component. Still, we believe that we do not have sufficient energy to rearrange and form a tensile film state at 400 °C. We rather assume that the interfacial adhesion of the films is drastically affected during the thermal cycling due to defect generation at the interface with the substrate. We observed circular delamination from the underlying silicon substrate in compressive films at stress magnitudes lower than the initial stress, confirming our assumption. This delamination can be a significant failure mode that could affect the performance and reliability of the devices. The delamination is often viewed as an inconvenience, but they can be useful in flexible electronic devices if well-controlled [77].

4.3.2. Nanoindentation analysis

At the beginning of my Ph.D. program, we had the nanoindentation measurements done by an external laboratory using a NanoTest Vantage instrument to measure our first set of samples deposited by CC-PECVD. They determined the elastic modulus and hardness from a load-penetration curve measured with a maximum load of 1 mN and an average penetration depth through the samples of 50 nm, which corresponds to 10 % of the film's thickness.

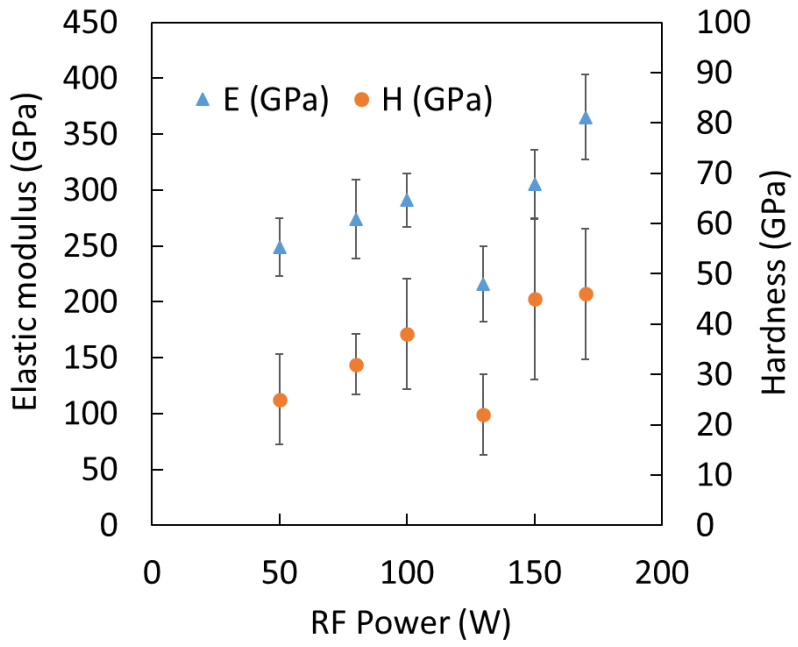

Figure 39: Elastic modulus and hardness from nanoindentation for 500 nm SiN_x films deposited by the CCP reactor with 130 W RF power (compressive built-in stress: -300 MPa). Substrate: Si. [33]

Figure 39 shows that elastic modulus and thin film hardness increase with the RF power; however, elastic modulus and hardness values are much higher than those in the literature for SiN_x films [1,2,78]. Since our first characterization of the elastic modulus was done externally, we developed an in-house technique to characterize the elastic modulus of thin films from microbeams, as presented previously. Later in this Ph.D. work, we collaborated with the Ecole Polytechnique Montreal, and I was trained to perform measurements and analyze nanoindentation data independently on an Anton Paar Ultra Nanoindentation Tester ($UNHT^3$). We examined the elastic modulus and hardness of SiN_x and SiO_yN_x films for various chemical compositions. The

nanoindentation results showed that the elastic modulus and the hardness evolved similarly according to N_2 or O_2 gas flows introduced into the plasma during the deposition of the ECR-PECVD films.

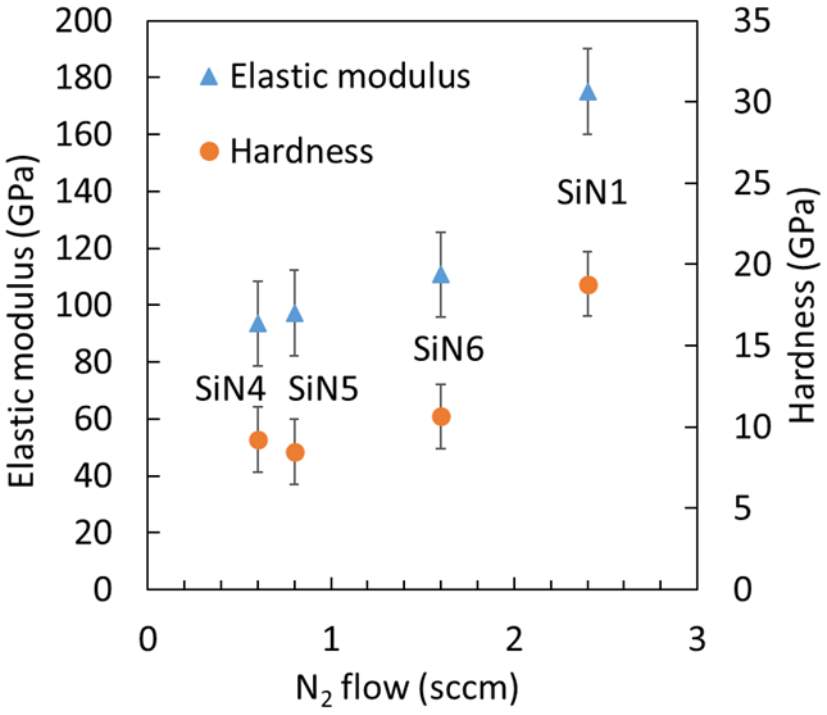

Figure 40: The elastic modulus and hardness variation measured using nanoindentation at 10 % of the thicknesses of the films as a function of the N_2 flow for SiN_x.

Figure 40 shows that the elastic modulus and hardness of the SiN4 and SiN5 layers are very close to the mechanical properties of low-hydrogenated amorphous Si films presented in [79], however, the elastic modulus and hardness of SiN_x films increase significantly with N_2 flows higher than 1 sccm. Thus, we approach elastic modulus and hardness values close to those in the literature [1,2,78] for SiN_x films between 100 GPa and 160 GPa.

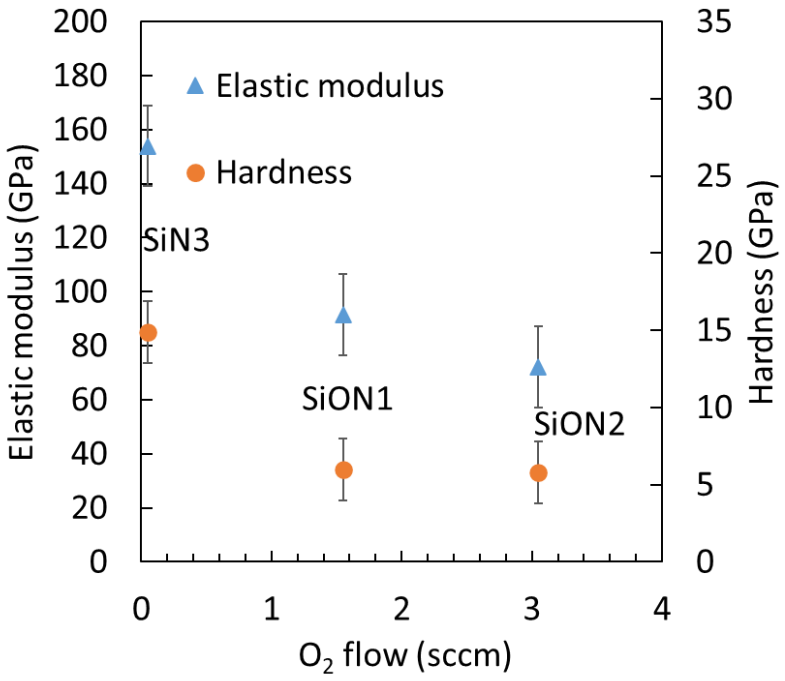

Figure 41: The elastic modulus and hardness variation measured using nanoindentation at 10 % of the thicknesses of the films as a function of the O_2 flow for SiO_yN_x.

In contrast, Figure 41 shows the opposite effect during the introduction of O_2 flow, where we notice a decrease in the elastic modulus and a softening of the films. Since SiO_yN_x layers had very similar optical properties to SiO_x, in Chapter 3, we expected that the elastic modulus and hardness of SiO_yN_x films would vary similarly and decrease significantly towards the mechanical properties of SiO_x [80].

This is followed by a section presenting the mechanical properties of SiN_x films measured using a different technique developed during this PhD to characterize the elastic

modulus of thin films from released microbeams and not influenced by the substrate properties.

4.3.3. Release of microbeams analysis

We performed the microbeam analysis on 22 microbeams per layer of different compressive stresses (four layers in total). We selected microbeams of different lengths and widths, as shown in Figure 28, to have a good estimation of error bars. All deformation states (downward or upward) were considered in our analysis to calculate the elastic modulus values of the films.

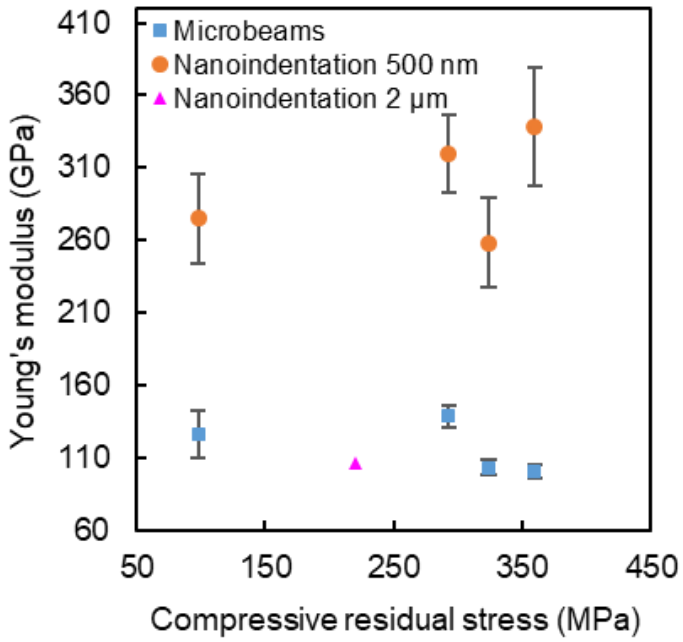

Figure 42: Elastic modulus of SiN_x films with compressive built-in stress deposited on Si using a CCP reactor. [33]

Figure 42 shows the elastic modulus of compressively strained SiN_x films using the microbeams technique and nanoindentation. The elastic modulus values from nanoindentation measurements appear to be higher than those from the microbeams elongation, except for thick films. We can notice a slight increase in elastic modulus for the nanoindentation measurement while elastic modulus measured from the microbeams elongation seems unchanged and slightly decrease for large compressive stresses. As discussed in Ref. [81], the compressive built-in stress would also affect the nanoindentation results by increasing Young's modulus. As a matter of fact, the estimation of SiN_x films' Young's modulus in thin films using different methods is not trivial, and we believe that the results of nanoindentation performed on thick layers are more reliable for future modeling. It is also possible to use the microbeams technique to evaluate the elastic modulus of layers less than 500 nm thick. If we compare the range of values of the elastic moduli measured by nanoindentation more recently on a more precise nano-indenter, we obtain values between 100 GPa and 160 GPa, very close to those measured by microbeams on different samples and those in the literature[1,2,78].

The mechanical properties of amorphous SiN_x-based multilayer structures are shown in the following part.

4.4. Characterization of the mechanical properties of silicon nitride-based multilayer structures

4.4.1. Residual stresses in multilayer structures

It is common to find multilayer structures with hundreds of individual layers since the number of layers significantly influences the performance of some optical devices. However, the mechanical stress of each layer can lead to excessive deformation and sometimes the deterioration of optical devices. Thus, it is necessary to control and characterize the mechanical properties of multilayer structures. We discussed in Chapter 3 how to fabricate and characterize the optical properties of multilayer structures and measure their thickness profiles using VASE. This study mainly focuses on characterising the mechanical properties of SiN_x-based multilayer structures using curvature measurements and nanoindentation.

In this work, we first studied the effect of mechanical stress on multilayer structures designed with identical 100 nm thick layers (2L, 4L, 6L, with L for layers). Then, we designed a multilayer structure considering its mechanical and optical properties to make an optical notch filter, as discussed in Chapter 3. The notch filter was designed using a quarter-wave thickness structure and an optically optimized structure. All structures obtained by simulation were fabricated using SiN_x-based multilayers. We used a weighted average of each monolayer's residual stress considering its estimated thickness, to predict the overall multilayer residual stress. The predicted residual stress

was compared with the measured residual stress from the wafer curvature. Since the Stoney formula does not consider the elastic modulus of the films, we were able to measure the global residual stress of multilayer structures according to the global thickness of the multilayer structure.

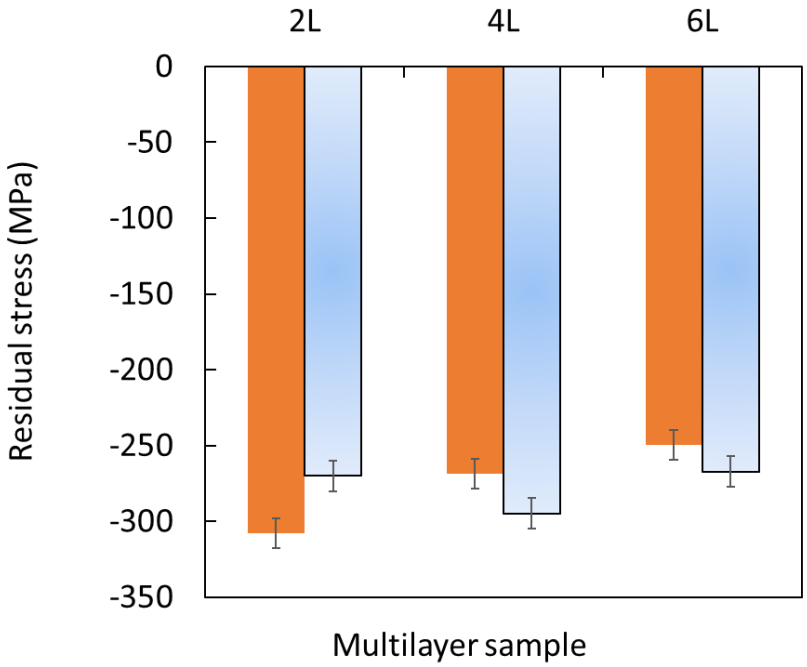

Figure 43: Three multilayer structures with 2, 4, and 6 layers of 100 nm each deposited on a Si substrate. The measured residual stress values are in solid orange color, and the predicted residual stress values are in a grading blue color.

Figure 43 shows a slight difference between the measured stresses and those predicted, which can be due to several reasons, among them the uncertainty of the thicknesses of the layers predicted by the model VASE. We also notice that the overall residual stress does not depend on the number of layers in multilayer structures as long as the

SiN/SiON thickness ratio remains constant. However, even if the residual stress remains the same, the forces applied on the substrate increase with the thickness, without any controlled relaxation mechanism, the layers can delaminate from the substrate.

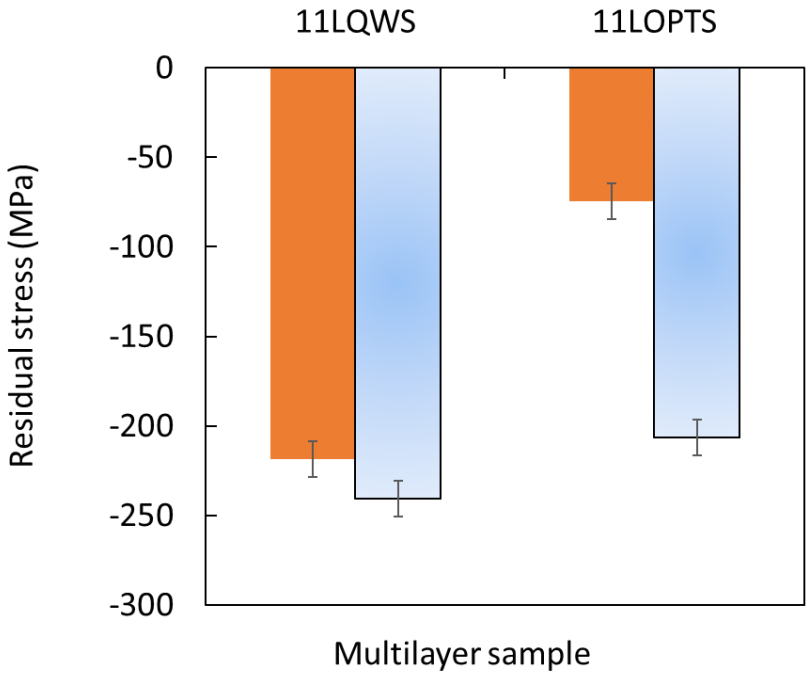

Figure 44: 11-layers notch filter structures with a QWS and an OPTS profiles. The measured residual stress values are in solid orange color and the predicted residual stress values are in grading blue color.

Figure 44 shows a similar comparison between the measured and predicted residual stresses for the 11L quarter-wave thickness (QWS) sample, where a periodicity in the thicknesses of the layers is followed. However, the measured residual stress in the 11L optimized thickness (OPTS) sample is significantly lower than the predicted residual

stress. In the case of 11L OPTS, all the thicknesses of the stack are different and few of them are very thin less than 10 nm (see Figure 19) compared to the 11L QWS where all layers are above 40 nm and vary with periodicity (see Figure 17).

We can explain this reduction of residual stress by the non-periodicity of the layer thicknesses in the optimized structure. Thus, the thicker layers can apply higher interface forces on much thinner layers leading to partial stress relaxation at the interfaces between the layers. However, in the previous Chapter, we noticed that the optical properties of the optimized filter were not significantly impacted by this drop in residual stress. Thus, we assume that stress relaxation did not introduce macroscopic geometric changes to the structure. Integrating the mechanical component into the optimization process to optimize the design of multilayer structures will be interesting, considering both the optical and mechanical properties.

4.4.2. Nanoindentation analysis of multilayer structures

To characterize the elastic properties of thin films, it is necessary to decouple the contribution of the thin films from that of the substrate. We usually circumvented this problem by limiting our nanoindentation measurement to 10 % of the film's thickness, illustrated by a dashed black line in Figure 45. It is, however, difficult to limit our measurements to 10 % of the thickness when this one is very low, less than 300 nm thick. We use films with a thickness between 10 and 140 nm in our multilayers, meaning measurements between 1 and 14 nm should be used to determine their elastic

properties. However, the tip size effects can extend up to 50 nm from the surface, making such measurements nearly impossible on our thin films. It is even more challenging to perform these measurements on multilayer structures, where several films contribute together to nanoindentation.

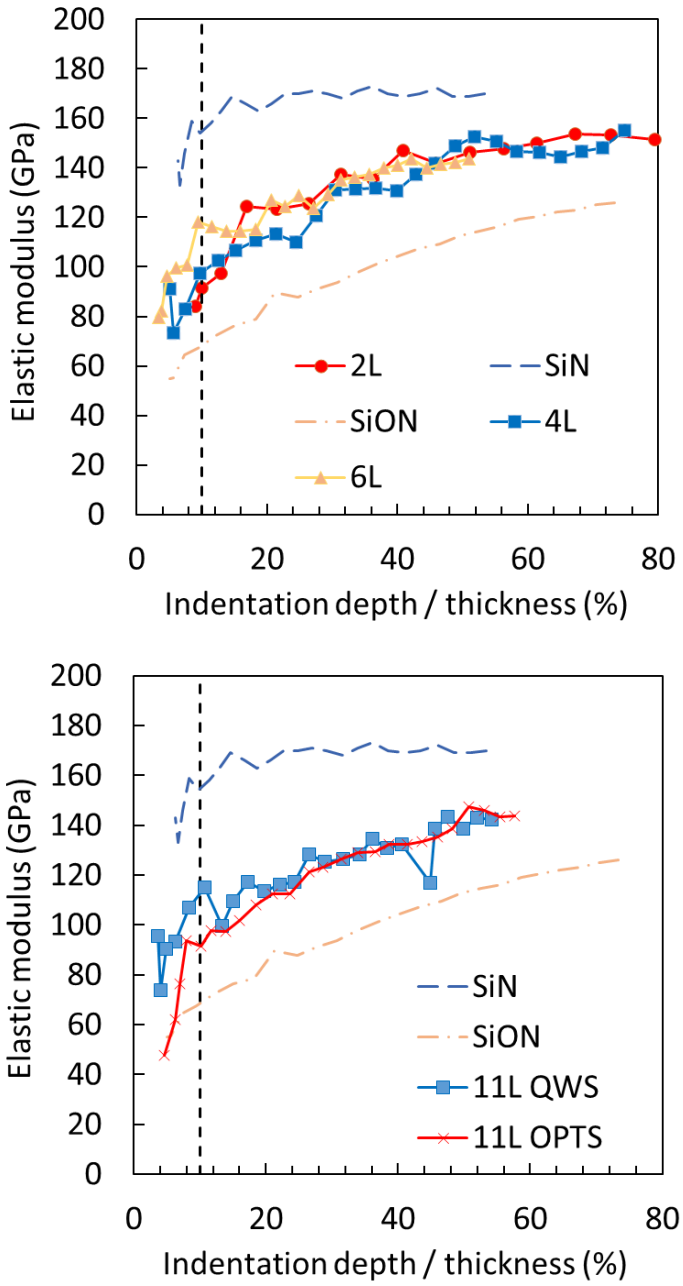

Figure 45: Elastic modulus of SiN_x-based monolayers and multilayers on Si substrate versus normalized indentation depth.

Figure 45 shows an elastic modulus of a SiN_x monolayer around 160 GPa and a SiO_yN_x monolayer around 70 GPa at 10 % of the thickness. The multilayer structures had elastic moduli between 70 GPa and 160 GPa since all layers contributed to their elasticity. We notice that the elastic modulus changes significantly as a function of the thickness and approaches the elastic modulus of the Si substrate (169 GPa)[82]. These variations can be correlated with the presence of different materials in the multilayers. It is possible to develop empirical, semi-empirical, or analytical models to decouple the contribution of each layer to the elasticity of the multilayer structure and the influence of the substrate. However, applying these models to process the obtained curves is complex and slow [83,84] and requires the knowledge of parameters that are difficult to determine with precision and reliability. Thus, we can reduce the elastic behaviour of the multilayer structure to an average of Young's moduli of the different layers according to their thickness.

4.5. Conclusions

We discussed, in this Chapter, SiN_x-based thin films with tunable mechanical properties fabricated by employing an ECR-PECVD reactor. We characterized the residual mechanical stress using wafer curvature measurements and estimated the films' elastic modulus and hardness using nanoindentation. Just as the optical properties in Chapter 3, the layers' mechanical properties were also significantly affected by gas flow variation. We also studied the effect of post-deposition thermal cycling on the properties of the films. We realized that the residual stresses generated by the thermal mismatch between the deposition and ambient temperature were not the main contribution to the stress and the global stress was mainly intrinsic. We also quantified the rates of irreversible stress generation according to annealing time at 400 °C, which we suppose is useful for studying the generation of delamination in thin compressive layers and investigating the interface conditions between the coatings and the substrate. Finally, we studied the mechanical properties of multilayers using a global weighted residual stress measurement and a nanoindentation measurement in a CMC mode to evaluate the elastic modulus of the multilayers over the indentation depth.

5. Study of the Induced Strain in a Semiconductor Substrate

5.1. Introduction

We studied in the previous Chapters how to control the optical and mechanical properties of SiN_x-based films by tuning the PECVD process parameters. We investigated the residual stress/strain of the films at a macroscopic scale using wafer curvature measurements. In this Chapter, we propose studying the effect of SiN_x thin films as stressor layers on bulk semiconductors at the microscopic scale using optical methods. As discussed in Chapter 1, the strain field induced by a stressor layer on a semiconductor material varies the material's optical properties, which is particularly interesting in designing photoelastic waveguides [15]. Stressor stripes can induce variations in the refractive index beneath them and define a guiding region in the semiconductor without requiring the use of several materials (core and cladding). For that reason, we structured SiN_x stressor layers into elongated stripes using optical lithography and etching. Then, we evaluated the locally induced strain field in the underlying substrate using micro-photoluminescence (micro-PL) for GaAs and micro-Raman spectroscopy for Si. Many research groups measured the spectrally resolved PL, analyzing the spectral shift of the band-to-band transitions in bulk semiconductors to evaluate the local strain [32,85,86]. In this research project, we used a technique proposed by Cassidy et al.[87] where the degree of polarization of the PL (DOP-PL) is used to investigate the anisotropic part of the strain tensor locally.

As an illustration of strain distribution in indirect bandgap semiconductors, we measured a micro-Raman profile across a stressor stripe on a Si substrate. However, we will mainly focus in this Chapter on results obtained by the DOP-PL measurements on GaAs and compare them with numerical simulations performed on COMSOL Multiphysics®.

First, we give a brief description of the DOP-PL method used to measure our samples, and then we discuss the experimental and simulation results obtained from both surface and cross-section measurements.

5.2. Experimental details

5.2.1. Degree of polarization of the PL

The principle of DOP-PL measurement is to excite the material's PL at room temperature using a 635 nm red laser focused on the semiconductor's surface. Note that the DOP-PL technique uses the spectrally integrated PL signal. As discussed in [87], we can suppose that substrates emit PL radiation polarized according to the stress state of semiconductors, where the anisotropic deformation of a cubic crystal such as GaAs or InP induces a DOP-PL.

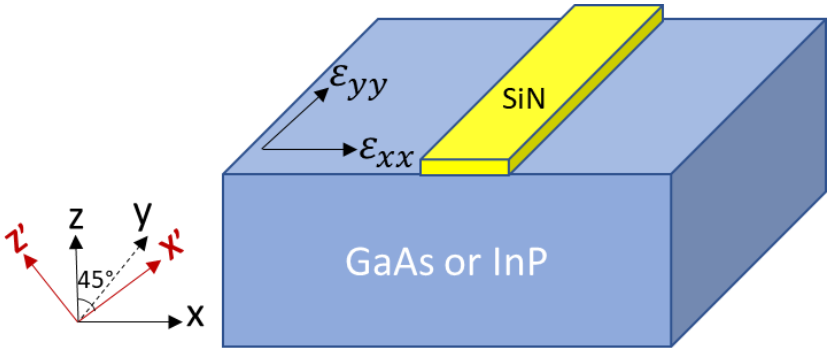

Figure 46: Geometry of a SiN_x stripe on an InP or GaAs (100) substrate.

We define the DOP-PL for the material under study as:

$$DOP_y = \frac{L_x - L_z}{L_x + L_z} \tag{16}$$

where L_x, and L_z are the measured irradiance for light polarized along the x, and z directions, respectively. "y" denotes the propagation direction for both the excitation

laser beam and the detected PL signal beam, “x” and “z” are two directions in the perpendicular plane, as shown in Figure 46. More precisely, we assume in [87][88] that DOP-PL signal is related to the difference in the normal strain coefficients with two orthogonal directions in the plane perpendicular to the laser beam used for these measurements. The DOP-PL, as measured on the cross-section, is related to the strain by the following formula [88] (see Fig. 46 for the x, y, and z axes):

$$DOP_y = -C \cdot (\varepsilon_{xx} - \varepsilon_{zz}) \tag{17}$$

where $(\varepsilon_{xx} - \varepsilon_{zz})$ denotes the difference in the normal components of strain [87]. The DOP constant C depends on the semiconductor material, and it has been reported that C = 50 +/- 10 for GaAs [87]. Thus, a positive DOP signal indicates that the crystal deformation is locally more compressive (or less tensile) in the x-direction than in the z-direction for the case of the (110) cross-section measurements.

We scanned the samples with a step of 0.5 µm and a laser spot diameter of the order of a micrometre. The sensitivity of this technique to local strains is very high; strains as low as 10^{-5} can produce detectable DOP-PL signals [87]. Thus, we can measure the anisotropic stress associated with a precision of the order of MPa.

Recently, Schaub et al.[34] developed an updated acquisition setup to show maps of the degree of linear polarization of PL (DOLP-PL) proportional to the anisotropic

strain and orientation maps of the linear component of the PL polarization state, which is a principal axis of the strain.

5.2.2. Set of samples

All the SiN_x thin films used in this part were fabricated using the CCP reactor with controlled deposition conditions. The built-in stress in these thin films was adjusted by controlling the deposition power. We prepared SiN_x thin films with different built-in stresses: (-280 MPa, -293 MPa) compressive films and (164 MPa, 285 MPa) tensile films.

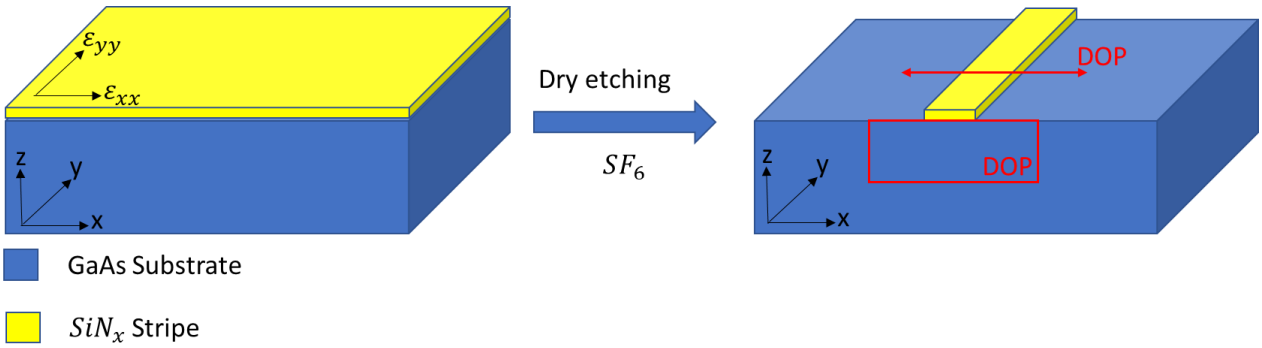

Figure 47: SiN_x stripe patterned by photolithography and etched by reactive ion etching using an SF_6 plasma on a GaAs (100) substrate. Scan-line for the DOP measurement from the surface and square for the cross-section measurement area.

The films were subsequently patterned by photolithography and etched by reactive ion etching using an SF_6 plasma, as shown in Fig. 47. Similar to the microbeams process, the photolithography step was carried out with a positive photoresist using a so-called "maskless" equipment (Smart Print UV from microlight 3D company). The

patterns design, simple to implement in our case, has remained similar to the microbeams fabrication. However, the stripes were aligned to the crystallographic axis [110] and [1-10] of the GaAs crystal. After a dry etching by SF_6 plasma and removal of the photoresist layer, stripes with a length of 1.2 mm and a width comprised between 5 µm and 50 µm are formed. Such stripes acting as stressors on the GaAs can be seen in Figure 48.

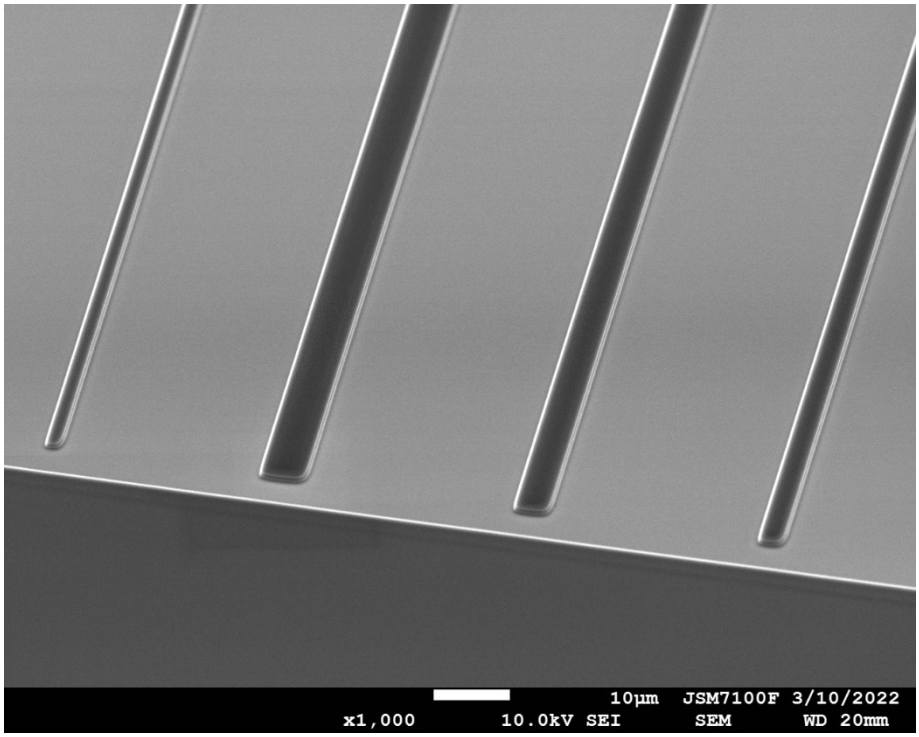

Figure 48: SiN_x stripes on GaAs obtained after deposition with the CCP reactor and a dry etching process using an SF_6 plasma.

Then, we performed DOP-PL measurements to map the magnitude and distribution of residual mechanical strain in GaAs (100) substrates induced by the presence of strained SiN_x stripes. We measured the samples from the top surface but also in cross-

section configuration. Compressed SiN_x stripes were fabricated on Si for micro-Raman measurement following the same process.

5.3. Results and discussion

5.3.1. Strain mapping beneath a stressor layer

We note that the length of the stripes was significantly longer (a few millimetres) compared to their width (microns). So, we can consider the stripes infinite along the y-axis and assume that the stress relaxes mainly along the x direction on the xy plane, see Fig. 47. For a stripe that is infinite along the y direction, it has been shown in [32] that the plane strain approximation in the (x,z) plane is valid for these samples. Therefore ε_{yy} can be considered negligible.

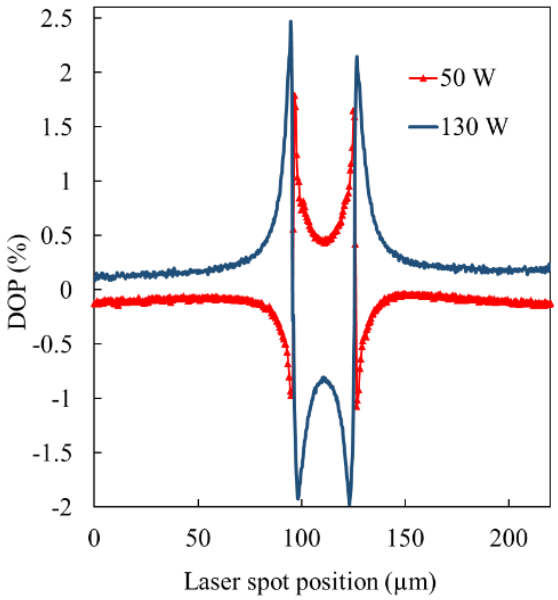

Figure 49: DOP-PL top surface GaAs for two different SiN_x 20 µm stripes (initial residual stress before etching: 285 MPa tensile in red (50 W) and -293 MPa compressive in blue (130 W)) deposited by a CCP reactor on GaAs substrate. [33]

Figure 49 shows DOP-PL measurements performed on a GaAs sample from the top surface across the stripe. Due to the limited penetration of the excitation laser at 635 nm, the PL signal collected in this configuration is a weighted average of the PL signal in the 100 nm absorption depth in the substrate material beneath the surface [88]. We can also observe, in Fig. 49, sharp peaks near the stripe edges, with opposite signs inside versus outside the stripe. This behaviour of the perpendicular strain ε_{xx} is the signature of the discontinuity occurring after etching the stressor films and was first analyzed more than thirty years ago in the framework of the edge force model [89]. This model was further sophisticated, considering that the stress in the thin films undergoes relaxation near the edges (see discussion in [32]). The DOP-PL line scans reveal other interesting features in Fig. 49. First, the DOP-PL signal remains finite near the stripe centre, which shows that the strain cannot be considered biaxial near the stripe centre, even if this stripe is "broad". Second, the perpendicular strain propagates in the semiconductor outside the stripe over distances of several tens of µm.

In the case of indirect gap semiconductors, the PL technique is not applicable for stress measurements. Then, the micro-Raman technique is appropriate and has been widely used [90]. However, data acquisition time is considerably longer in micro-Raman than in micro-PL because the Raman signal is orders of magnitude lower than the PL signal. Here we just illustrate the technique with a single top surface line scans performed by Alain Moreac (R&D engineer at University of Rennes) on our Si samples

covered by a SiN_x stripe deposited by PECVD with built-in compressive stress, as shown in Fig. 49.

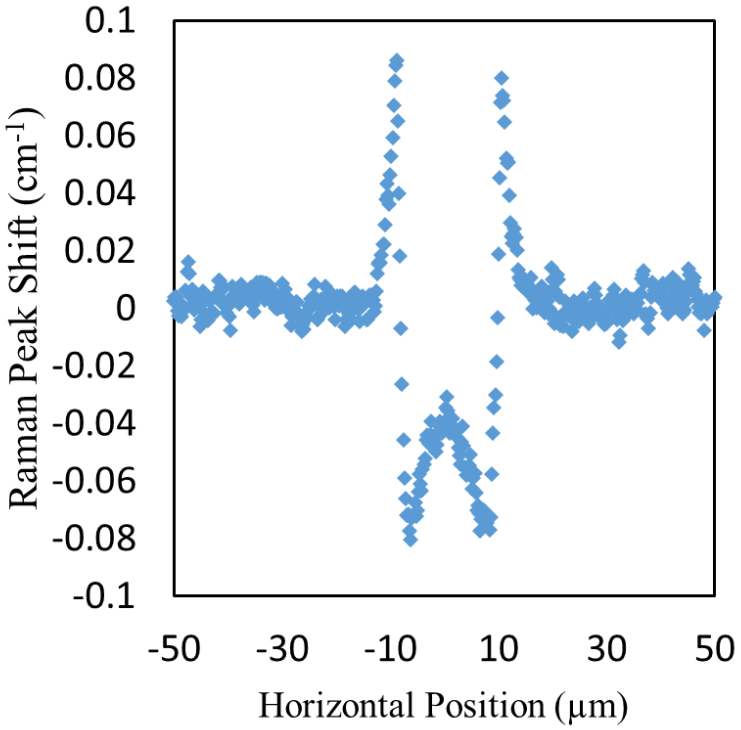

Figure 50: Raman shift profile measured from the surface across a SiN_x stripe deposited by PECVD on Si (stripe width 20 µm / built-in stress – 280 MPa).

We note that the Raman shift is a good approximation measurement of the hydrostatic (isotropic) crystal deformation unless some complex Raman line shape modelling is performed [90]. Strain shifts the Raman scattering peaks of semiconductors, and the sign of this shift depends on the nature of the strain, either compression or tension. Positive shifts correspond to compressive stress and negative ones to tensile stress. Fig. 50 reveals a trend similar to that shown in Fig. 49, where the strain /stress discontinuities at the stripe edges govern the shape of the experimental curves.

We also prepared cleaved samples to measure the cross-section of DOP-PL mapping beneath stripes with different widths and residual stresses. After carefully cleaving the sample through the SiN_x stripe, we performed measurements from the cross-section to investigate the strain distribution induced by the stressor stripe.

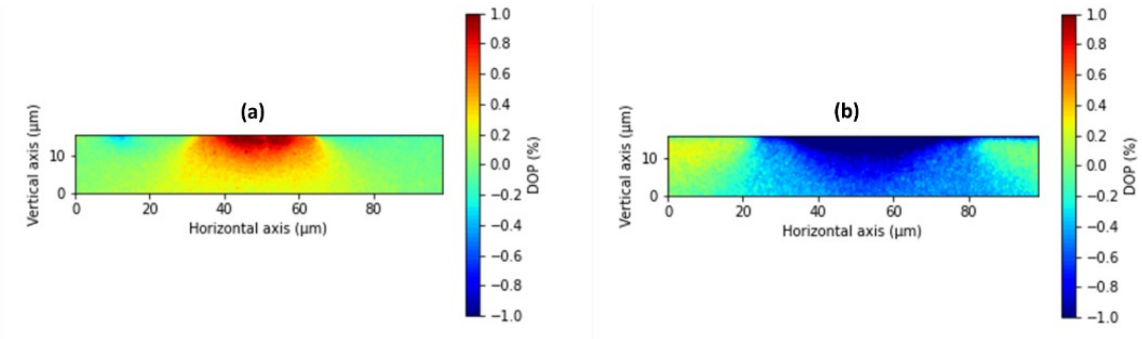

Figure 51: DOP-PL cross-section of GaAs for two different SiN_x stripes (20 µm stripe in tension at 164 MPa (a) and 50 µm stripe in compression at -280 MPa (b)) deposited within the CCP reactor on GaAs substrates. [33]

It is interesting to note in Fig. 51 that for both the 20 µm wide tensile stripe and the 50 µm wide compressive stripe, the anisotropic deformation in the semiconductor bulk is significant up to 10 microns in depth. However, dielectric thin films reverse the sign of the anisotropic strain due to the difference in residual stress.

So far, the results deal with crystal deformation measurements or mappings performed within the semiconductor. These measurements, of course, do not require knowledge of the semiconductor or dielectric thin film elastic properties. However, these

properties are required, for example, if one wants to perform accurate simulations of the crystal deformations. Whereas the elastic properties of most standard semiconductor materials are rather well known, this is not at all the case for dielectric thin films. As shown in Chapter 4, the mechanical behaviour is highly dependent on the deposition conditions and requires a detailed characterization. Thus, we have used the elastic properties of the dielectric thin films from Chapter 4 to perform accurate simulations of the crystal deformations in the following part.

5.3.2. Finite element simulations

It is essential to build numerical models of the strain effects produced by stressor layers on semiconductors to help predict changes occurring on photonic devices from strain engineering using stressor layers. For this reason, we chose a finite element approach to have an efficient tool for designing photonic components. We included different differential equations to account for the linear elasticity of different materials involved, such as the semiconductor substrate and dielectric stripe stressor.

We used COMSOL Multiphysics® for our numerical approach to coupling different deformation mechanisms. In addition to this choice, an important issue was choosing between a two-dimensional (2D) versus a three-dimensional (3D) simulation. When the designed components have a long enough dimension, such as stripes with a length at least 100 times higher than their thickness and width, the 2D model with plane strain assumption [91] is appropriate. For instance, it allows for an accurate calculation

of local materials' properties affected by stress, such as the refractive index in any cross-section. We have checked the validity of the 2D simulation for long devices such as stressor stripes at the surface. To illustrate this, we have defined a SiN_x stripe with initial bi-axial stress equal to the built-in stress deduced from the curvature measurements. We chose this method as the one most similar to the experimental process, where the stripe is defined by etching through a dielectric thin film with initial built-in stress. We have tried validating our numerical simulation approach by comparing it with the DOP-PL profiles and maps measured experimentally. The COMSOL simulations were performed using a two-dimensional plane strain model with standard free surface conditions and prescribed displacements. We took the elastic properties of the GaAs substrate from the literature [46] and our experimental estimation from microbeams (see Chapter 4) for the deposited SiN_x thin film.

For the top surface measurements, the DOP formula is:

$$DOP_z = -C \cdot (\varepsilon_{xx} - \varepsilon_{yy}) \tag{19}$$

We cannot use this formula directly because the normal deformations ε_{xx} and ε_{yy} vary strongly along the vertical dimension z (see Figure 47 for the x, y, and z axes). A generalized formula, considering the penetration depth for the excitation laser beam, has been proposed and validated against experimental data for the case of an extension of the analytical edge force in Ref.[32]. However, applying this formula in the

framework of our numerical simulations, even in the 2D approach, consumed a lot of computer time. Thus, we used (Equation 19) and adjusted coefficient C to provide the best agreement with the experimental DOP-PL measurements.

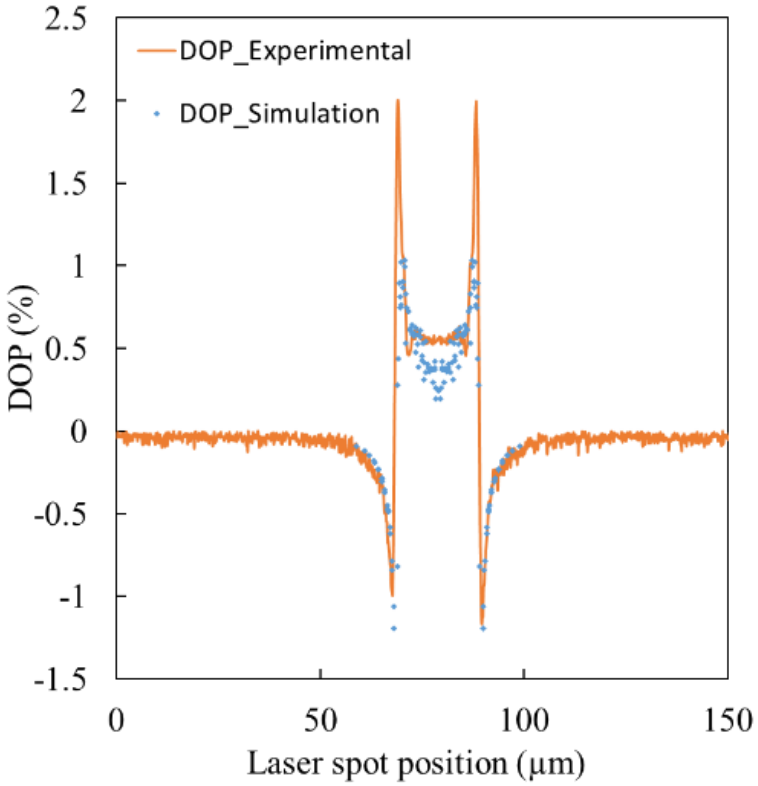

Figure 52: A comparison of DOP-PL simulations with DOP-PL line scans on the top surface of a 20 µm SiN_x stripe with 164 MPa tensile stress. [33]

The resulting experimental and numerical line scans are shown in Figure 52. As can be seen, the agreement is correct (determination coefficient R^2 =0.78).

We also performed a simulation of the DOP-PL signal from the cross-section to compare them with the experimental maps of Fig. 51. We used a 2D plane strain model with standard free surface conditions and prescribed displacements. We considered

initial bi-axial stress in the films equal to the built-in stress deduced from the curvature measurement.

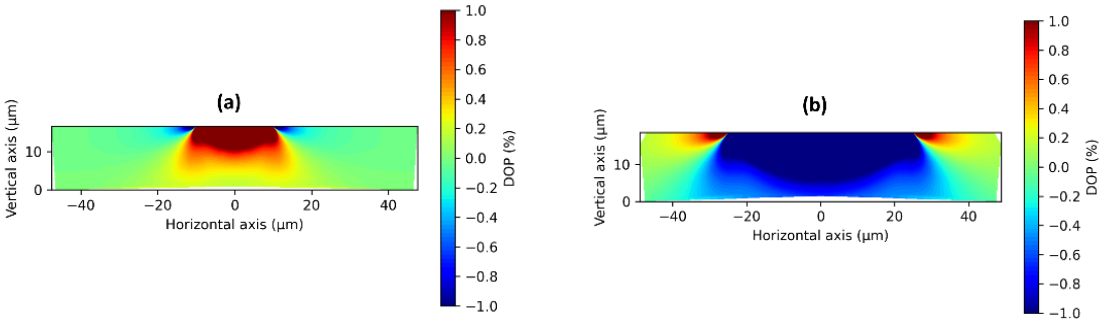

Figure 53: DOP-PL simulations for two different SiN_x stripes, a 20 µm stripe in tension 164MPa (a), and a 50 µm stripe in compression -280MPa (b), on GaAs substrates. [33]

Fig. 53 shows details of the DOP-PL signal, which are not all identified on the experimental map, especially in the edges. We attribute this to the limited spatial resolution (~ 1 µm) of the experimental DOP-PL maps. We can notice an agreement with Fig 51. The anisotropic deformation in the semiconductor bulk remains significant at more than 10 microns in depth. The comparisons of the DOP results with the simulation were satisfactory. As discussed in Chapter 1, the induced mechanical strain can modify materials' refractive index and allow the fabrication of photoelastic waveguides. Thus, we used the same finite element model used to reproduce the DOP results in this Chapter to calculate the refractive index maps of GaAs under a SiN_x stressor stripe using the photoelastic coefficients of GaAs [11].

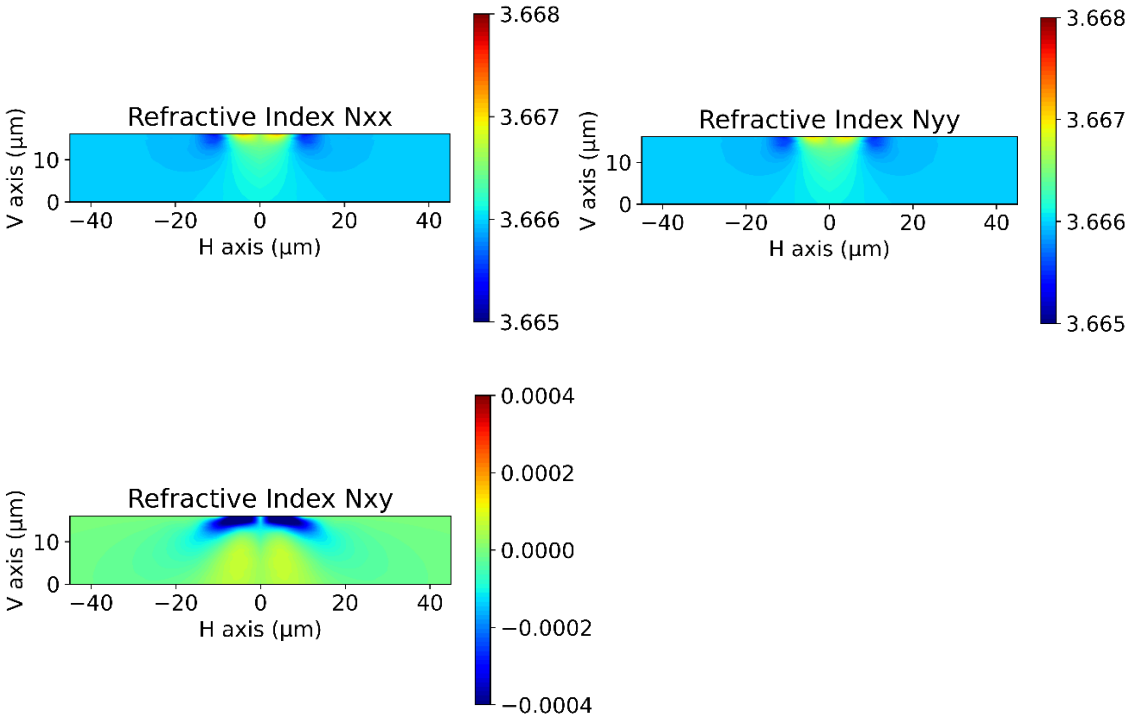

Figure 54: Simulation of refractive index distribution in the cross-section of GaAs under a 20 µm wide SiN_x stripe in compression at -280 MPa.

Figure 54 shows the refractive indices n_{xx}, n_{yy}, and n_{xy} maps in bulk GaAs under a 20 µm wide SiN_x stripe in compression at -280 MPa. We note that this stressor SiN_x stripe induced a spatial modulation of GaAs refractive index in both lateral (n_{xx}) and vertical (n_{yy}) directions for about $\Delta n \sim 0.01$. It results in a higher refractive index beneath the compressive stripe, which goes in the direction of what would be needed to guide the light under the stressor layer. These refractive indices values were calculated for a wavelength of 1.15 µm, but we do not expect them to change significantly for other energies below the bandgap of GaAs.

5.4. Conclusions

This Chapter focused on experimental techniques for determining local strain field distribution in the vicinity of a dielectric thin film structure deposited on a semiconductor substrate. For III-V semiconductors, we used DOP-PL measurements, while micro-Raman spectroscopy was used for a Si substrate. Then, we compared some results obtained on GaAs with numerical modelling of the mechanical stress distribution induced into semiconductor materials by the presence of thin film dielectric structures using COMSOL Multiphysics®. The comparisons of the results with simulation were satisfactory, making it possible to validate the quality of the characterisation methods that have recently been developed. Last, we showed how the strain field induced by a stressor layer on a GaAs varies the material's refractive index, which is particularly interesting in designing photoelastic waveguides

6. Conclusions and Perspectives

The following sections provide a summary of the work carried out during our research journey and offer perspectives for future work enabled by our studies.

6.1. Summary

In this research work, we aimed to achieve progress in the integration of strain engineering techniques in optoelectronics manufacturing through the control of the physical properties of dielectric thin films and studied their impact on IIIV semiconductors. A variety of experimental studies were performed, whose primary objective was to better understand and characterize the optical and mechanical properties of SiN_x-based thin films deposited by plasma-enhanced chemical vapour deposition (PECVD). The obtained results made it possible to control the properties of SiN_x-based thin films and fabricate real devices such as multilayer optical filters and stressor layers. Simulations were used as a tool to confirm certain experimental results and not to predict the properties of thin films from their deposition conditions. This thesis benefited from the unique testing facilities of a French-Canadian collaboration between the University of Rennes and McMaster University. The collaboration offered access to two different plasma reactors and to processing facilities such as clean rooms, either to produce some of the building blocks typical of the semiconductor industry or to produce devices designed to evaluate some of the essential elastic properties such as released microbeams discussed in Chapter 4.

We initially focused on the deposition techniques (standard CC-PECVD and ECR-PECVD) to get the best possible control of the optical and mechanical properties of the dielectric thin films. Then, we used a wide variety of experimental techniques available in different laboratories to measure the *ex-situ* properties of the thin films themselves (such as ellipsometry, nano-indentation, and profilometry) or to characterize the semiconductor material in the vicinity of the dielectric thin film structure using (micro-PL, micro-Raman). Some of the deposition and characterization techniques were developed during this research work and are unique, allowing us to go beyond standard approaches. We were able to control the refractive index of SiN_x-based films by tuning the process parameters and optimized the deposition conditions to design functional multilayer structures. Similarly, we controlled the mechanical properties of the films using different characterization methods such as wafer curvature measurements, nanoindentation, microstructures fabrication. We also described our approach to the determination of the elastic properties (mainly bi-axial Young's modulus) of the dielectric thin films, based on the combination of a large panel of techniques.

We fabricated stressor stripes with residual stress on-demand and studied their influence on the substrate. We also addressed modelling of the mechanical strain distribution induced into semiconductor materials by the presence of thin film dielectric structures. The comparison between the experimental results and simulation was well fitting. One important feature of our approach is that we can determine different

elements of the stress / strain tensor using our panel of experimental techniques, such as measuring both the isotropic part (i.e. volume change) using micro-Raman spectroscopy and the anisotropic part of the crystal deformation using DOP/DOLP-PL measurements, as well as mapping of these contributions with a micrometer resolution.

6.2. Suggested future work

We presented in this thesis several avenues for further research which could be pursued in future work to enhance the results presented here. The digitization of deposition reactors is an important step to collect maximum good-quality data during deposition to enhance our ability to control the physical properties of thin films on demand. Characterizing the plasma and film properties *in situ* is essential to understand certain phenomena related to the plasma surface interaction and growth mechanism of amorphous thin films. Therefore, we can use an analytical model employing different mathematical approaches, such as linear and cubic regressions over the measured data, to develop a prediction model for each deposition reactor. This approach will help us obtain initial recipes to engineer some optical and mechanical properties combinations on demand. It would be practical to begin by predicting the deposition rate of the thin films and their optical properties since these two parameters can be measured *in situ* in some systems with integrated ellipsometry, and the data collection can be performed faster.

After improving the control of the properties of the films, it is possible to design "stressor" elements integrated into optoelectronic devices to control some of the semiconductor properties through the locally applied stress. Large-scale industrial schemes already use this strain engineering approach, but many new ideas could be proposed for such development.

References

[1] A. Khan, J. Philip, P. Hess, Young's modulus of silicon nitride used in scanning force microscope cantilevers, J. Appl. Phys. 95 (2004) 1667–1672.

[2] M. Vila, D. Caceres, C. Prieto, Mechanical properties of sputtered silicon nitride thin films, J. Appl. Phys. 94 (2003) 7868–7873.

[3] C.-Y. Chou, C.-H. Lin, W.-H. Chen, B.-J. Li, C.-Y. Liu, High-dielectric-constant silicon nitride thin films fabricated by radio frequency sputtering in Ar and Ar/N2 gas mixture, Thin Solid Films. 709 (2020) 138198.

[4] B. Merle, M. Göken, Fracture toughness of silicon nitride thin films of different thicknesses as measured by bulge tests, Acta Mater. 59 (2011) 1772–1779.

[5] D. Rudmann, D. Brémaud, A.F. Da Cunha, G. Bilger, A. Strohm, M. Kaelin, H. Zogg, A.N. Tiwari, Sodium incorporation strategies for CIGS growth at different temperatures, Thin Solid Films. 480 (2005) 55–60.

[6] T. Ghani, M. Armstrong, C. Auth, M. Bost, P. Charvat, G. Glass, T. Hoffmann, K. Johnson, C. Kenyon, J. Klaus, B. McIntyre, K. Mistry, A. Murthy, J. Sandford, M. Silberstein, S. Sivakumar, P. Smith, K. Zawadzki, S. Thompson, M. Bohr, A 90nm high volume manufacturing logic technology featuring novel 45nm gate length strained silicon CMOS transistors, in: IEEE

Int. Electron Devices Meet. 2003, IEEE, n.d.: pp. 11.6.1-11.6.3. https://doi.org/10.1109/IEDM.2003.1269442.

[7] Y. Sun, S.E. Thompson, T. Nishida, Strain effect in semiconductors: theory and device applications, Springer Science & Business Media, 2009.

[8] M. Huang, Stress effects on the performance of optical waveguides, Int. J. Solids Struct. 40 (2003) 1615–1632. https://doi.org/10.1016/S0020-7683(03)00037-4.

[9] B. Wang, J. List, Basic optical properties of the photoelastic modulator part I: useful aperture and acceptance angle, in: Polariz. Sci. Remote Sens. II, SPIE, 2005: pp. 436–443.

[10] T.M. Benson, T. Murotani, P.A. Houston, P.N. Robson, Photoelastic optical directional couplers in epitaxial GaAs layers, Electron. Lett. 6 (1981) 237–238.

[11] P.A. Kirkby, P.R. Selway, L.D. Westbrook, Photoelastic waveguides and their effect on stripe-geometry GaAs/Ga1— x Al x As lasers, J. Appl. Phys. 50 (1979) 4567–4579.

[12] B. Ku, K.-S. Kim, Y. Kim, M.-S. Kwon, Bulk-silicon-based waveguides and bends fabricated using silicon wet etching: Properties and limits, J. Light. Technol. 35 (2017) 3918–3923.

[13] R.R. Grote, K. Padmaraju, B. Souhan, J.B. Driscoll, K. Bergman, R.M. Osgood, 10 Gb/s Error-Free Operation of All-Silicon Ion-Implanted-Waveguide Photodiodes at 1.55$\mu {\rm m} $, IEEE Photonics Technol.

Lett. 25 (2012) 67–70.

[14] S.P. Wong, W.Y. Cheung, N. Ke, M.R. Sajan, W.S. Guo, L. Huang, S. Zhao, IR photoelasticity study of stress distribution in silicon under thin film structures, Mater. Chem. Phys. 51 (1997) 157–162.

[15] L.D. Westbrook, P.J. Fiddyment, P.N. Robson, Photoelastic channel optical waveguides in epitaxial GaAs layers, Electron. Lett. 5 (1980) 169–170.

[16] A.R. Adams, Strained-layer quantum-well lasers, IEEE J. Sel. Top. Quantum Electron. 17 (2011) 1364–1373. https://doi.org/10.1109/JSTQE.2011.2108995.

[17] P.J.A. Thijs, L.F. Tiemeijer, P.I. Kuindersma, J.J.M. Binsma, T. Van Dongen, High-performance 1.5 mu m wavelength InGaAs-InGaAsP strained quantum well lasers and amplifiers, IEEE J. Quantum Electron. 27 (1991) 1426–1439.

[18] M. Silver, A.F. Phillips, A.R. Adams, P.D. Greene, A.J. Collar, Design and ASE characteristics of 1550-nm polarization-insensitive semiconductor optical amplifiers containing tensile and compressive wells, IEEE J. Quantum Electron. 36 (2000) 118–122.

[19] M. Silver, P.D. Greene, A.R. Adams, Tailoring the heavy-hole and light-hole quantum-confined Stark effect using multistrain-stepped quantum wells, Appl. Phys. Lett. 67 (1995) 2904–2906.

[20] M. Silver, P.D. Greene, A.R. Adams, Polarisation-insensitive modulators based on multistrain stepped quantum well structures, Electron. Lett. 30

(1994) 1890–1891.

[21] J. Bardeen, W. Shockley, Deformation potentials and mobilities in non-polar crystals, Phys. Rev. 80 (1950) 72–80. https://doi.org/10.1103/PhysRev.80.72.

[22] F. Schäffler, Si/Si1− xGex and Si/Si1− yCy heterostructures: materials for high-speed field-effect transistors, Thin Solid Films. 321 (1998) 1–10.

[23] H. Li, Y. Xu, G. Li, Strain effect analysis on the electrical conductivity of Si/Si1− xGex nanocomposite thin films, Solid. State. Electron. 85 (2013) 64–73.

[24] D.A. Antoniadis, I. Aberg, C.N. Chleirigh, O.M. Nayfeh, A. Khakifirooz, J.L. Hoyt, Continuous MOSFET performance increase with device scaling: The role of strain and channel material innovations, IBM J. Res. Dev. 50 (2006) 363–376.

[25] A. Ghrib, M. El Kurdi, M. Prost, S. Sauvage, X. Checoury, G. Beaudoin, M. Chaigneau, R. Ossikovski, I. Sagnes, P. Boucaud, All-Around SiN Stressor for High and Homogeneous Tensile Strain in Germanium Microdisk Cavities, Adv. Opt. Mater. 3 (2015) 353–358.

[26] M. El Kurdi, M. Prost, A. Ghrib, S. Sauvage, X. Checoury, G. Beaudoin, I. Sagnes, G. Picardi, R. Ossikovski, P. Boucaud, Direct band gap germanium microdisks obtained with silicon nitride stressor layers, ACS Photonics. 3 (2016) 443–448.

[27] C.S. Fenrich, X. Chen, R. Chen, Y.-C. Huang, H. Chung, M.-Y. Kao, Y. Huo,

T.I. Kamins, J.S. Harris, Strained Pseudomorphic Ge1–x Sn x Multiple Quantum Well Microdisk Using SiN y Stressor Layer, ACS Photonics. 3 (2016) 2231–2236.

[28] F. Herman, The electronic energy band structure of silicon and germanium, Proc. IRE. 43 (1955) 1703–1732.

[29] A. Ghrib, Ingénierie de contrainte dans des cavités germanium: vers une application de laser intégré sur silicium, (2014).

[30] P. Moontragoon, R.A. Soref, Z. Ikonic, The direct and indirect bandgaps of unstrained SixGe1− x− ySny and their photonic device applications, J. Appl. Phys. 112 (2012) 73106.

[31] H. Guyot, P. Achatz, A. Nicolaou, P. Le Fèvre, F. Bertran, A. Taleb-Ibrahimi, E. Bustarret, Band structure parameters of metallic diamond from angle-resolved photoemission spectroscopy, Phys. Rev. B - Condens. Matter Mater. Phys. 92 (2015) 045135. https://doi.org/10.1103/PhysRevB.92.045135.

[32] S. Gérard, M. Mokhtari, J.-P. Landesman, C. Levallois, M. Fouchier, E. Pargon, P. Pagnod-Rossiaux, F. Laruelle, A. Moréac, B. Ahammou, D.T. Cassidy, Photoluminescence mapping of the strain induced in InP and GaAs substrates by SiN x stripes etched from thin films grown under controlled mechanical stress, (2020). https://doi.org/10.1016/j.tsf.2020.138079.

[33] B. Ahammou, A. Abdelal, J.-P. Landesman, C. Levallois, P. Mascher, Strain engineering in III-V photonic components through structuration of SiNx films,

J. Vac. Sci. Technol. B, Nanotechnol. Microelectron. Mater. Process. Meas. Phenom. 40 (2022) 12202.

[34] E. Schaub, B. Ahammou, J.-P. Landesman, Polarimetric photoluminescence microscope for strain imaging on semiconductor devices, Appl. Opt. 61 (2022) 1307–1315.

[35] J.F. Nye, Physical properties of crystals: their representation by tensors and matrices, Oxford university press, 1985.

[36] D.-X. Xu, W.N. Ye, S. Janz, A. Deî Age, P. Cheben, B. Lamontagne, E. Post, P. Waldron, Stress Induced Effects for Advanced Polarization Control in Silicon Photonics Components, Adv. Opt. Technol. 689715 (2008). https://doi.org/10.1155/2008/689715.

[37] D. Wang, J. Lee, K. Holland, T. Bibby, S. Beaudoin, T. Cale, Von Mises Stress in Chemical-Mechanical Polishing Processes, J. Electrochem. Soc. 144 (1997) 1121–1127. https://doi.org/10.1149/1.1837542.

[38] E.P. Eernisse, Stress in ion-implanted CVD Si3N4 films, J. Appl. Phys. 48 (1977) 3337–3341. https://doi.org/10.1063/1.324217.

[39] M.A. El Khakani, M. Chaker, A. Jean, S. Boily, H. Pépin, J.C. Kieffer, S.C. Gujrathi, Effect of rapid thermal annealing on both the stress and the bonding states of a-SiC:H films, J. Appl. Phys. 74 (1993) 2834–2840. https://doi.org/10.1063/1.354635.

[40] J. Liu, X. Sun, R. Camacho-Aguilera, L.C. Kimerling, J. Michel, Ge-on-Si

laser operating at room temperature, Opt. Lett. 35 (2010) 679–681.

[41] W.A. Kohler, Structural properties of vapor deposited silicon nitride, Metall. Mater. Trans. B. 1 (1970) 735–740.

[42] R. Baets, A.Z. Subramanian, S. Clemmen, B. Kuyken, P. Bienstman, N. Le Thomas, G. Roelkens, D. Van Thourhout, P. Helin, S. Severi, Silicon Photonics: silicon nitride versus silicon-on-insulator, in: Opt. Fiber Commun. Conf., Optical Society of America, 2016: pp. Th3J-1.

[43] L. Vivien, L. Pavesi, Handbook of silicon photonics, Taylor & Francis, 2016.

[44] F. de Brito Mota, J.F. Justo, A. Fazzio, Hydrogen role on the properties of amorphous silicon nitride, J. Appl. Phys. 86 (1999) 1843–1847.

[45] J. Tersoff, Structural properties of sp 3-bonded hydrogenated amorphous carbon, Phys. Rev. B. 44 (1991) 12039.

[46] J. Robertson, Defects and hydrogen in amorphous silicon nitride, Philos. Mag. B. 69 (1994) 307–326. https://doi.org/10.1080/01418639408240111.

[47] H. Gleskova, S. Wagner, V. Gas, Ï. Âk, P. Kova Âc, Low-temperature silicon nitride for thin-®lm electronics on polyimide foil substrates, n.d.

[48] Z. Yin, F.W. Smith, Optical dielectric function and infrared absorption of hydrogenated amorphous silicon nitride films: Experimental results and effective-medium-approximation analysis, Phys. Rev. B. 42 (1990) 3666.

[49] S.C. Mao, S.H. Tao, Y.L. Xu, X.W. Sun, M.B. Yu, G.Q. Lo, D.L. Kwong, Low propagation loss SiN optical waveguide prepared by optimal low-

hydrogen module, Opt. Express. 16 (2008) 20809–20816.

[50] E. Johlin, N. Tabet, S. Castro-Galnares, A. Abdallah, M.I. Bertoni, T. Asafa, J.C. Grossman, S. Said, T. Buonassisi, Structural origins of intrinsic stress in amorphous silicon thin films, Phys. Rev. B - Condens. Matter Mater. Phys. 85 (2012) 075202. https://doi.org/10.1103/PhysRevB.85.075202.

[51] J.A. Floro, S.J. Hearne, J.A. Hunter, P. Kotula, E. Chason, S.C. Seel, C. V. Thompson, The dynamic competition between stress generation and relaxation mechanisms during coalescence of Volmer–Weber thin films, J. Appl. Phys. 89 (2001) 4886. https://doi.org/10.1063/1.1352563.

[52] A. Moridi, H. Ruan, L.C. Zhang, M. Liu, Residual stresses in thin film systems: Effects of lattice mismatch, thermal mismatch and interface dislocations, Int. J. Solids Struct. 50 (2013) 3562–3569. https://doi.org/10.1016/j.ijsolstr.2013.06.022.

[53] G.N. Parsons, J.J. Boland, J.C. Tsang, Selective Deposition and Bond Strain Relaxation in Silicon PECVD Using Time Modulated Silane Flow, Jpn. J. Appl. Phys. 31 (1992) 1943–1947. https://doi.org/10.1143/JJAP.31.1943.

[54] A. Tarraf, J. Daleiden, S. Irmer, D. Prasai, H. Hillmer, Stress investigation of PECVD dielectric layers for advanced optical MEMS, J. Micromechanics Microengineering. 14 (2004) 317–323. https://doi.org/10.1088/0960-1317/14/3/001.

[55] W. Chen, J. Stuckelberger, W. Wang, S.P. Phang, D. Kang, C. Samundsett,

D. MacDonald, A. Cuevas, L. Zhou, Y. Wan, D. Yan, Influence of PECVD Deposition Power and Pressure on Phosphorus-Doped Polysilicon Passivating Contacts, IEEE J. Photovoltaics. 10 (2020) 1239–1245. https://doi.org/10.1109/JPHOTOV.2020.3001166.

[56] W.D. Nix, B.M. Clemens, Crystallite coalescence: A mechanism for intrinsic tensile stresses in thin films, J. Mater. Res. 14 (1999) 3467–3473. https://doi.org/10.1557/JMR.1999.0468.

[57] R.W. Hoffman, Stress distributions and thin film mechanical properties, Surf. Interface Anal. 3 (1981) 62–66. https://doi.org/10.1002/SIA.740030113.

[58] H. Windischmann, Intrinsic stress in sputter-deposited thin films, Http://Dx.Doi.Org/10.1080/10408439208244586. 17 (2006) 547–596. https://doi.org/10.1080/10408439208244586.

[59] C.A. Davis, A simple model for the formation of compressive stress in thin films by ion bombardment, Thin Solid Films. 226 (1993) 30–34. https://doi.org/10.1016/0040-6090(93)90201-Y.

[60] R.P. Dabkowski, Installation of a New Electron Cyclotron Plasma Enhanced Chemical Vapour Deposition (ECR-PECVD) Reactor and a Preliminary Study ofThin Film Depositions, (2012).

[61] H. Fujiwara, Spectroscopic ellipsometry: principles and applications, John Wiley & Sons, 2007.

[62] E. Franke, C.L. Trimble, M.J. DeVries, J.A. Woollam, M. Schubert, F. Frost,

Dielectric function of amorphous tantalum oxide from the far infrared to the deep ultraviolet spectral region measured by spectroscopic ellipsometry, J. Appl. Phys. 88 (2000) 5166–5174.

[63] J. N. Hilfiker, C.L. Bungay, R.A. Synowicki, T.E. Tiwald, C.M. Herzinger, B. Johs, G.K. Pribil, J.A. Woollam, Progress in spectroscopic ellipsometry: Applications from vacuum ultraviolet to infrared, J. Vac. Sci. Technol. A Vacuum, Surfaces, Film. 21 (2003) 1103–1108.

[64] D. Franta, D. Nečas, L. Zajíčková, I. Ohlídal, J. Stuchlík, D. Chvostová, Application of sum rule to the dispersion model of hydrogenated amorphous silicon, Thin Solid Films. 539 (2013) 233–244.

[65] J. Tauc, R. Grigorovici, A. Vancu, Optical Properties and Electronic Structure of Amorphous Germanium, Phys. Status Solidi. 15 (1966) 627–637. https://doi.org/10.1002/pssb.19660150224.

[66] A.R. Forouhi, I. Bloomer, Optical dispersion relations for amorphous semiconductors and amorphous dielectrics, Phys. Rev. B. 34 (1986) 7018.

[67] A. Soman, A. Antony, Colored solar cells with spectrally selective photonic crystal reflectors for application in building integrated photovoltaics, Sol. Energy. 181 (2019) 1–8.

[68] P. Bhattacharyya, B. Ahammou, F. Azmi, R. Kleiman, P. Mascher, Design and Fabrication of Multiple-Color-Generating Thin-Film Optical Filters for Photovoltaic Applications, in: ECS Meet. Abstr., IOP Publishing, 2022: p.

1064.

[69] J. Zhang, A. V Tikhonravov, M.K. Trubetskov, Y. Liu, X. Cheng, Z. Wang, Design and fabrication of ultra-steep notch filters, Opt. Express. 21 (2013) 21523–21529.

[70] G.G. Stoney, G. Gerald, The tension of metallic films deposited by electrolysis, Proc. R. Soc. London. Ser. A. 82 (1909) 172–175. https://doi.org/10.1098/rspa.1909.0021.

[71] W.C. Oliver, G.M. Pharr, Measurement of hardness and elastic modulus by instrumented indentation: Advances in understanding and refinements to methodology, J. Mater. Res. 19 (2004) 3–20. https://doi.org/10.1557/jmr.2004.19.1.3.

[72] S. Dub, P. Lytvyn, V. Strelchuk, A. Nikolenko, Y. Stubrov, I. Petrusha, T. Taniguchi, S. Ivakhnenko, Vickers hardness of diamond and cBN single crystals: AFM approach, Crystals. 7 (2017) 369.

[73] D. Maier-Schneider, J. Maibach, E. Obermeier, A New Analytical Solution for the Load-Deflection of Square Membranes, J. Microelectromechanical Syst. 4 (1995) 238–241. https://doi.org/10.1109/84.475551.

[74] J. Thurn, M.P. Hughey, Evaluation of film biaxial modulus and coefficient of thermal expansion from thermoelastic film stress measurements, J. Appl. Phys. 95 (2004) 7892–7897.

[75] C.-L. Tien, T.-W. Lin, Thermal expansion coefficient and thermomechanical

properties of SiN x thin films prepared by plasma-enhanced chemical vapor deposition, Appl. Opt. 51 (2012) 7229–7235.

[76] M.P. Hughey, R.F. Cook, Massive stress changes in plasma-enhanced chemical vapor deposited silicon nitride films on thermal cycling, Thin Solid Films. 460 (2004) 7–16.

[77] D. Vella, J. Bico, A. Boudaoud, B. Roman, P.M. Reis, The macroscopic delamination of thin films from elastic substrates, Proc. Natl. Acad. Sci. 106 (2009) 10901–10906.

[78] H.W. Pan, L.C. Kuo, S.Y. Huang, M.Y. Wu, Y.H. Juang, C.W. Lee, H.C. Chen, T.T. Wen, S. Chao, Silicon nitride films fabricated by a plasma-enhanced chemical vapor deposition method for coatings of the laser interferometer gravitational wave detector, Phys. Rev. D. 97 (2018) 22004. https://doi.org/10.1103/PhysRevD.97.022004.

[79] X. Jiang, K. Reichelt, B. Stritzker, The hardness and Young's modulus of amorphous hydrogenated carbon and silicon films measured with an ultralow load indenter, J. Appl. Phys. 66 (1989) 5805–5808.

[80] H. Ni, X. Li, H. Gao, Elastic modulus of amorphous SiO 2 nanowires, Appl. Phys. Lett. 88 (2006) 43108.

[81] A.W. Warren, Y.B. Guo, M.L. Weaver, The influence of machining induced residual stress and phase transformation on the measurement of subsurface mechanical behavior using nanoindentation, Surf. Coatings Technol. 200

(2006) 3459–3467.

[82] J. Kim, D.D. Cho, R.S. Muller, Why is (111) silicon a better mechanical material for MEMS?, in: Transducers' 01 Eurosensors XV, Springer, 2001: pp. 662–665.

[83] Y.-G. Jung, M. Martyniuk, H. Huang, B.R. Lawn, M. Martyniuk, X.Z. Hu, Evaluation of Elastic Modulus and Hardness of Thin Films by Nanoindentation Fatigue and fracture of welded metals with soft buffer layer View project A Numerical study on indentation-induced delamination on thin film/substrate system View project Evaluation of elastic modulus and hardness of thin films by nanoindentation, Artic. J. Mater. Res. (2004). https://doi.org/10.1557/JMR.2004.0380.

[84] M. Martyniuk, J. Antoszewski, B.A. Walmsley, C.A. Musca, J.M. Dell, Y.-G. Jung, B.R. Lawn, H. Huang, L. Faraone, Determination of mechanical properties of silicon nitride thin films using nanoindentation, in: Spaceborne Sensors II, SPIE, 2005: pp. 216–225.

[85] S. Perkowitz, Optical characterization of semiconductors: infrared, Raman, and photoluminescence spectroscopy, Elsevier, 2012.

[86] J. Jimenez, J.W. Tomm, Photoluminescence (PL) techniques, in: Spectrosc. Anal. Optoelectron. Semicond., Springer, 2016: pp. 143–211.

[87] D.T. Cassidy, M.A. Fritz, Photoelastic effect from die bonding of diode lasers, Appl. Opt. Vol. 43, Issue 1, Pp. 160-166. 43 (2004) 160–166.

https://doi.org/10.1364/AO.43.000160.

[88] M.A. Fritz, D.T. Cassidy, Extraction of bonding strain data in diode lasers from polarization- resolved photoluminescence measurements, Microelectron. Reliab. 44 (2004) 787–796. https://doi.org/10.1016/j.microrel.2003.08.013.

[89] S.M. Hu, Film-edge-induced stress in silicon substrates, Appl. Phys. Lett. 32 (1978) 5–7. https://doi.org/10.1063/1.89840.

[90] H. Rho, H.E. Jackson, B.L. Weiss, Mapping of local stress distributions in SiGe/Si optical channel waveguide, J. Appl. Phys. 90 (2001) 276. https://doi.org/10.1063/1.1376420.

[91] S. Timoshenko, J.N. Goodier, Theory of Elasticity" McGraw-Hill Book Company, 1951.